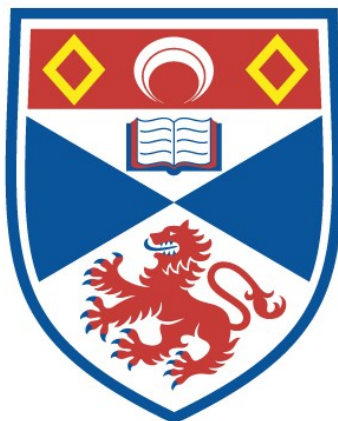


STRUCTURAL AND COMPOSITIONAL ANALYSIS OF COBALT PALLADIUM MODEL CATALYST SURFACES

Alexander Murdoch

**A Thesis Submitted for the Degree of PhD
at the
University of St Andrews**



2012

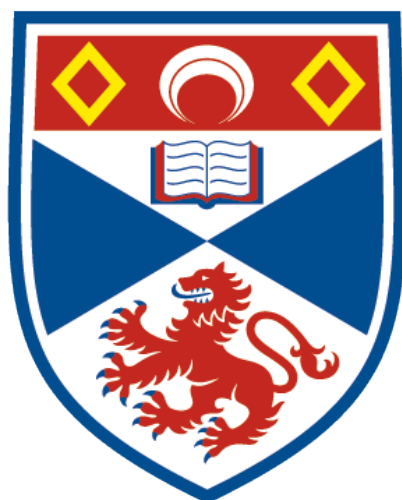
**Full metadata for this item is available in
St Andrews Research Repository
at:**

<http://research-repository.st-andrews.ac.uk/>

Please use this identifier to cite or link to this item:

<http://hdl.handle.net/10023/3640>

This item is protected by original copyright



University of
St Andrews

Structural and Compositional Analysis of Cobalt Palladium
Model Catalyst Surfaces

This thesis is submitted in accordance with the requirements of the University
of St Andrews for the degree of Doctor of Philosophy

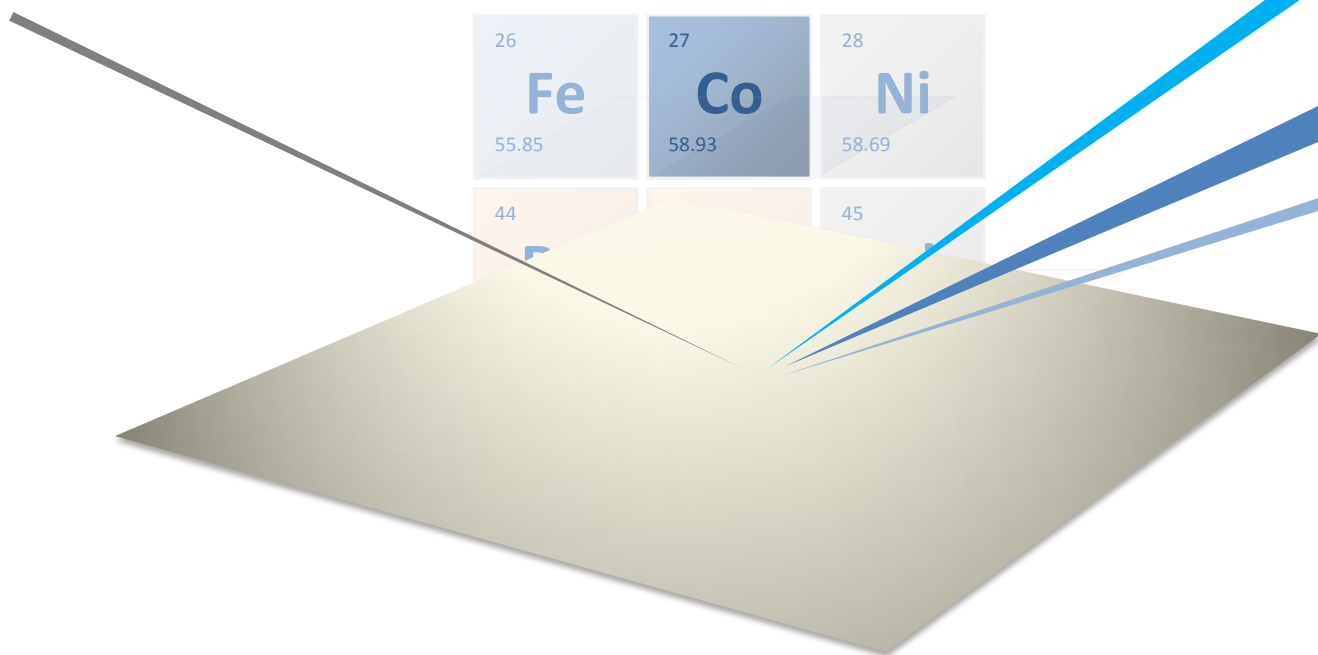
Alexander Murdoch

March 2012



Structural and Compositional Analysis of Cobalt Palladium Model Catalyst Surfaces

By Alex Murdoch



i. Declarations

1. Candidate's declarations:

I, Alexander Murdoch, hereby certify that this thesis, which is approximately 40,000 words in length, has been written by me, that it is the record of work carried out by me and that it has not been submitted in any previous application for a higher degree.

I was admitted as a research student in August 2007 and as a candidate for the degree of PhD in August 2007; the higher study for which this is a record was carried out in the University of St Andrews between 2007 and 2010.

Date: 05 March 2012

Signature of candidate:

2. Supervisor's declaration:

I hereby certify that the candidate has fulfilled the conditions of the Resolution and Regulations appropriate for the degree of PhD in the University of St Andrews and that the candidate is qualified to submit this thesis in application for that degree.

Date: 05 March 2012

Signature of supervisor:

3. Permission for electronic publication:

In submitting this thesis to the University of St Andrews I understand that I am giving permission for it to be made available for use in accordance with the regulations of the University Library for the time being in force, subject to any copyright vested in the work not being affected thereby. I also understand that the title and the abstract will be published, and that a copy of the work may be made and supplied to any bona fide library or research worker, that my thesis will be electronically accessible for personal or research use unless exempt by award of an embargo as requested below, and that the library has the right to migrate my thesis into new electronic forms as required to ensure continued access to the thesis. I have obtained any third-party copyright permissions that may be required in order to allow such access and migration, or have requested the appropriate embargo below.

The following is an agreed request by candidate and supervisor regarding the electronic publication of this thesis:

Embargo on both all of printed copy and electronic copy for the same fixed period of 2 years on the following grounds: Publication would preclude future publication;

Date: 05 March 2012

Signature of candidate:

Signature of supervisor:

ii Acknowledgements

Firstly, I would like to thank my supervisor, Chris Baddeley, for the opportunity to work with him on this project. Thanks also for his incomparable support, advice and help during this project. Thank you for the enthusiasm and encouragement.

I have a great deal of gratitude for the post-docs that I have had the privilege of their support during this project. Aoife Trant and Tim Jones have given generously; their time, experience and patience. They have both made my time enjoyable and devoid of a dull moment.

Many thanks go to Johan Gustafson and Andrew Haire for sharing their knowledge and providing invaluable support especially at the CCLRC facility in Daresbury.

My appreciation goes to Steve Francis, for generously sparing his time to help with experimental setup and equipment problems. Thanks also to Neville Richardson for access to the STM/RAIRS apparatus.

I would like to acknowledge the other members of the surface science department – the experience wouldn't have been the same without them: Riho Green, John Greenwood, Federico Grillo, Shawn Jensen, Sid Jethwa, Daniel Tee, Nicola Toma, and Karen Wilson.

For the extensive support from my family and friends throughout, I would like to express my appreciation. Most of all, to Sarah for being there throughout, putting up with the stressful moments and sharing the more enjoyable moments throughout.

Additionally, I would like to thank Dr Tim Noakes and Dr Paul Bailey at CCLRC Daresbury for their advice involving MEIS during the experiments.

I would like to acknowledge the Sasol, St Andrews and EPSRC for funding of this project and the University of St Andrews for the opportunity to study here.

iii Abstract

To date there has been much work carried out in the field of surface science to gain a better understanding of the fundamentals of a wide range of catalytic systems and reactions. The central theme of this thesis relates to cobalt based Fischer-Tropsch synthesis (FTS) with particular focus on the structure, composition and surface chemistry of CoPd bimetallic systems and on the interaction of Co with oxide support materials.

In the work described in this thesis MEIS and STM are used to examine the growth of Co on Pd{111} and to characterise the structure of CoPd alloys created by thermal treatment of thin Co films. MEIS investigations indicate that Co grows initially as an fcc overlayer, but beyond a few layers, a stacking fault exists resulting in hcp growth. On annealing between 550 and 700 K, a previously unreported ordered surface alloy is observed giving rise to a $p(2 \times 1)$ structure which is concluded to be the surface termination of an ordered CoPd bulk alloy. At higher annealing temperatures, long range Moiré structure is observed by STM which MEIS reveals to correspond to a Pd-rich alloy.

MEIS is used to investigate adsorbate induced segregation effects at CoPd surfaces on Pd{111}. The adsorption of O_2 , CO, H_2 and CO/ H_2 mixtures (syngas) were all examined on a range of bimetallic surfaces. Oxygen adsorption on CoPd alloys strongly segregates cobalt to the surface as a result of the facile oxidation reaction. The behaviour of the components of syngas was more complex with the most noticeable effects being observed on surfaces which were more defect rich.

The growth, annealing behaviour and adsorption properties of Co particles on oxide and mixed oxide surfaces are examined using MEIS and TPD.

iv List of Abbreviations

AES	Auger Electron Spectroscopy
AFM	Atomic Force Microscopy
bcc	Body centred cubic
fcc	Face centred cubic
FTS	Fischer-Tropsch Synthesis
GTL	Gas To Liquid
hcp	Hexagonal close packed
HEIS	High Energy Ion Scattering
HREELS	High Resolution Electron Energy Loss Spectroscopy
IR	Infrared
LEED	Low Energy Electron Diffraction
LEIS	Low Energy Ion Scattering
MEIS	Medium Energy Ion Scattering
ML	Monolayer
PES	PhotoEmission Spectroscopy
RAIRS	Reflectance Absorbance Infrared Spectroscopy
RBS	Rutherford Backscattering Spectroscopy
SFG	Sum Frequency Generation
SMSI	Strong Metal Support Interaction
STM	Scanning Tunnelling Microscopy
TPD	Temperature Programmed Desorption
TPS	Temperature Programmed Spectroscopy
UHV	Ultra High Vacuum
XRD	X-Ray Diffraction



v List of Universally Used Symbols/Notations

Å	Ångström, 0.1 nm
E_f	Fermi Energy
E_{vac}	Vacuum Energy
K	Kelvin
L	Langmuir
ML	Monolayer
MLE	Monolayer Equivalents
ΔH_{ads}	Change in enthalpy of adsorption
θ	Angle
(hkl)	Family of Planes
{hkl}	Specific Plane
<xyz>	Family of Vectors
[xyz]	Specific Vector

vi(a) Definitions; Catalysis

Catalyst:- A substance that increases the rate of a given reaction without being consumed in the reaction itself allowing equilibrium to be reached more rapidly.

Heterogeneous Catalyst:-A catalyst that is in a different state from the reactants and products. The most common is with a solid catalyst and gas phase reactants/products.

Fischer-Tropsch Reaction:- Invented in the 1920's by two German scientists, it is the reaction of carbon monoxide and hydrogen gas over a heterogeneous catalyst to produce a mixture of different hydrocarbons.

Activity:-The conversion is the percentage of the feedstock that reacts over a catalyst. Activity is the conversion expressed as the number of reactions per active catalytic sites per unit time.

Selectivity:- The amount of defined product formed in a catalytic reaction expressed as a percentage of all products. For example low methane selectivity and high selectivity towards gasoline range hydrocarbons are generally desired for a Fischer-Tropsch catalyst.

Promoter:- The term *promoter* is used in catalysis to describe an added species to a catalyst for improved performance. It is also used often to describe a bimetallic catalyst with a low ratio of a metal doped into the primary metal. The former metal is usually high in cost which is the principal reason for using low quantities.

Poisoning:- The decrease in conversion or selectivity due to the catalyst becoming inactive. This happens because the active sites in the metal either become blocked or react with impurities or by-products. Sulphur and graphitic carbon are common substances that deactivate a number of catalysts.

Reducibility:- Catalyst preparation often utilises chemical metal precursors which have to undergo some kind of chemical decomposition to achieve metal particle formation. Reducibility is defined by the mole percent of atoms in these particles that are reduced to the metallic state.

Support:- A catalyst support is primarily designed to decrease catalyst costs. The active component is finely dispersed across a support which has a large surface area per mass resulting in a high surface area per mass of the active component. For costs to be lowered substantially, the support must be extremely inexpensive in relation to the active component. Supports must be carefully chosen considering the reactor style and the reaction being carried out. Generally supports should be structurally tough, highly porous and have high thermal stability along with being chemically compatible with the reaction.

vi(b) Definitions; Surface Chemistry

Azimuth:- The azimuth is a vector direction defined by the crystal plane that is it perpendicular to. For example the fcc<112> azimuth is perpendicular to the fcc{112} plane in an fcc crystal.

Facet:- When single crystals are cut or formed the faces that are exposed will be different on a number of different faces or planes which are defined by their miller indices e.g. fcc{110}. This is important for discussing crystalline nanoparticles and the exposed crystal faces that will have important differences in reactivity.

Langmuir:- 1 Langmuir is an approximation for the number of gas molecules required to saturate the surface molecular adsorption sites at a given temperature and pressure. Assumptions include: a sticking probability of one, single layer adsorption, no interaction between adsorbed species and equivalent ΔH_{ads} for all molecules. 1 L is equivalent to 1 second exposure at a pressure of 10^{-6} torr.

Monolayer (Equivalent):- A single continuous layer of atoms deposited onto a surface corresponds to a monolayer. Monolayer equivalent is used when the growth does not proceed in a layer-by-layer fashion, and corresponds to the number of atoms required to form a theoretical single layer.

Terrace:- Single crystals are never formed completely flat and include raised areas and depressions. Terraces are the extended flat areas between steps. The chemistry associated with this part of the single crystal is concerned with a lack of major defects or to single point defects such as interstitial atoms or kinks in the surface depending on how the experiments are focused.

Reconstruction:- Atoms in solid materials are in the lowest energy state when fully coordinated by its neighbouring atoms. On the surface some of these neighbouring positions are vacant resulting in a higher potential energy. In some cases atoms in the surface layers will form a new structure that is lower in energy to counter this, which is known as reconstruction.

Step Edge:- Where one terrace meets another of a different height there is a 'step' up or down. Atoms at the step edge have a lower coordination number and as a result are more reactive and may also undergo reconstruction as discussed previously.

Sticking Probability:- The probability of adsorption of a single molecule onto a surface is dependent on the orientation and kinetic energy of the molecule. Sticking probability is the ensemble property defined as the rate of molecular adsorption divided by the collision rate and is often dependent on the surface coverage.

Contents

i)	<u>Declaration</u>	5
ii)	<u>Acknowledgements</u>	7
iii)	<u>Abstract</u>	9
iv)	<u>List of Abbreviations</u>	11
v)	<u>List of Universally Used Symbols/Notations</u>	12
vi)	<u>Definitions – a) Catalysis, b) Surface Science</u>	13
vii)	<u>Contents</u>	15
	1.0 <u>Chapter 1: - Introduction</u>	17
	1.1 Fischer-Tropsch Background	19
	1.2 Introduction to Catalysis	20
	1.3 Fischer-Tropsch Chemistry	22
	Cobalt FT Catalysts	22
	Bimetallics and Promoted Catalysts	23
	Deposition Methods	25
	Chemical and Thermal Treatments	26
	Catalyst Behaviour Under FTS Conditions	26
	Poisoning	27
	1.4 The Surface Science Approach	28
	Relating Surface Science with ‘Real’ Catalysis	30
	Single Crystal Analysis	31
	Supported Nanoparticles	33
	1.5 Aims of the Thesis	36
	1.6 Introduction Bibliography	37
	2.0 <u>Chapter 2: - Experimental Techniques</u>	41
	2.1 Sample Preparation	43
	2.2 UHV Systems	45
	2.3 LEED	47
	2.4 Auger	48
	2.5 TPD	49
	2.6 STM	50
	2.7 MEIS	52
	2.8 RAIRS/DRIFTS	57
	2.9 Experimental Bibliography	59

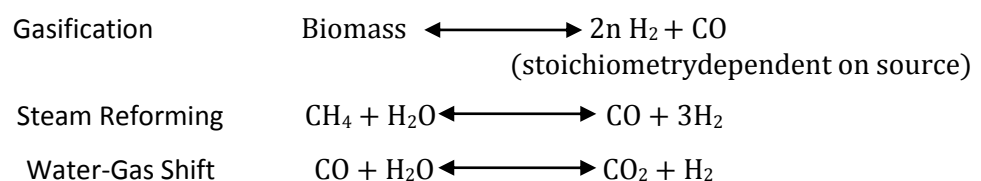
3.0	<u>Chapter 3: - Structural and Compositional Analysis of CoPd Alloys on Pd{111} using MEIS and STM</u>	61
3.1	Introduction	63
3.2	Experimental Summary	66
3.3	Results	68
3.4	Discussions	76
3.5	Conclusions	83
3.6	Chapter 3 Bibliography	84
4.0	<u>Chapter 4: - Behaviour of CoPd Alloys on Exposure to Oxygen and Behaviour of Ultrathin Cobalt Oxide Layers on Pd{111}</u>	85
4.1	Introduction	87
4.2	Experimental Summary	90
4.3	Results	92
4.4	Discussions	100
4.5	Conclusions	104
4.6	Chapter 4 Bibliography	106
5.0	<u>Chapter 5: - Adsorbate Induced Segregation of CoPd Alloys on Pd{111}: Examination of CO, H₂ and Syngas adsorption using MEIS and RAIRS</u>	107
5.1	Introduction	109
5.2	Experimental Summary	114
5.3	Results	116
5.4	Discussions	136
5.5	Conclusions	140
5.6	Chapter 5 Bibliography	141
6.0	<u>Chapter 6: - Characterisation of Mixed Alumina-Titania Model Supports</u>	143
6.1	Introduction	145
6.2	Experimental Summary	149
6.3	Results	151
6.4	Discussions	159
6.5	Conclusions	162
6.6	Chapter 6 Bibliography	163
7.0	<u>Chapter 7: - Overall Conclusions and Further Work</u>	165
7.1.	Conclusion Summary	167
7.2.	Further Work	169
7.3.	Conclusion Bibliography	170

Introduction

1.1 Fischer Tropsch Background

The method of converting a CO and H₂ mixture (syngas) into liquid fuels, part of gas to liquid (GTL) chemistry, was invented in 1922 by Franz Fischer and Hans Tropsch [1]. The process was greatly utilised during the Second World War by Germany and later on during the apartheid era in South Africa. During these periods the availability of crude oil was insufficient to cover the demand for liquid fuels and other petroleum derivatives. On the other hand each country had vast deposits of coal (from which syngas can be derived) within their borders. Minor interest was also shown shortly after the Second World War by U.S.A. until the realisation of the wealth of oil within America and western control of oil in the Middle East. Aside from these periods of history, little interest has been invested in Fischer-Tropsch Synthesis (FTS).

This brief history highlights the potential for this technology in the near future considering increasing demand for petroleum. Research in geology, geography and other disciplines has shown that the global oil supply has a limited future economic potential for supplying the world with energy. In addition to this is the growing realisation that mankind has caused severe damage to the environment in the last 200 years associated with global industrialisation, in particular the release of large quantities of CO₂ resulting from the use of fossil fuels. The potential of FTS for solving the problem of diminishing oil reserves is unfortunately associated with the environmental issues of releasing CO₂ from a coal resource instead of oil, thus diminishing one problem but not the other. However the real potential of FTS may be to utilise biofuel technology as a source of syngas [2, 3] by converting biomass into a H₂/CO mixture *via* the reactions shown below:



Biomass is a generic term covering – among other things – sewage, organic waste and agricultural waste. If this achievement is realised then mankind will have an exceptionally clean energy supply which can be easily integrated into transport, electricity supply, heating, food production and leisure with little or no modification.

The products of FTS consist of a range of simple hydrocarbons such as methane, methanol, ethane, ethanol, isobutane, and diminishing amounts of higher hydrocarbons. The value of each

product depends on the consumer market. Methane, which is usually produced in large quantities, is a low value product because it is relatively easy to obtain as a natural resource (e.g. from natural gas), has a low energy density for use as a fuel and is not easily converted to other valuable products [4]. C₂₋₄ (commonly known as liquid petroleum gas, or LPG) has a higher value as a fuel with greatly increased energy density. Increasingly higher chain hydrocarbons such as the gasoline fraction (C₅₋₈), kerosene fraction (C₈₋₁₅) and diesel fuels fraction (C₁₂₋₁₈) are in great demand for transportation and energy production and are thus high value products.

To gain higher value products other processes may follow FTS such as the Mobil process [5] and reforming/cracking catalysis; producing longer chain hydrocarbons as well as iso-paraffins and aromatics (both give high octane numbers needed for petrol engines). However, additional processes add cost and energy consumption to the overall production of the different chemicals. The desired properties of FTS are to either have a high selectivity towards higher molecular weight products, branched alkanes, oxygenated hydrocarbons or aromatics. A range of catalysts with high selectivities towards specific product ranges will reduce additional processing costs whilst reducing waste. The ability to create highly selective catalysts will come from an understanding of the surface chemistry on an atomic scale.

1.2 Introduction to Catalysis

Carbon monoxide, with a bond dissociation energy of 1072 kJ mol⁻¹ [6], has the strongest known covalent bond. Consequently reactions that involve breaking apart a molecule like CO often have very poor rates associated with the resulting high activation energy. For this reason the FT reaction is required to be carried out over a catalyst. A catalyst is defined as a substance that increases the rate of a given reaction without being consumed in the reaction, allowing equilibrium to be reached more rapidly. In terms of energy this means the activation energy is lowered, so at a given temperature a larger proportion of molecules exceed the activation energy in order to react. In terms of bonding the carbon monoxide is 'activated' as it adsorbs on the catalyst surface, therefore reducing the bond order of the carbon-oxygen bond. Without the catalyst the kinetics of the reaction of CO with H₂ would prevent FTS from being commercially or environmentally practical.

FTS reactions can be carried out over a number of different transition metal catalysts. Many metals have some FT activity. However, the metal-CO bonding strength defines whether a given metal can be considered as 'FTS active'. This bonding can either be physisorption, where the

reactant stick to the surface primarily *via van der Waals* interactions, or chemisorption, where there is an electron transfer between the surface and the molecule; resulting in a chemical bond. This bond formation modifies the order of the intramolecular CO bond and, depending on the extent of electronic charge transfer, may be enough to break these bonds (dissociative chemisorption) and the components of the molecule will be adsorbed at two different sites. This principle is demonstrated in the diagram given in *figure 1.1* along with a potential energy diagram in *figure 1.2* [7] which compares physisorption and chemisorption.

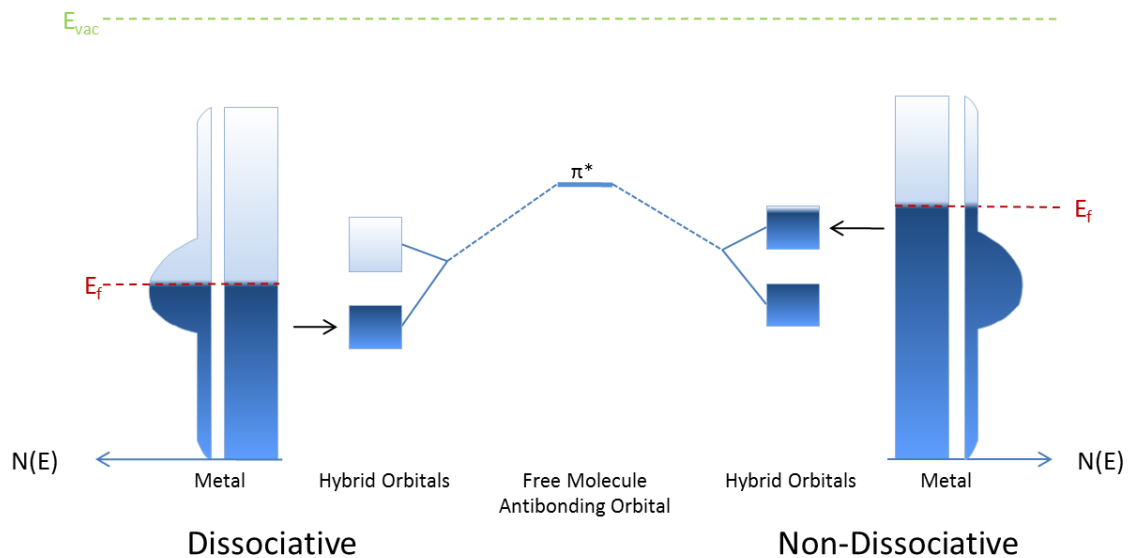


Figure 1.1:- Energy levels for adsorption example of a gas molecule on two different metals. E_f , Fermi energy; E_{vac} , vacuum energy; π^* , molecular antibonding orbital.

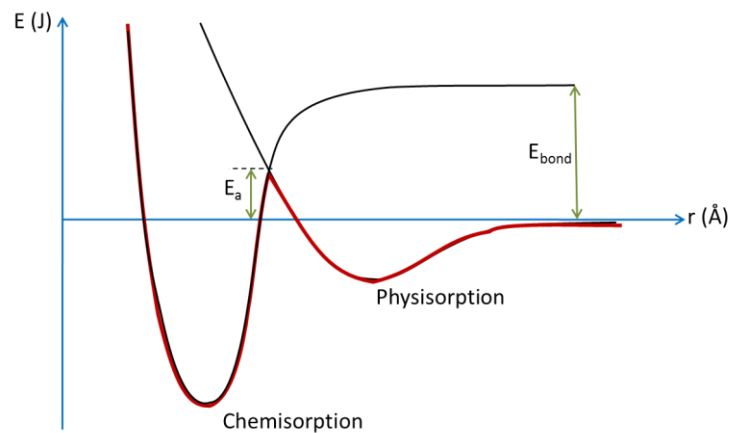


Figure 1.2:- Potential energy diagram for dissociative bonding at the surface of a solid. E , Potential Energy; r , distance between molecule and surface atom; E_{bond} , bond dissociation energy of the molecule; E_a , activation energy.

For the dissociative adsorption, the metal donates electrons to the antibonding orbitals of the molecule reducing the bond order significantly. For non-dissociative bonding, the donation from the metal does not lead to strong metal-adsorbate bonding, and the resulting molecular bond has a substantial bond order.

1.3 Fischer Tropsch – Chemistry

FT catalysts occupy a section of transition metal elements around group VII and VIII, to the left of which the bonding to CO is strongly dissociative and results in detrimental coking of the catalyst surface. In the other direction the bonding is too weak to sufficiently 'activate' CO. The target range of hydrocarbon products should ideally determine the composition of the catalyst, but in reality the cost of the metals used [8] plays a much bigger role. For this reason FT catalysts are based on either iron or cobalt; often supported by an inexpensive oxide support to increase the surface area. Small amounts of the more expensive metals such as platinum, palladium, ruthenium or rhodium may also be included if the value of the product range can be increased substantially.

Cobalt FT catalysts

An extensive review of Fischer-Tropsch catalysts is given by Khodakov *et al* [9]. The topics covered include: Discussion of the primary FTS metals (Fe, Co), the promoting role of alkali and transition metals on the catalytic behaviour and the role of support (primarily alumina, silica, titania and mixed oxides). Details of the different catalytic systems reviewed are discussed individually throughout the following sections before discussing related studies in surface analysis.

Another extensive review by Somorjai [10] describes the hydrogenation of CO and CO₂ over different metallic catalysts from the viewpoint of molecular interactions with the catalyst surface. The studies reviewed are a combination of catalytic reaction research and surface adsorption investigations. The former provides the product distribution while the latter provides explanations for the product distribution in terms of adsorption dynamics. Hydrogen dissociative adsorption is facile on transition metals and CO dissociative adsorption is seen to be a key factor in the primary reaction step in FTS, occurring readily on cobalt and iron but not on platinum and palladium. The chain growth mechanism is described as occurring as a result of the presence of highly mobile hydrocarbon species (-CH₂, -CH₃, -CH₂CH₃, as well as more complex intermediates) on the surface. The promotion with noble metals is shown to have the effect of maintaining the metallic nature of the cobalt through the hydrogen spillover mechanism where H₂ dissociatively adsorbed on the noble metal sites adjacent to cobalt restricts the oxidation from water. The author focuses on describing the effect of the chosen metal-promoter combination over any other considerations. From this paper it can be seen that cobalt alloyed with rhenium or ruthenium is utilised for the production of higher weight hydrocarbon chains. As discussed previously, these molecules are more important

economically because they can be used either directly (as fuels, solvents, etc) or further converted into high value petroleum products.

The comparison of reaction selectivities for different metals is a primary consideration in catalysis. The main FTS choices, due to reactor running costs and catalyst costs, are cobalt and iron; the latter selected for producing the lighter gasoline fractions [9] and the former for heavier diesel and paraffin waxes [9]. The performance of other metals is of interest, largely to provide an understanding of their role as promoters.

Dongyan *et al* offer a comparison of cobalt to ruthenium, platinum and palladium [11]. Ruthenium was shown as the only catalyst with a higher conversion (8.4% compared to 6.4% for cobalt). The cobalt in this example is stated to have reducibility of 61.3%, which would contribute to the relatively low conversion. The large cost of ruthenium relative to cobalt effectively removes the advantage of having the higher conversion rates.

Bimetallics and Promoted Catalysts

The usual purpose of promoters in catalytic particles is to 'tune' the selectivity and reactivity of the catalyst. Although each individual metal may not be ideal for the reaction, alloying produces a catalyst with intermediate properties – in some cases alloying can also eliminate detrimental effects from one of the individual metals. In FTS the selectivity and activity of the catalysts are extremely important. Metallic nickel is seen to produce low carbon weight molecules like methane [9] which are relatively inexpensive products. Cobalt based catalysts are used to produce higher molecular weight hydrocarbons in the kerosene-diesel range [9] and iron for LPG ranges, all of which have a greater value. This selectivity can then be improved by the addition of promoters such as rhodium and platinum to a catalyst in order to produce cyclic hydrocarbons or iso-hydrocarbons; and because such petrochemicals can be used as additives in motor fuel or in the synthesis of other high value products, they have great economic value. The other advantage is that the catalyst material has a high weight percent of the relatively cheap metal, but the properties are increasingly similar to the more valuable metal, keeping the catalyst price low.

In order to select the best promoter to optimise catalytic performance it is necessary to understand the effect of the promoter on the overall chemistry. Often in heterogeneous catalysis, an

empirical trial and error approach is used. As a result, there is still debate regarding the mechanisms underpinning the operation of many industrial catalysts.

In addition to the comparison of the individual metals (discussed in the previous section), Dongyan *et al* also examine cobalt catalysts doped with small quantities of the metals discussed above [11]. The doped catalysts are dramatically improved with increases in activity and improvements in the selectivities towards higher hydrocarbons; the hypothesis is that the increased reducibility is the principal cause for these improvements. The reducibility is concluded to be a result of hydrogen spillover from the noble metal sites, aiding reduction and protecting the cobalt sites from oxidation.

Also studied was Co/Zn on titania which exhibited lower activity than a reference sample of cobalt supported on titania [12]. Samples consisting of particles on titania surfaces were characterised using XPS as well as TPR, XRD, TGA (ThermoGravimetric Analysis) and laser Raman spectroscopy. In this study catalysts are prepared by a co-precipitation sol-gel method as well as incipient wetness impregnation of cobalt and zinc species on pre-prepared titania. The order of deposition of cobalt and zinc are changed showing very little change [12], whilst the variation of the content of zinc is shown to increase CO conversion by approximately 25% - attributed to a reduction of the strong metal support interaction (SMSI) as zinc is thought to produce a 'sandwich layer' between the cobalt particles and the titania. The selectivities towards C_1 , however, are seen to increase combined with decreasing higher hydrocarbons in all but one of the samples.

The addition of gold to cobalt catalysts has been shown [13, 14] to have a large effect on selectivity especially in heterogeneous catalysis. In FTS the selectivity is considered to be improved at low surface concentrations of gold [15]. It is hypothesised by the authors that gold either reduces catalytic selectivity towards hydrogenolysis reactions and thus allows chain growth, or that there is some dilution effect on the formation of the products. At higher gold concentrations the surface concentration of gold increases and, due to the loss of active cobalt sites, the activity and selectivity dramatically decrease.

Addition of gold to cobalt also shows improved reducibility [16], characterised using TPR, with reduction occurring at lower temperatures during catalyst preparation (along with an improvement in catalyst regeneration) [16]. The samples utilised a kaolin support and were designed for the production of 2,3-dihydrofuran, a dehydrogenation reaction [16]. The presence of water in

this study correlated to the water by-product in FTS that has been hypothesised to be a possible cause of the oxidation of cobalt based catalysts [9].

Deposition Methods

The usual method of metal impregnation onto the oxide surface is the incipient wetness chemical synthesis where the oxide pellets or particles are mixed with an appropriate solvent containing a complexed metal precursor [9]. The particles are then dried under controlled conditions allowing the precursors to precipitate in the pores of the support. Then the metal precursor is chemically treated to decompose the species *via* metal oxide into the fully reduced metal. This route introduces additional variables during the catalyst formation that are poorly understood.

There have been a number of studies [17-27] using metal complex precursors as methods of deposition. In surface science a prepared crystal of either a pure oxide (for AFM) or a metallic crystal with a passive –naturally formed – oxide layer (for atmospheric STM), is spin coated using the appropriate solution containing the metal precursors. Spin coating ensures a uniform deposition of the precursor as compared to deposition *via* immersion. The chemical and thermal reductions/decompositions are mirrored on the processes used for an industrial prepared catalyst whilst measuring the structural and chemical results of the particles using surface science methods.

The most common precursor utilised in cobalt catalysts is hydrated cobalt nitrate [18-21, 26]. Another possible precursor for cobalt that has been reported [17-19, 24-25, 27] is dicobaltocarbonyl. One study in particular compares the samples formed from both cobalt octacarbonyl and cobalt dodecacarbonyl as well as cobalt nitrate (hydrated) [19]. As well as $\text{Co}_2(\text{CO})_8$ some research includes analysis on $\text{Co}_4(\text{CO})_{12}$ which has been found to be an intermediate along with other higher carbonyls [9] in the decomposition of $\text{Co}_2(\text{CO})_8$. The effects of the precursors can be significant in some cases, but the underlying causes are poorly understood.

The structure of the oxide support, as well as the pH, temperature and pressure during the decomposition reactions are expected to strongly influence the particle size and structure. The penultimate state of the catalyst formed from most chemical precursors is cobalt (II) oxide (CoO). The step that follows does not fully reduce all of the cobalt, and a certain fraction of the total cobalt remains as an oxide *in situ*. The result of this is a catalyst with diminished activity and poor selectivity

[9] which has been proven to be improved to different degrees with the use of promoters [9], [28] as well as using a number of acidic chelating agents [29] that aid reduction.

Chemical and Thermal Treatments

Chemical deposition adds an additional level of complexity to the overall system. The choice of chemical precursor obviously has an effect on the metal structure, but an equally strong effect comes from the kinetics and thermodynamics of the decomposition reactions. From basic crystallography it is known that fast cooling of a molten material freezes the material in the amorphous state and slow cooling allows a crystal to form. With the correct kinetics, purity and a good seed crystal or nucleation site, highly ordered crystals can be produced despite their entropic encumbrance. Similar crystal dynamics are true for chemical formation and post-sintering of the metal particles.

Reported primarily in the field of catalysis is analysis of the influence of preparation method on catalytic activity and selectivity [9]. The study by Matthey *et al* on titania preparation [30] is a good example of the extreme effects of chemical treatment of a surface. The controlled termination groups of the titania surface in this case, change the nucleation sites and morphology of the gold particles. More relevant to FTS in particular is temperature treatment due to the two structural phases of cobalt that can both be present at the temperatures used in FT catalyst preparation and reactions.

Mentioned above is the use of organic acid chelating agents which appear to aid the reduction of the cobalt oxide improving the activity as well as selectivity of the final catalyst [29]. The data indirectly describe the effectiveness of each of the chemicals used from the reaction performance. The likely effect is that the acidic chelating agents surround the cobalt metal atoms or particles forming intermediates between cobalt oxide and cobalt metal, and subsequently 'catalyse' the reduction with hydrogen.

Catalyst Behaviour Under FTS Conditions

Many different techniques are used to investigate adsorbate chemistry in surface science. When the system is correlated with a real catalyst, as it is in the experiments described in this thesis, adsorbate chemistry is possibly the most relevant interaction in the system. Even the effect of the

adsorbates on the chemical and structural properties of a catalyst come back to affect the products of the catalytic reaction. In surface science studies of FT catalysis, the reactant gas (syngas) consisting of hydrogen and carbon monoxide is used as a probe in different techniques (described in *Chapter 2*). The change in structure along with changes in the electronic, vibrational and bonding properties can be studied using several methods. Additionally desorption and vibrational techniques can be used to analyse the desorbing molecules as well as adsorbed intermediates of FTS on the surface which explain the product distribution of the overall reaction.

The catalytic studies that are discussed generally examine the effect on the reaction products after altering the catalyst. Although trends from these experiments can be extrapolated, it is difficult to gain a clear understanding of the underlying processes. In surface science the interaction with each of the different surfaces can be examined as well as with the surfaces of supported particles enabling the investigation of the structural and chemical basis of the highest performing catalysts, therefore providing a better understanding of the system.

Poisoning

Poisoning is an advantageous research subject in catalysis and surface science because of the implications in the industrial use of a given catalyst. The major poisoning mechanism in cobalt-based FTS is oxidation of the metallic component [9]. The research on this topic reviewed by Niemantsverdriet *et al* [31] contains a number of conflicting studies. The review concludes that, in some circumstances, the oxide reacts with the metal and cobalt silicate/aluminates are formed and, in the case of titania, encapsulation of the nanoparticles occurred under FTS conditions, thus deactivating the catalyst. For titania it has been shown that the interaction with the active catalyst particles strongly depends on the preparation conditions (reducing/oxidising/hydrating) of the oxide before deposition is carried out [30]. Catalysts prepared from cobalt nitrate and other chemical precursors have been seen to only partially reduce during preparation thus initial activity is low [9].

Oxidation is a widespread problem in FTS catalysts coming from both preparation method and poisoning while the reactor is online. A number of studies hypothesise that promoting with noble metals reduces the reactivity of the metal with the oxide support and trace water/oxygen in the reactor [32].

From this we can look at the importance of the oxide support as well as promoters on the reactivity of the active metal. For example the saturated nature of silica/alumina may aid cobalt oxidation and non-stoichiometric titania that can be oxidised may depress the effect as well as the changes in the electronic structure and particle size effects of the different supports. However where oxide supports may be selected to inhibit metal oxidation it is thought [9] that certain oxides react in an adverse way with the metal, for example, creating cobalt silicates/aluminates, inactive in FTS. Additionally differing chemical and thermal preparations can have an effect on the stability of the final supported catalyst.

Additionally the effect of sulphur poisoning has been reported [33]. Lietti *et al* describe how low amounts of sulphur exposed to the catalyst decreases activity without any significant change to the selectivity. However at higher levels increased towards 2000 ppm the catalyst selectivity changes to favour smaller hydrocarbon molecules over long chain molecules. It is probable that this is a result of the significant decrease in the number of adjacent active catalyst sites because of high sulphur coverage.

Carbon deactivation, or coking, is known to be a problem in many types of organic catalysis. In FTS coking is rarely a problem because the catalyst is designed for the adsorbed carbon to be relatively mobile in order to allow carbon and CH_x groups to come together and polymerise [10]. The addition of metals such as platinum which do not cause CO to dissociate [10] can be postulated to decrease the strength of the carbon-metal bonding through electronic effects.

A thermodynamic study on the temperatures required to hydrogenate different types of carbon [34] states that at normal FTS temperatures only carbidic carbon can react where amorphous and graphitic carbon cannot. This is an important point for the possibility for coking. However, this paper clarifies that coking is prevented by inhibiting the formation of networked carbon structures over the cobalt catalysts.

1.4 The Surface Science Approach

The general aim of surface science research is to gain a comprehensive understanding of the processes at the molecular level including metal-support interactions, catalyst-adsorbate interactions and surface and adsorbate structure. This fundamental view of the chemistry of a surface requires a high level of control with few variables affecting the data. To accomplish this, a

model is used as an alternative to the real system using the same metals, molecules and other compounds whilst simplifying the macroscopic structure. This can present problems comparing to a real catalyst because macroscopic structure could have a real effect on the chemistry, thus a major aspect of surface science is to find a reasonable compromise between simplicity and realism. However the advantage of using simple atomically flat supports allows the use of many techniques that would not be able to be utilised to study surfaces inside a porous or rough sample.

In 2007, a notable pioneer of surface science, Gerhard Ertl, was awarded the Nobel Prize in Chemistry “for his studies of chemical processes on solid surfaces” [35]. He was the one of the first to see the potential for new surface science techniques such as LEED, UPS (Ultraviolet Photoemission Spectroscopy) and STM.

The most simplified but widely used model involves experimentation using single crystals. The ordered nature of single crystals allows fundamental interactions between the surface and adsorbed species to be analysed in a reproducible fashion. Although this method provides the highest level of control the crystal surface is never completely free of surface defects which often contribute significantly [36] towards the results.

To produce data more closely correlated in structure to real catalytic systems, a model of oxide supported particles, a common catalyst type, can be analysed. A widely reported [37-39] method for this is to use an ultra-thin Al_2O_3 film grown on a metal substrate to model the standard porous alumina support commonly used in some catalytic reactors [40]. This method has displayed [37] that even layers only a few angstroms thick exhibit near-bulk properties. The active metal component is then deposited and analysed using the range of techniques available. The main advantages of this approach are that nanoparticles supported on planar oxide surfaces are easier to characterise than those inside porous supports. In addition many of the surface analytical methods used utilising charged particles or a tunnelling current require the sample to act as a conducting earth for the subsequent charge accumulation. The thin oxide layers produced have small enough resistances to avoid charging effects. With the use of supported particles on an oxide as an alternative to a single crystal metallic substrate, the model catalyst more closely simulates the structure of a real catalyst.

Relating Surface Science with 'Real' Catalysis

An important feature in the surface science approach to understanding catalytic systems is to produce models as close to a working material as possible, otherwise known as bridging the *material* and *pressure* gaps. Surface analysis techniques generally use ultra high vacuum (UHV), fully described in the *Chapter 2*. This firstly presents a problem known as 'the pressure gap' because working materials usually operate at atmospheric pressure, and in the example of catalysts, in great excess of atmospheric pressure.

Secondly the samples are very simple models of a working material with 'flat' surfaces and well controlled defects. In a working heterogeneous catalyst the material must have, by design, a large surface area per mass to increase the production per capita spent on the catalyst material. This applies to the support as well as the active metal in the catalyst. As well as product turnover the selectivity can often depend heavily on defect structure, pore size and the methods used for catalyst preparation. The differences in structure of a real catalytic material compared with a single crystal model catalyst are collectively described as 'the material gap'.

Experimental design therefore has a large role in bridging the gap between surface science analysis and catalyst design. The techniques used must be developed to further improve the ability of surface methods to understand, even predict and improve real materials. Freund *et al* review studies [41, 42] that utilise LEED, PES, STM and to a lesser extent TEM and RAIRS for the analysis of surface interactions. These studies describe the growth and morphology of rhodium, palladium, cobalt, platinum and vanadium nanoparticles supported primarily by alumina, although silica, titania, magnesia and nickel oxide are also discussed. Significantly the alumina is grown on several substrates, analysing the quality of the oxide layer to discern the influence of each substrate.

Of the methods and substrates discussed, the possible problems highlighted are high disorder and holes in the thin film where the metallic substrate is exposed. Alumina formed by the oxidation of a NiAl(110) crystal is described to have a uniform structure with a film thickness of 5 Å which is structurally characterised by Kresse *et al* [39]. The deposition of metals in the monolayer regime onto oxide surfaces results in the formation of particles which can then be analysed to determine particle structure, their thermal stability and their interaction with adsorbates.

nucleation of particles on defect sites in the oxide surfaces with the use of (Scanning Tunnelling Microscopy) STM. In the case of TiO_2 the gold particles form on reduced (oxygen vacancy) and oxidised (interstitial oxygen) sites but not on hydrated sites [30]. Deposition on an inactive surface – hydrated in this case – results in nucleation at structural defect sites which, in this case are the step edges.

Single Crystal Analysis

Single crystal analysis is the main methodology of UHV surface science. The single crystal gives an almost perfectly flat surface of a selected orientation. This specific surface gives an ability to test adsorbates on surfaces with different co-ordination environments of surface atoms. An adsorbate molecule or adatom in a hollow site of an fcc (111) surface, for example, has a coordination of 3 surface atoms. On a higher indexed face the co-ordination can be higher where the adsorbate can stick to the surface at defects such as step and kink sites. Even the orientations of the surface atoms co-ordinated to the adsorbate are relevant because considering molecular adsorbents the molecular orbitals have specific orientation.

Work on cobalt single crystals without promoters has been carried out on a number of different crystal orientations [45, 46]. The crystals are prepared in UHV and are passed directly into a reactor cell for testing. This set up allows a bridging of the pressure gap, mentioned before, whilst retaining control over the metal surface and the introduction of impurity gases, such as water and oxygen. Cobalt crystals with a surface orientation of (0001) [45] as well as (1120) [46] – schematic representations shown in *figure 1.3* – have been tested under a range of different reaction conditions for both batch and flow reactions.

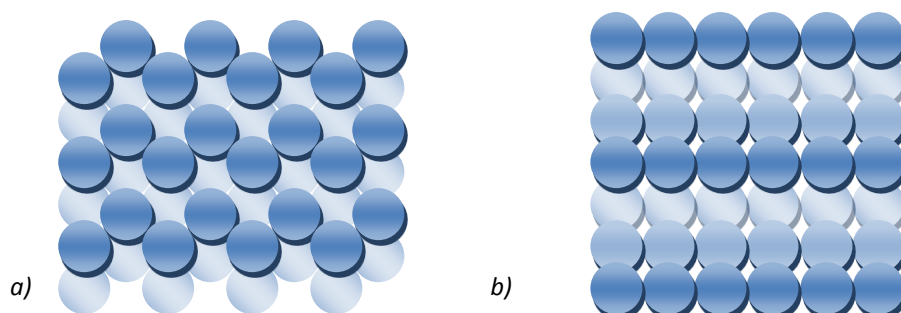


Figure 1.3:- Top down views of Co(1120) (a), and Co(1012) (b).

In this work [45, 46] the samples were prepared in UHV then transferred to a high pressure cell where the reaction tests are carried out after which the samples are transferred back to be characterised with AES, EELS and LEED. The EELS data displays mainly adsorbed CO and CH_x species

and the conclusion from the LEED is that the adsorbed species have no significant long range order determined by a blurred pattern and a lack of additional spots. Overall conclusions are that the activation energies for the formation of C_1 , C_2 and C_3 products are very similar suggesting a similar rate determining step. Additionally the comparison between the (0001) crystal data [45] and the data from the higher order surfaces [46] it has been concluded that there is an increase in chain growth probability correlated with the detection of C_{4+} fragments in the EELS spectra. From this it would appear that where the activity has been stated as being structure insensitive, the selectivity is not. This can be clarified by stating that the hydrogenation reaction is not structure insensitive and chain growth is.

Comparing single crystal analysis [45] to studies on prepared catalysts [11] selectivity is found to be higher towards smaller molecules over single crystals. This indicates FTS reaction dynamics are influenced by secondary chain growth reactions controlled by either the oxide support or the defects and differing exposed facets of the particles. Metal atoms on the surface with low coordination will bind more strongly to adsorbed alkyl chains giving more opportunity for chain growth, and thus it can be postulated that the surface disorder of the particles is responsible for C_{5+} selectivity rather than the oxide support. The alternative hypothesis that the oxide acts as a reservoir for adsorbed species can also be considered.

The adsorption of hydrocarbons and their binding energies with the surface have been investigated on Ru(0001) [47]. The authors use these data to propose reaction mechanisms to explain the formation of certain FTS products, namely the differences in intermediates and reactions that result in saturated and unsaturated hydrocarbons. The paper concludes that the surface intermediates $-CH$, $-CHCH_3$ etc, react *via* carbene mechanisms. In addition the paper concludes that the final intermediates are 'alkyl-' and 'alkylidene-like' species. This paper effectively identifies and characterises the ruthenium surface as a long chain forming FTS catalyst. This can be taken further and the hypothesis that ruthenium will have a strong influence as a promoter in other (cheaper) FTS active catalysts can be made.

Similar work has been carried out on cobalt metal [48, 49]. Although this work was carried out on cobalt foil and not a single crystal it is still highly relevant. In one case the cobalt is in the form of a thin layer of around 6-8 MLE (monolayer equivalents) on gold and the result reported is a change in selectivity towards shorter chain hydrocarbons. The effect would most likely be from the effect of gold on the electronic properties of the cobalt surface. The gold acts as a weak promoter

even when not in solid solution changing the electrochemical potential of the cobalt. However at the higher temperature used stated in this paper, the gold has a high probability of diffusion into the cobalt layer which would significantly increase the effect of Au on the surface chemistry. Also to be considered is the relative thickness of the cobalt layer, suggesting this effect to be negligible. If the growth is less homogeneous, however, the gold could have a fairly significant effect.

Supported Nanoparticles

The following step in complexity in modelling real catalysts involves the deposition of bimetallic particles (*via* sequential or co-deposition) onto planar oxide surfaces. In theory, when the metals are very similar and the interaction of the metals with the oxide support is relatively weak, the particles should be fairly uniform in size and have a good distribution of each element throughout the particles. More often small differences in atomic size, electron affinity or surface free energy will cause one metal to segregate preferentially to the surface of the particles [50, 51]. Metals which are immiscible in the bulk usually form separate particles [52], but in some circumstances mixing can occur in the surface layers due to lowering of surface energies [53].

Aside from the possible added contribution to the catalytic chemistry from the oxide, the changes in particle morphology and dispersion are also of great importance. Following the above argument to reduce costs a high dispersion (small particle size) would be desired to minimise the total ratio of mass to surface area. However, the effect of reducing particle size changes the electronic structure of the particle [38], where the reduction in the number of atoms (quantum size effect) and phonon interaction with the support results in the valence band changing. These considerations convey the importance of research on model oxide materials in surface science to 'bridge the materials gap'.

Among the methods of preparing oxide surfaces in UHV systems there are a number of different model surfaces that can be prepared in order to examine metal particle behaviour on oxides. The preparation technique of the oxide is designed to produce a balance between creating an accurate model of a real support while allowing surface analysis techniques to be employed. Alumina and silica single crystals, pure sapphire and quartz respectively, are both insulating materials. This prevents the use of STM and other techniques where samples need to be earthed for current drain, including argon bombardment for cleaning (*Chapter 2*).



Ultra thin layers of alumina [37-39] and silica [54-56] are routinely deposited onto a conducting substrate for surface investigations. Characterisation of these surfaces indicates the surface structure and chemistry are close representations of the bulk oxides [39, 54]. A drawback to this type of preparation is that in some cases a small degree of porosity occurs, resulting in the metal substrate being exposed. The choice of substrate, therefore, is governed by the continuity of the oxide film.

Titania crystals are conducting and can be used for analysis where a current drain is required. Due to the reducible nature that makes it conducting, the surface chemistry of titania is relatively complex. Care must be taken in selecting the method of preparation because the surface chemistry and structure change dramatically [30] which would then affect the chemistry of the metal particles as discussed previously. The preparation techniques in this paper show that in a UHV chamber the best surface can be obtained by controlling the temperature during oxidation. If the crystal is at an elevated temperature and exposed to oxygen, titanium interstitials will diffuse to the surface growing new TiO₂ layers. This would effectively destroy the smooth nature of the surface making it difficult to obtain well controlled data.

After the oxide surface is obtained deposition of the metals is carried out using methods described (*Chapter 6*). The growth of cobalt metal particles on the oxide is determined by the thermodynamics and kinetics of all surface processes: Nucleation, adsorption, desorption, coalescence, diffusion, and layer growth. The adsorption and surface movement of incident atoms is detailed by Wadley *et al* [57] by reviewing computational analysis of cobalt layer growth on cobalt (0001) crystals in UHV conditions. The data presented in this paper describe the calculated binding energies for cobalt adsorbing into hcp, fcc and step edge sites and considers the effect of vapour atom energy distribution and surface temperature (seen in experimental conditions to have a pronounced effect on particle morphology [43]). The data show differences of *ca.* 5% in the binding energies between fcc and hcp sites and on the terraces and 12% at the step edges (hcp is the most favourable). This greater preference of structure at the step edge states that adatoms incident on the surface are more strongly influenced by the underlying layers at the step edge.

For atoms of cobalt on an oxide substrate it can be hypothesised that during 2D layer growth, diffusing atoms will assume fcc sites on an fcc substrate or hcp on an hcp substrate. This can be extrapolated back to heterogeneous nucleation, as seen to be the primary mechanism for cobalt particle growth [43], where atoms will assume the underlying structure as they form around the

nucleated atom. Additionally, it is known that cobalt undergoes a phase change above 700 K [45] from hcp to fcc and at room temperature the structure may easily be affected by the preparation conditions and the oxide support as well as the environment surrounding the particles after preparation. In addition the structure of bulk cobalt is shown to be highly dependent on particle size [58] – hcp structure is more stable in larger particles. From this it can be postulated that overall the first layers of cobalt in a particle will assume the structure of most substrate materials.

Research on oxide supported cobalt has been reported using alumina [59-61], silica [62-64] and titania [65]. Within the field of catalysis there is no clear consensus on what effects each of the oxide materials has on the active metal [9]. Generally titania appears to be more reactive and cobalt is prone to encapsulation or reaction that results in the formation of cobalt titanates.

Cobalt has been studied on alumina a number of times using a range of different techniques for characterisation. The cobalt has been deposited using various techniques including; Pulsed Laser Deposition (PLD) [60], target sputtering deposition [61], E-beam evaporation [60] and standard thermal evaporation [59] each of which provide a reproducible cobalt surface with minor differences in morphology for PLD. All of the papers mentioned concentrate on structure and particle size distribution. Dureuil *et al* [59] put together a comparison of PLD and thermal evaporation at different temperatures and cobalt doses followed by discussion of the kinetic basis of the differences in particle morphology and conclude that the pulsed nature of PLD results in the coalescing of particles in between pulses. Overall the shared view of the structure of deposited cobalt is that it forms spherical fcc particles which become oblate as particle size increases. Additionally annealing, dosing at higher temperature and larger doses create fewer larger particles.

The silica-cobalt studies [62-64] focus on the postulated deactivation by oxidation in FTS conditions. The samples are prepared in UHV using a thin film of silica on silicon with cobalt deposited by evaporation and analysed using RBS, AFM and various PES techniques. The paper finds that oxidation is difficult under reaction conditions and that the tendency towards oxidation decreases with increasing particle size. In working reactors however, oxidation is seen to be a major contributor in catalyst deactivation [32].

Also studied is a cobalt platinum nanoparticle system on silica by Niemantsverdriet *et al* [65]. This paper studies catalysts for hydrogenation of crotonaldehyde, relevant as the reaction is very similar to CO hydrogenation. The samples, prepared by the spin coating technique, were

characterised using Rutherford Backscattering Spectroscopy (RBS), otherwise known as High Energy Ion Scattering (HEIS), as well as AFM and various photoemission spectroscopic techniques. The most relevant results concern greater reduction of cobalt when alloyed with platinum. The results from these studies have also been seen in several catalysis studies [9] where noble metal promoters improve the reducibility of the cobalt.

Work on the cobalt/palladium system has been carried out using various probe techniques by Freund *et al* [66, 67] covering differing palladium concentrations and looking at the effect of oxidation. XPS, STM and CO-TPD are used to analyse the effects of changing cobalt composition on the oxidation state of cobalt, the structure and the size distributions of the nanoparticles and what correlated effects occur for the adsorption of CO and the susceptibility to oxidation. XPS data describe palladium as having a positive effect on the susceptibility to oxidation as revealed by an increase in intensity of the cobalt peak assigned to Co^0 . The CO-TPD plots also display a dramatic change in the desorption of CO across a range of Pd compositions. Pure palladium particles display a relatively high desorption temperature consistent with a strong bonding to CO and cobalt displays two peaks at room temperature and 400 K. Bimetallic particles between 30-70% cobalt display only one peak at *ca.* 350 K.

1.5 Aims of the Thesis

The main aim of this thesis is to contribute to an improved understanding of cobalt based Fischer-Tropsch catalysts using surface science techniques. Structural, compositional and chemical analysis will be carried out on model catalyst surfaces grown on single crystals for this purpose.

In *Chapter 3*, MEIS and STM are used to examine the growth of Co on Pd{111} and to characterise the structure of CoPd alloys created by thermal treatment of thin Co films. In *Chapter 4*, the interaction of oxygen with CoPd alloys on Pd{111} is investigated with MEIS as is the structure and the thermal behaviour of a cobalt oxide film on Pd{111}. *Chapter 5* focuses on the investigation of the adsorption of catalytically relevant gas phase species (CO, H₂ and Syngas) on CoPd alloys on Pd{111} with MEIS and RAIRS. In Particular the influence of the composition and partial pressure of the gas phase on the composition of the bimetallic surface is examined. *Chapter 6* examines the growth and annealing behaviour of Co particles on oxide and mixed oxide surfaces using MEIS and TPD.

1.6 Bibliography

- [1] Fischer F., Tropsch H., *Über die Herstellung synthetischer Kohlenwasserstoffe (Synthol) durch Aufbau aus Kohlenoxyd und Wasserstoff (About the production of synthetic oil mixture (Synthol) through the formation of carbon monoxide and hydrogen)*, Brennst. Chem. 4 (1923), 276
- [2] Vannice M.A., *Synthesis of hydrocarbons from CO and H₂*, Catal. Rev. Sci. Eng. 14 (1976), 153-161
- [3] Demirbas A., *Progress and recent trends in biofuels*, Prog. Energ. Combust. 33 (2007), 1-18
- [4] Naito S., *Methane conversion by various metal, metal oxide and metal carbide catalysts*, Catal. Surveys from Japan 4 (2000) 3-15
- [5] Kolasinski K.W., *Surface Science; Foundations of Catalysis and Nanoscience*, ISBN: (2002), p220
- [6] Cottrell T. L., *The Strengths of Chemical Bonds, 2nd ed.*, Butterworths, London, 1958
- [7] Attard G. and Barnes C., *Oxford Chemistry Primers: 59 – Surfaces*, Oxford University Press (1998), ISBN: 0-19-855686-1
- [8] www.metalprices.com, Viewed: September 2011
- [9] Khodakov A. Y. et al, *Advances in the development of novel cobalt Fischer-Tropsch catalysts for synthesis of long-chain hydrocarbons and clean fuels*, Chem. Rev. 107 (2007), 1692-1744
- [10] Somorjai G. A., *Catalytic hydrogenation of carbon oxides – a 10-year perspective*, Appl. Catal. A 186 (1999), 355-362
- [11] Dongyan X. et al, *Reaction performance and characterisation of Co/Al₂O₃ Fischer-Tropsch catalysts promoted with Pt, Pd and Ru*, Catal. Lett. 102 (2005), No's 3-4
- [12] Nobuntu N. et al, *The preparation and study of sol-gel synthesised Co/Zn/TiO₂ Fischer-Tropsch catalysts*, Appl. Catal. A 317 (2007), 195-203
- [13] Besenbacher F. et al, *Design of a surface alloy catalyst for steam reforming*, Science 279 (1998), 1913-1915
- [14] Molenbroek et al, *Structure and reactivity of Ni-Au nanoparticle catalysts*, J. Phys. Chem. B 105 (2001),
- [15] Lahtinen J. et al, *Role of readsorption during CO hydrogenation over cobalt model catalysts*, J. Mol. Catal. 91 (1994), 387-397
- [16] Leite L. et al, *Promoting effect of gold on the structure and activity of Co/kaolin catalyst for the 2,3-dihydrofuran synthesis*, Catal. Comm. 3 (2002), 341-34
- [17] Kim K. et al, *Characteristics of cobalt thin films deposited by remote plasma ALD method with dicobalt octacarbonyl*, J. Electrochem. Soc. 154 (2007), H177-H181
- [18] Niemelä M. K. et al, *Preparation and characterization of Co / SiO₂, Co-Mg/SiO₂ and Mg-Co / SiO₂ catalysts and their activity in CO hydrogenation*, Top. Catal. 2 (1995), 45-57
- [19] Niemelä M. K. et al, *The effect of the precursor on the characteristics of Co/SiO₂ catalysts*, Appl. Catal. A 147 (1996), 325-345
- [20] Niemelä M. K. et al, *The activity of the Co/SiO₂ catalyst in relation to pretreatment*, Appl. Catal. A 156 (1997), 319-334
- [21] Coulter K. E. et al, *Effects of activation on the surface properties of silica-supported cobalt catalysts*, J. Catal. 154 (1995), 56-64

- [22] Salavati-Niasari M. *et al*, Preparation of cobalt nanoparticles from [bis(salicylidene) cobalt(II)]-oleylamine complex by thermal decomposition, *J. Magn. Magn. Mater.* 320 (2008), 575-578
- [23] Don Keun L. *et al*, Preparation of monodisperse Co and Fe nanoparticle using precursor of M₂+oleate₂ (M = Co, Fe), *Curr. App. Phys.* 6 (2006), 786-790
- [24] Sei-Jin O. *et al*, Mossbauer analysis on the magnetic properties of Fe-Co nanoparticles synthesized by chemical vapour condensation process, *J. Magn. Magn. Mater.* 280 (2004), 147-157
- [25] Wang Z. H. *et al*, Characterization of Fe-Co alloyed nanoparticles synthesized by chemical vapor condensation, *Mater. Lett.* 57 (2003), 3560-3564
- [26] Huaming Y. *et al*, Mechanochemical synthesis of cobalt oxide nanoparticles, *Mater. Lett.* 58 (2004), 387-389
- [27] Zhao Q. *et al*, UHV/CVD growth of Co on Si(001) using cobalt carbonyl, *Appl. Surf. Sci.* 219 (2003), 136-142
- [28] Nowitzki T. *et al*, Oxidation of alumina-supported Co and Co-Pd model catalysts for the Fischer-Tropsch reaction, *J. Phys. Chem. C* 111 (2007), 8566-8572
- [29] Mochizuki T. *et al*, Novel preparation method of highly active Co/SiO₂ catalyst for Fischer-Tropsch synthesis with chelating agents, *Catal. Lett.* 113 (2007), 165-169
- [30] Matthey D. *et al*, Enhanced bonding of gold nanoparticles on oxidized TiO₂(110), *Science* 315 (2007), 1692-1696
- [31] Van de Loosdrecht J. *et al*, Cobalt Fischer-Tropsch synthesis: Deactivation by oxidation?, *Catal. Today* 123 (2007), 293-302
- [32] Tsakoumis N. E. *et al*, Deactivation of cobalt based Fischer-Tropsch catalysts: A review, *Catal. Today* 154 (2010), 162-182
- [33] Lietti L. *et al*, Fischer-Tropsch synthesis on sulphur poisoned Co/Al₂O₃ catalyst, *Appl. Catal. A* 330 (2007), 49-56
- [34] Koerts T. *et al*, A low temperature reaction sequence for methane conversion, *Chem. Commun.* 18 (1991), 1281-1283
- [35] *The Nobel Prize in Chemistry 2007*, www.Nobelprize.org, 4 August 2011, http://nobelprize.org/nobel_prizes/chemistry/laureates/2007/
- [36] Zubkov T. *et al*, The effect of atomic steps on adsorption and desorption of CO on Ru(109), *Surf. Sci.* 526 (2003), 57-71
- [37] Freund H.-J., *Metal oxide surfaces: electronic structure and molecular adsorption*, *Phys. Status Solidi (B)* 192 (1995), 407-440
- [38] Baumer M. *et al*, Metal deposits on well-ordered oxide film, *Prog. Surf. Sci.* 61 (1999), 127-198
- [39] Kresse G. *et al*, Structure of the ultrathin aluminium oxide film on NiAl(110), *Science* 308 (2005), 1440-1442
- [40] Bowker M., *The Basis and Applications of Heterogeneous Catalysis*, Oxford (1998), ISBN: 0-19-855958-5
- [41] Freund H. -J. *et al*, Bridging the pressure and materials gaps between catalysis and surface science: clean and modified oxide surfaces, *Top.Catal.* 15 No.2-4 (2001), 201-209
- [42] Freund H. -J. *et al*, Preparation and characterization of model catalysts: from ultrahigh vacuum to in situ conditions at the atomic dimension, *J. Catal.* 216 (2003), 223-235



- [43] Min B. K. *et al*, *Support effects on the nucleation, growth and morphology of gold nanoclusters*, *Surf. Sci.* 600 (2006), L7-L11
- [44] Sykes E. C. H. *et al*, *Nucleation, growth, sintering, mobility and adsorption properties of small gold particles on polycrystalline titania*, *J. Phys. Chem. B* 106 (2002), 5390-5394
- [45] Geerlings J. C. C. *et al*, *Studies of the Fischer-Tropsch reaction on Co(0001)*, *Surf. Sci.* 241 (1991), 302-314
- [46] Geerlings J. C. C. *et al*, *Structure sensitivity of the Fischer-Tropsch reaction on cobalt single crystals*, *Surf. Sci.* 241 (1991), 315-324
- [47] Neurock M. *et al*, *Mechanisms for chain growth in Fischer-Tropsch Synthesis over Ru(0001)*, *J. Catal.* 212 (2002), 136-144
- [48] Lahtinen J. *et al*, *Carbon monoxide hydrogenation on cobalt foil and on thin cobalt film model catalysts*, *J. Catal.* 142(1993), 206-225
- [49] Lahtinen J. *et al*, *The effects of promoters in carbon monoxide hydrogenation on cobalt foil model catalysts*, *J. Mol. Catal. A* (1997), 255-260
- [50] Ferrando R. *et al*, *Nanoalloys: From theory to applications of alloy clusters and nanoparticles*, *Chem. Rev.* 108 (2006), 845-910
- [51] Jia-Wen H. *et al*, *Synthesis of Au@Pd core-shell nanoparticles with controllable size and their application in surface-enhanced Raman spectroscopy*, *Chem. Phys. Lett.* 408 (2005), 354-359
- [52] Besenbacher F. *et al*, *The Chemical Physics of Solid Surfaces, Volume 8*, Elsevier (1997), Chapter 6, 207-257
- [53] Pleth Nielsen L. *et al*, *Initial Growth of Au on Ni(110): Surface Alloying of Immiscible Metals*, *Phys. Rev. Lett.* 71 (1993), 754
- [54] Haire A. R. *et al*, *Influence of preparation conditions on the depth-dependent composition of AuPd nanoparticles grown on planar oxide surfaces*, *Surf. Sci.* 605, 1-2 (2011), 214-219
- [55] Hasunuma R. *et al*, *Interface states of SiO₂/Si(111) observed by an atomic force microscope*, *Surf. Sci.* 443 (1999), L1055-L1058
- [56] Shin H.C. *et al*, *Sputter damage in Si surface by low energy Ar⁺ ion bombardment*, *Curr. Appl. Phys.* 3 (2003), 61-64
- [57] Wadley H. N. G. *et al*, *Mechanisms, models and methods of vapour deposition*, *Prog. Mater. Sci.* 46 (2001), 329-377
- [58] Owen E. A. *et al*, *Effect of Grain Size on the Crystal Structure of Cobalt*, *Proc. Phys. Soc.* (1954), 456-466
- [59] Dureuil V. *et al*, *Growth and morphology of cobalt nanoparticles on alumina*, *J. Cryst. Growth* 233 (2001), 737-748
- [60] Zei M. S., *Epitaxial growth of cobalt cluster on the bare and the oxide film grown on NiAl(100) surfaces*, *Surf. Sci.* 601 (2007), 858-864
- [61] Briático J. *et al*, *Structure of cobalt cluster films obtained by sputter deposition on alumina*, *Eur. Phys. J. D* 9 (1999), 517-521
- [62] Niemantsverdriet J. W. *et al*, *Preparation and characterisation of spherical Co/SiO₂ model catalysts with well-defined nano-sized cobalt crystallites and a comparison of their stability against oxidation with water*, *J. Catal.* 239 (2006), 326-339

- [63] Saib A. M. *et al*, *In situ oxidation study of a planar Co/SiO₂/Si(100) model catalyst with nanosized cobalt crystallites under model Fischer-Tropsch Synthesis conditions*, J. Phys. Chem B 110 (2006), 8657-8664
- [64] Heras J. M. *et al*, *Oxygen adsorption on thin cobalt films. An Auger and work function study*, Vacuum 48 (1997), 651-653
- [65] Borgna A. *et al*, *Pt-Co/SiO₂ bimetallic planar model catalysts for selective hydrogenation of crotonaldehyde*, J. Phys. Chem. B 108 (2004), 17905-17914
- [66] Carlsson A. F. *et al*, *The structure and reactivity of Al₂O₃-supported cobalt-palladium particles: A CO-TPD, STM, and XPS study*, J. Phys. Chem. B 107 (2003), 778-785
- [67] Carlsson A. F. *et al*, *Adsorption and reaction on pristine and oxidised Co-Pd bimetallic particles supported on Al₂O₃ thin films*, Surf. Sci. 545 (2003), 143-153

Experimental



2.1 Sample Preparation

Surface investigations generally focus on measurements carried out on single crystal surfaces. The single crystal has a uniform structure throughout which inevitably translates to the surface providing consistency between experiments. The type of crystal used is decided by the variable being analysed while experimental control is maximised. For example, an investigation of the interaction of CO and H₂ with cobalt on the atomic level without the complication of the effects of the oxide support may lead to the use of a cobalt single crystal, whereas a study which focuses on the interaction of cobalt particles with the oxide support will require the use of a crystal most able to produce a well-defined surface of the given oxide.

Each crystal is cut in a certain direction to expose a surface orientation suitable for the experiments. The most suitable crystal is loaded into a UHV system and at this point the surface will be covered in multiple contaminants, defects and imperfections, most of which arise from being exposed to the ambient environment. The crystal is commonly cleaned using cycles of argon ion bombardment (sputtering) followed by annealing. This essentially strips off the top layers of atoms including the contaminants, then the surface is allowed to equilibrate upon heating. The cyclic nature of the cleaning also gradually removes minor bulk impurities over an extended period of time. The resulting clean, well ordered surface is then used to carry out the experiments.

For investigations detailed in this thesis concentrating on cobalt-palladium bimetallic surfaces, a palladium single crystal cut to expose the (111) facet is employed. The alternate use of a cobalt crystal presents an experimental limitation due to a phase transition of bulk cobalt at 723 K from hcp to fcc, and in reality there is often a mixture of the two phases which is dependent on the particle size and crystal preparation [1]. Preparation of a well ordered single phase of cobalt is therefore extremely difficult.

After the palladium crystal is clean, or an oxide layer has been prepared, the active metallic component (cobalt) is deposited onto the surface. The method used for this is metal vapour deposition in which particles of the given metal are heated to a point where the metal sublimates. Of the various methods this provides the most control of variables because the metal is deposited as a gradual flux of atoms. The difficulty is transferring a large amount of heat energy to the metal within the vacuum system. A number of heating methods are noted below:

Metal filament:- With a filament made of the dosing metal this method is simple and fairly inexpensive. Current is passed through the filament and the surface atoms sublime at a rate determined by the temperature of the filament.

W or Ta filament with metal pieces:- The most conventional and inexpensive method used where pieces of metal wire are clamped onto a metal wire filament (tungsten/tantalum) through which an electrical current is then passed. For some elements the metal will melt before an appropriate flux is obtained and a degree of control is needed to keep the flux high without the viscosity decreasing enough for the metal to drop off the filament. Other issues of concern include deposition of metals with high evaporation temperatures and those that alloy with the filament materials.

K-cells:- Alternatively an evaporation cell or Knudsen cell (K-cell) can be used which heats a small sample in a refractory crucible. This method is usually used for metals that melt before evaporating and partially for higher melting temperatures.

E-beam/Pulsed Laser Deposition (PLD):- For high melting metals the alternative to bulk heating is to superheat the surface of a metal wire. This can be done with electrons accelerated to a high voltage from a circular filament that surrounds the metal wire. A current is passed through this and a high voltage potential applied between the filament and metal causes a cascade of electrons to hit the metal surface, evaporating the surface atoms before heat energy can diffuse. PLD uses laser light passed through a viewport which hits the sample, heating the surface. The disadvantage is that the vapour beam is pulsed as opposed to constant which gives differences in the growth mechanism and as a result changes the morphology [2].

Mini-Furnace (*figure 2.1*):- This deposition method, which bears similarities with a K-cell, has the advantage of being very inexpensive. It has been developed from a number of different examples [3] where a tungsten filament is wound around a ceramic tube and the evaporating metal placed inside. This has been added to by using outer ceramic tubing to reflect and concentrate the heat energy towards the centre allowing a higher possible temperature. The ceramic used is either Al_2O_3 from *Multi Lab*, used for lower melting temperature metals, or yttria stabilised zirconia (YSZ) for higher melting metals. This method supplies a constant vapour beam with a relatively high flux which reduces preparation time for experiments.



Figure 2.1:- Cutaway schematic of the mini furnace doser including the dosing metal in the centre.

The filament methods, initially considered for dosing cobalt, were rejected due to a high failure rate of the filament – the cause was determined to be alloying of cobalt with tungsten at elevated temperatures, resulting in a depressed melting temperature. In comparison the mini-furnace proved to be extremely reliable and had a consistent dosing rate after careful outgassing. For this reason this design was used in all cobalt dosing with the exception of a small number of experiments where cobalt oxide was being deposited (a cobalt wire filament was utilised to avoid contamination due to volatile tungsten oxide).

The substrate candidates for studying oxides and the supported metal nanoparticles are numerous and are chosen to give the most continuous, ordered surface. For example alumina can be deposited on a metal substrate [4] or an aluminium containing crystal can be oxidised [4, 5] resulting in an alumina film. In addition to the requirement for a well ordered surface, the substrate needs to be conducting as pointed out previously, thus ruling out bulk silica or alumina (sapphire). The substrate and preparations used are discussed fully in *Chapter 6*.

2.2 UHV (Ultra High Vacuum) Systems

An ultra high vacuum is a state of vacuum with a pressure below 10^{-8} mbar (10^{-6} Pa, or approximately $1.3 \cdot 10^{-8}$ torr). In surface science, UHV systems are used to kinetically inhibit the adsorption of reactive gases and impurities onto the surface being analysed. These adsorbed gases would contaminate the surface and adversely affect the quality of the data. As seen in the graph below *figure 2.2*, the time taken to form one monolayer (ML) is greatly increased from a few nanoseconds at atmospheric pressure to hours for the pressures obtained in a UHV system (assuming a sticking probability of 1.0). Additionally the UHV system serves to permit techniques using electrons or ions as probes of the surface or techniques that detect and analyse emitted particles of a similar nature. These particles have a very low mean path length in atmospheric pressure and would be unable to reach the sample from the source or from the sample to the detector.

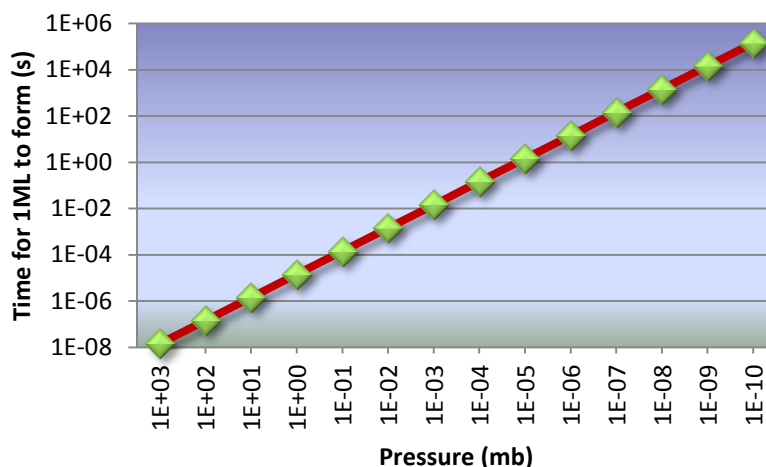


Figure 2.2:- Graph of Pressure versus time for 1 ML to form. Calculated from Hertz-Knudsen equation (Assuming; $T = 298 \text{ K}$, $M = 28 \text{ kg mol}^{-1}$ (molar mass of N_2), Surface sites per $\text{m}^2 = 1 / \text{Area of } \text{N}_2 \text{ molecule}$, Area of $\text{N}_2 \text{ molecule} = \pi r^2$ where $r = \text{van der Waals' radius of nitrogen}$): $Z_w = N_o P / (2\pi MRT)^{1/2}$ [6].

To achieve UHV conditions the gas is expelled from the chamber using turbomolecular pumps, ion pumps and titanium sublimation pumps (TSPs).

A turbo pump is made up of a stack of compressor blades that spins at around 800 Hz. To reduce the total pressure difference over the pump, it is connected to a rotary pump on the high pressure side (atmosphere) to create a fore vacuum of 10^{-2} mbar. The turbo pump is effective across a wide range of pressures, but pumps lighter molecules less effectively since they have a higher velocity at a given temperature compared to heavier molecules.

The TSP is a thick (2 mm) filament of titanium that, when a large current (40 A) is passed through, evaporates the metal from the surface. The titanium vapour is extremely reactive with many gaseous compounds (such as water) and the titanium forms complexes which then stick to the chamber wall in line of sight of the filament. Due to the use of a hot filament, the TSP can only be used below 10^{-5} mbar, but is effective at increasing the overall pumping speed, especially between 10^{-8} and 10^{-11} mbar.

An ion pump is a large chamber coated with titanium with powerful magnets that accelerate ionised gas molecules into the titanium film creating titanium compounds. The pump should not be used above 10^{-7} mbar as the finite titanium becomes saturated with interstitial atoms, but can be used to improve the pumping speed below this pressure.

After the vacuum has been established, the chamber is baked (heated to accelerate desorption from the chamber walls) and current is passed through all the filaments whilst the chamber is hot to remove the majority of adsorbed residual molecular species and minimise readsorption. The final pressures normally obtained with all these methods, in a working system are between 10^{-9} and 10^{-11} mbar. The chamber used for TPD experiments and general testing of components is shown below in *figure 2.3*.

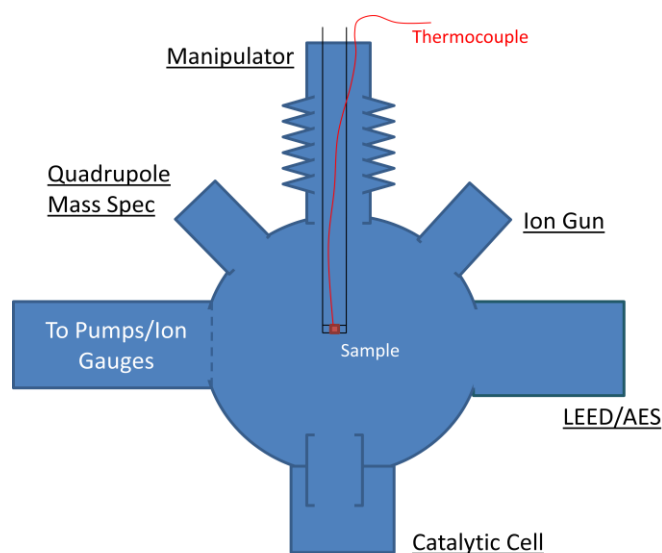


Figure 2.3:- Schematic diagram of TPD chamber used in experiments.

2.3 Low Energy Electron Diffraction (LEED)

LEED is commonly used to check the long range surface order of a surface, giving a limited indication of how clean and well ordered the surface is. The diffraction pattern results when the de Broglie wavelength of the incident electrons is similar to the lattice spacing. This pattern is visualised on a phosphorescent screen and is a 2D Fourier transform of the surface structure where the beam hits the sample. As shown in *figure 2.4*, electrons with the kinetic energies used (25-200 eV) have inelastic mean free paths of less than 1 nm [7] and therefore have very little surface penetration. The resulting data obtained are therefore surface sensitive. Due to their tiny mass, electrons are known to exhibit strong wave-particle duality.

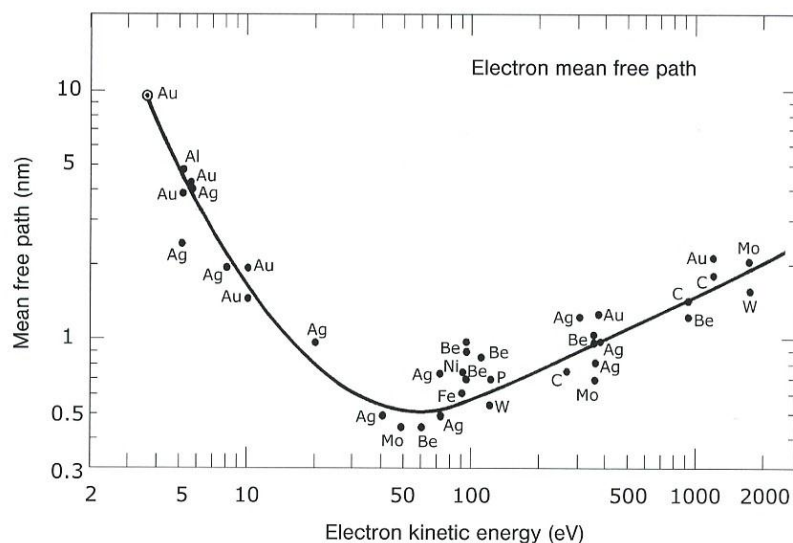


Figure 2.4:- Plot of inelastic mean free path against electron kinetic energy [7].

2.4 Auger Electron Spectroscopy (AES)

Auger Electron Spectroscopy (AES) uses either high energy electrons or X-rays of a single given frequency to eject core electrons from atoms or ions in a sample. The energy supplied to the core electrons is sufficiently high to equal or exceed the binding energy of the electrons. Electrons from outer levels then fall into the vacancy and the resulting energy is absorbed by a third electron (the Auger electron) which is ejected from the atom/ion. The kinetic energy of this detected electron is dependent on each of the energy levels involved so transitions between the equivalent atomic orbitals in two different elements results in Auger electrons of different energy. Therefore the entire spectrum of a pure element is a unique fingerprint. There can be some overlap of individual peaks, but looking at different transitions will identify the elements from one another. One example is where fluorine has a KLL transition of *ca.* 650 eV and cobalt has a LMM transition of 648 eV. Although these peaks are difficult to differentiate the fluorine KLL is a single resolvable energy peak whereas the cobalt LMM is a triplet with two other peaks of similar intensity separated by 50 eV.

The Auger electron energy range is chosen to correspond to a low inelastic mean free path (*figure 2.4*), as it is for LEED, making the technique surface sensitive. One important advantage of AES over LEED is the element specific analysis. For impurities that are expected after being exposed to atmosphere such as oxygen (present as O₂ and water) and carbon (e.g. CO and organic substances) the spectra give a clear view of the level of contamination on a sample. The technique is also valuable for deposition of metals and other compounds; by determining the attenuation of the bulk signal [8] the degree of coverage can be determined, allowing the calibration of the dosing rate.

2.5 Temperature Programmed Spectroscopy (TPS)

TPS is a group of thermodynamic techniques that analyse the thermal energy needed to break bonds in a sample. The decomposition or desorption (in Temperature Programmed Desorption or TPD) can be measured by accurately monitoring the sample mass for changes, or by detecting the desorbed gaseous species directly. These techniques utilise the entire sample and the data are therefore convolutions of different processes. At the heating rates used, desorption features are typically broad due to the statistical distribution of energy at a given temperature. The peak shape itself is determined by the kinetics of the desorption process which in turn are affected by the type of adsorption, dissociative or non-dissociative. The rate of desorption follows an Arrhenius type behaviour described by the Polanyi-Wigner equation [7]:

$$- d\Theta_M / dt = \nu \Theta_M^n \exp (- E_{des} / RT)$$

Where Θ_M is the instantaneous coverage of species M, ν is the frequency factor and n is the kinetic order of desorption. It should be noted that the frequency factor and the desorption energy are coverage dependent. With a linear heating ramp α (Ks^{-1}) used for these experiments the equation becomes:

$$- d\Theta_M / dT = (\nu \Theta_M^n / \alpha) \exp (- E_{des} / RT)$$

For first order desorptions (in which the temperature for maximum desorption, T_{max} , remains constant for different coverages) this relationship can be summarised by the Redhead equation [7]:

$$E_{des} = R T_{max} [\ln (\nu T_{max} / \alpha) - 3.46]$$

As mentioned in the literature study it is also an important technique used to analyse the molecules that desorb from the surface of an active catalyst. CO for example will not be expected to desorb in large quantities from an active FTS catalyst surface under reaction conditions and in the presence of hydrogen. What does desorb will be of great significance to the analysis of the metal because it will indicate the route of reaction or the final products formed. The technique consists of a quadrupole mass spectrometer synchronised with a computer controlled heating mechanism. A number of peaks of expected possible desorbing species are monitored as the sample is heated such as mass 18 for water, mass 28 for CO/N₂ and 44 for CO₂. The apparatus used for TPD experiments is

also equipped with a catalytic cell which the sample can be lowered into for carrying out reactions then the sample can be brought up into the UHV chamber to carry out TPD analysis.

A schematic diagram of the system used for TPD experiment is shown above in *figure 2.3*.

2.6 Scanning Tunnelling Microscopy (STM)

Although a comparatively novel technique, STM (along with Atomic Force Microscopy) has become extremely popular throughout surface research. This is due principally to the capacity for providing direct qualitative information on some aspects of the surface structure, and as a result STM can be more convenient than other surface techniques (e.g. photoemission spectroscopy) that require detailed analysis. STM is limited, however, to surfaces that are conducting and are close to atomically flat. The surface features must also be localised for longer than the imaging time in order to be observed, excluding experiments to detect less massive molecules (e.g. CO), unless imaging is carried out at extremely low temperatures.

STM is based on a quantum phenomenon known as a tunnelling current that occurs (*figure 2.5*) between two points of differing potential – the surface and an atomically sharp tip – as they approach sub atomic distances. This current is exponentially dependent on the distance as described in *figure 2.6* therefore any changes in height will be represented as a change in current. Scanning can be carried out at a constant tip height while monitoring the tunnelling current or, more commonly, by maintaining a constant current while monitoring the height of the tip as it moves across the surface. The relationship between height and current is dependent on the resistivity of the tip-surface junction hence the image is not a pure topographic representation of the surface but contains a strong contribution from the electronic structure at the interface.

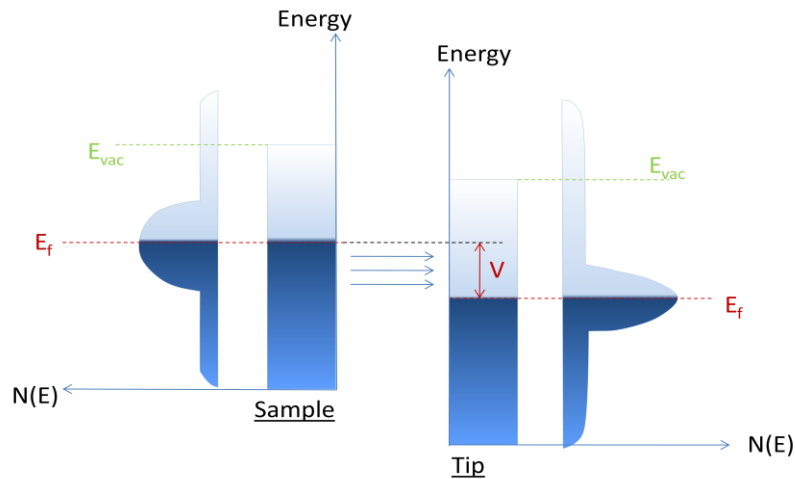


Figure 2.5:- Schematic diagram of energy against number of states, $N(E)$, of a sample and the tip displaying arrows representing the tunnelling current across the potential (V) [7].

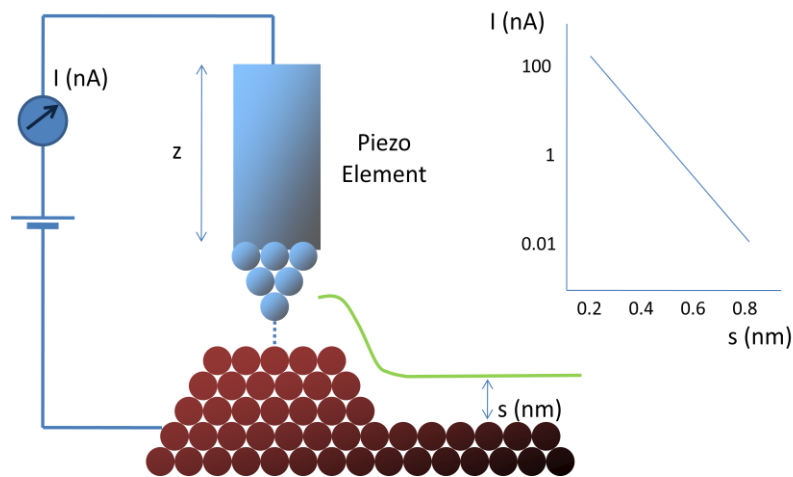
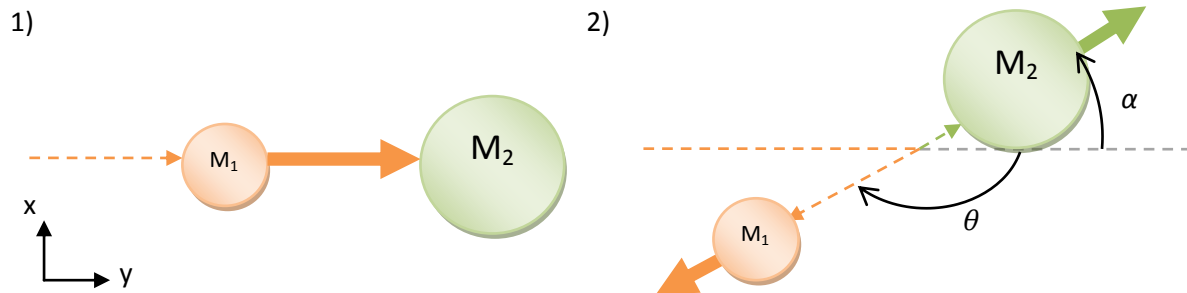


Figure 2.6:- Schematic diagram of STM tip and sample surface connected to current supply along with graph describing the logarithmic relationship between the current and the distance to the sample (s) [7].

Practically STM poses a number of difficulties in obtaining very high resolution, a result of the minuscule currents and distances involved. Difficulties lie in maintaining a fine control on the input and limiting noise – electronic and external vibration – on the output. As a result the apparatus must be isolated from the outside and the internal components, namely the tip and the surface, need to be close to thermal equilibrium to achieve good data. Most importantly the tip must be extremely sharp. The data are actually the convolution of the features of the surface and the tip and therefore the resolution is limited to the shape of the tip within tunnelling distance of the surface. In other words a single atom at the tip is limited to ‘seeing’ single atoms. This tip condition is energetically unfavourable and thus difficult to achieve and maintain.

Experiments are carried out in an Omicron UHV-STM including a preparation chamber equipped with LEED. This UHV system also includes Reflection-Absorption InfraRed Spectroscopy (RAIRS) apparatus. This technique, discussed below in full, is often able to detect the smaller or more mobile features that STM cannot detect therefore the combination is extremely useful.

2.7 Medium Energy Ion Scattering (MEIS)



Conservation of momentum: In the x-direction:-
In the y-direction:-

$$(m_1 u) = (m_1 v_1) \cos \theta + (m_2 v_2) \cos \alpha$$

$$0 = -(m_1 v_1) \sin \theta + (m_2 v_2) \sin \alpha$$

Conservation of energy:-

$$\frac{1}{2} (m_1 u^2) = \frac{1}{2} (m_1 v_1^2) + \frac{1}{2} (m_2 v_2^2)$$

Figure 2.7:- Description of the conservation of momentum and the conservation of energy.

Within this project MEIS is the most important tool for analysing the surface. Ion scattering is based on the classical physics described in *figure 2.7*. When light ions – such as helium or hydrogen – are scattered a substantial fraction of their initial kinetic energy is lost. Ion scattering techniques including MEIS measure this elastic energy loss and use the dependence on the mass of the sample atoms to identify the elements present. This energy loss, which is governed by the conservation of energy, is described below [9]:

$$E_1 = k^2 E_0$$

Where k^2 is given by:

$$k^2 = \left(\frac{(m_2^2 - m_1^2 \sin^2 \theta)^{\frac{1}{2}} + m_1 \cos \theta}{m_2 + m_1} \right)$$

Although unknown elements in the sample surface can be identified by considering the above equations they are usually determined prior to MEIS analysis using AES and so the peaks in the MEIS can be correlated with these expected elements.

In addition to the elastic energy loss, there is inelastic energy loss from ions that scatter from subsurface atoms and have to travel a given distance in and out of the sample. This energy loss is the result of the finite interaction with the electron orbitals of the atoms in the solid sample.

Experimental peaks are referenced with known surface peaks to analyse shifts down in energy – associated with the element being located deeper in the sample. A peak which is broad on the energy scale is indicative of an element occurring at a range of depths. The data collected are used to profile the depth dependent composition of the near surface region.

One of the central features of ion scattering is that data are fully quantitative; a contrast to most other methods used in surface science. The quantitative nature stems from being able to determine, with high accuracy, the scattering probability, defined below [9]:

$$\frac{d\sigma}{d\Omega} = F \left(\frac{z_1 z_2 e^2}{4E \sin^2 \left(\frac{\theta}{2} \right)} \right)^2 g(\theta, m_1, m_2)$$

Ion scattering techniques are distinguished by the initial energy of the ion beam due to the significance of the energy on how the probe ions interact with the surface and how they are detected. At the extremely high energies of Rutherford Back Scattering (RBS), with ion energies generally above 1 MeV, the detectors used are not capable of the energy separation required for monolayer resolution, and the exploitation of ‘blocking’ (discussed below) is not practical. For Low Energy Ion Scattering (LEIS), with ion energies generally below 1 keV, the probability of ion neutralisation as the ion travels through the sample is comparatively high; the resulting ‘visibility’ therefore being limited almost exclusively to the exposed surface atoms. MEIS utilises intermediate energies and can provide data for the surface and near-surface layers.

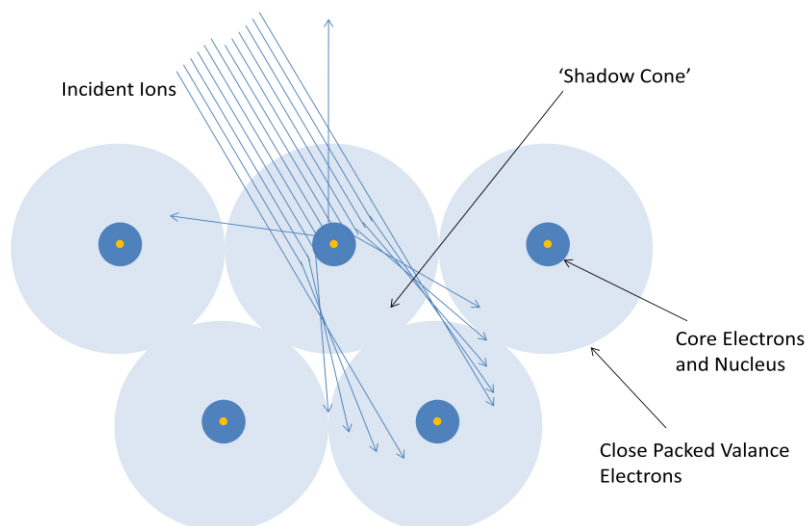


Figure 2.8:- The blocking effect seen in MEIS which occurs for incident ions and escaping ions. At typical ion energies used in MEIS the ions ‘see’ the atoms as reduced spheres and not close packed atoms.

An important feature of ion scattering is the existence of ‘blocking shadows’ in the ion beam behind atoms in the sample which are inversely proportional to the ion energy. At the energies used in MEIS, and in the correct geometry, the ion ‘shadow’ of the surface atoms obscures sub-surface atoms, as seen in *figure 2.8*, making them undetectable. Similarly ions scattered in subsurface collisions may be ‘blocked’ from reaching the detector by atoms nearer the surface illustrated schematically in *figure 2.9*. This phenomenon is manifested in the data as a blocking channel. After the desired atoms are ‘illuminated’ by choosing the correct alignment, the analyser angle is set to pick up a range of different outgoing angles corresponding to the relevant blocking channels. The exact angles chosen depend on the type of crystal structure being analysed and the depth to which data are to be collected from.

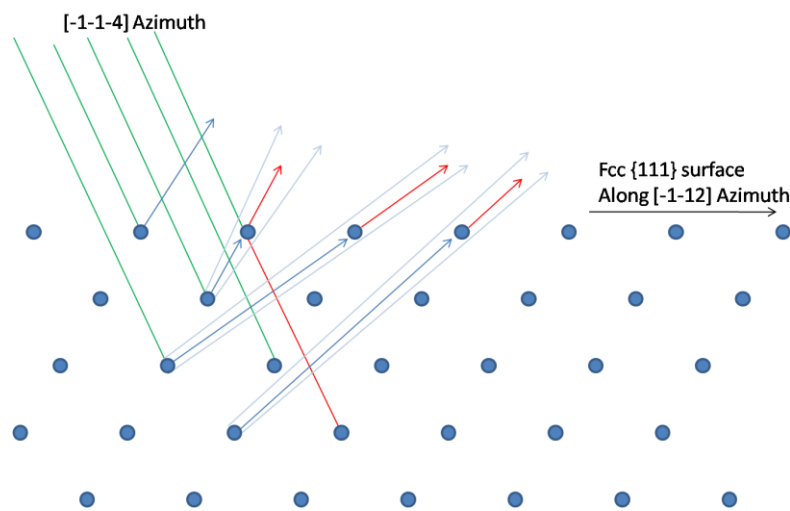


Figure 2.9:- Schematic diagram showing alignment chosen to illuminate top four layers. This specific alignment results in blocking to occur for the 2nd, 3rd and 4th layers within a low range of angles allowing data to be collected in one scan.

Below in *figures 2.10 and 2.11* [10] are diagrams of the MEIS equipment used at STFC Daresbury Laboratory, UK. The ion energy used is usually 100 keV, but the source at Daresbury is capable of 60-200 keV. The ions from the source are accelerated to the required energy and focused into a highly collimated beam by a series of electromagnetic lenses. The crystal is held in a goniometer which can be rotated in three dimensions to allow alignment of the crystal with respect to the beam. The high energy and angular resolution of the data is possible due to the unique detector used. Sample preparation is carried out in a dedicated preparation chamber and then transferred to the goniometer for MEIS data acquisition.

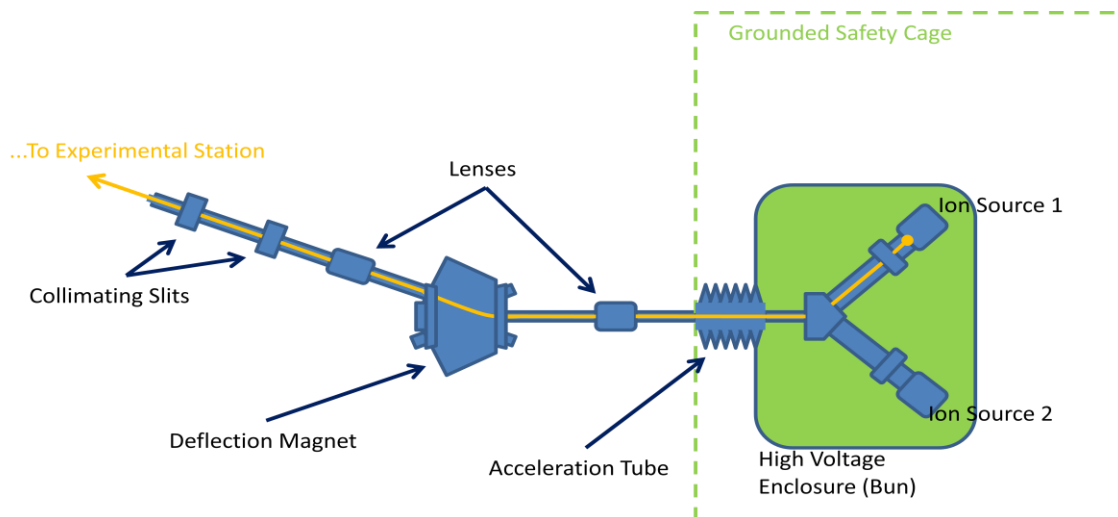


Figure 2.10:- Ion sources and beamline. Gaseous helium/hydrogen is ionised and focused into a beam which is then sent through to the scattering chamber in the experimental station where the sample is scanned.

The data are collected and stored as a 2D tile (an example of which is given in figure 2.12) of scattered ion intensity as a function of scattered ion energy and scattering angle. The detector is limited to energy and angle ranges of 1.442 keV and 25.67° respectively, and therefore multiple tiles are collected and joined together; giving a full 2D plot that includes all the elements and blocking channels of interest. These data are a convolution of scattering events involving different elements across a range of depths, and to extract useable quantitative information the data require detailed analysis.

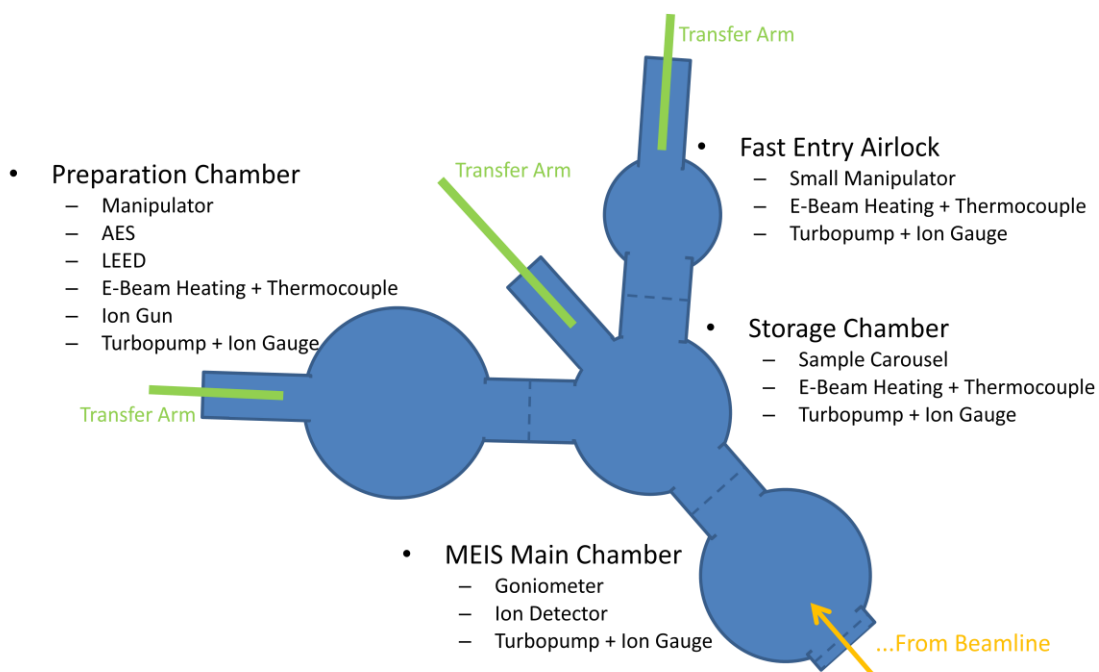


Figure 2.11:- Experimental station showing different chambers and the tools each is equipped with for sample preparation and storage while waiting to be scanned.

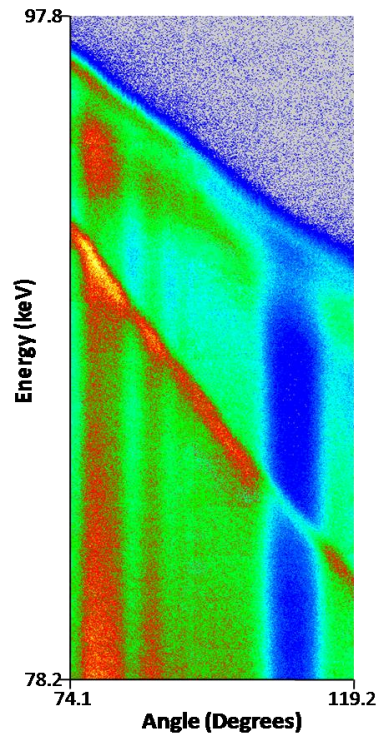


Figure 2.12:- Example of the combined 2D data tile collected using MEIS (approximate beam energy, 100 keV) for a CoPd alloy film on Pd{111}. Notable features include the blocking channels running vertically and the peaks for palladium and cobalt sloping across the tile.

For analysis, the data require separation into component parts. This is first accomplished by taking integral cuts over a small range of angles (depending on the sample, between 0.1° - 10°) within each blocking channel producing a plot of number of counts against ion energy. Each peak can be integrated and normalised for stopping powers as provided by the SRIM code [11] and scattering cross sections (as described in the equations above) of each element giving the relative intensities of each peak. By comparing these intensities in blocking channels which correspond to 1, 2 and 3 layer alignment, the composition in each layer can be determined [12]. This method provides sufficient information if the surface structure is pseudomorphic with the substrate. Further analysis is done to either confirm whether the surface is pseudomorphic or to characterise any alternative surface structure.

To characterise the structure, the peak(s) that corresponds to the surface layers are integrated across all angles scanned and presented as plots of ion counts versus angle. These data indicate the blocking channels for those surface layers which can be compared against known structures or matched to predicted data plots – calculated using a Monte Carlo based program called VEGAS. This program simulates a small section of the surface in which the atomic positions are modified for each structure. The program then calculates the number of ions that will be detected at each angle then outputs the data in a comparable format to the experimental data which have been

normalised to take into account the scattering cross section. Small changes in the atomic positions are made until the output achieves a best fit to the experimental data. The VEGAS simulations were carried out by Dr T E Jones (School of Chemistry, University of St Andrews).

Structure and composition, once determined, can be compared before and after annealing or exposure to a reagent. MEIS used in this way has the potential to detect very small changes in the surface which are dependent on reagent exposure time, dose, pressure and temperature.

2.8. - Reflectance Absorption InfraRed Spectroscopy (RAIRS)

Infrared (IR) spectroscopy is a technique commonly used in catalysis and surface science. Its different forms are defined generally by the experimental geometry and the sample under analysis represented below as a series of schematics in *figure 2.13*.

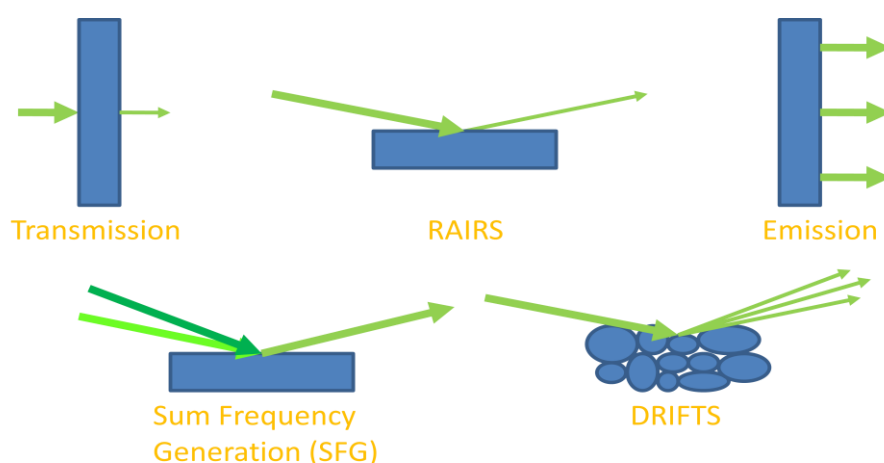


Figure 2.13:- Schematic summary of the various vibrational spectroscopies.

Transmission is often unworkable due to the opaque nature of the sample to infrared; the solution is to reflect the beam on the single crystal sample, known as RAIRS. The sensitivity of RAIRS is relatively low due to the small number of molecules on the sample (10^{15} molecules cm^{-2}) and so the reflection is carried out at grazing incidence with polarised radiation. The grazing incidence increases the path length of the IR radiation and simultaneously the radiation undergoes constructive interference only along the vector perpendicular to the surface. These factors contribute to an increase in the sensitivity, and in addition there is an enhancement as the beam passes through the adsorbate film twice (before and after reflection). The frequencies involved correspond to the energies involved in vibration of bonds. Therefore the technique can be used to identify unknown species, to establish bonding strengths or bonding sites and geometries.

These properties can only be examined in molecules with a dynamic dipole moment. This has the interesting result that the data can offer additional information on the orientations of adsorbed species. This is a result that arises when the electron 'sea' in the metal surface which moves to form an induced mirrored dipole in response to the dipole of an adsorbed species. When the dipole is parallel to the surface the 'mirror' image dipole will align in the opposite direction causing a loss of signal and when the dipole is perpendicular to the surface the IR absorption is enhanced. This effect is shown schematically below in *figure 2.14*.



Figure 2.14:- Schematic diagram of dipole alignment on a metal single crystal.

Although the use of RAIRS usually focuses on examining the state of an adsorbate or determining unknown reaction products, simple gas adsorbates (e.g. CO) may be utilised to provide information on the nature of the surface sites available. This is accomplished by referencing the data describing the surface of interest with studies of related basic systems. For example data describing the surface of a bimetallic alloy can be compared to publications on each individual metal using the same adsorbate.

As mentioned previously the RAIRS apparatus is combined with STM along with LEED and facilities for ion bombardment. The polarised infrared beam is directed into a dedicated UHV chamber through an alkali halide window to the sample allowing *in situ* measurement in a controlled atmosphere. The outgoing beam passes through another alkali halide window to reach a semiconductor based photodetector. Outside the UHV chamber the detector (mercury cadmium telluride detector cooled with liquid nitrogen) and mirrors are contained inside boxes which are purged with dry nitrogen with the intention of removing H₂O and CO₂ from the path of the infrared beam, and thus limiting absorption of the IR beam by these species.

RAIRS is a holistic technique which allows it to detect molecules with short retention time, however, this means the absorption from molecules in different states will convolute together which can make it complicated determining which sites molecules bind to. After considering the sensitivity enhancements, RAIRS continues to have relatively weak signal compared to other infrared methods and it is not readily quantifiable.

2.9 Bibliography

- [1] Owen E. A. *et al*, *Effect of Grain Size on the Crystal Structure of Cobalt*, Proc. Phys. Soc. (1954), 456-466
- [2] Dureuil V. *et al*, *Growth and morphology of cobalt nanoparticles on alumina*, J. Cryst. Growth 233 (2001) 737-748
- [3] Wytenburg W. J. *et al*, *Long-lived aluminium evaporation source for controlled, reproducible deposition of clean ultrathin films under ultrahigh-vacuum conditions*, J. Vac. Sci. Tech. A 10 (1992) 3598
- [4] Baumer M. *et al*, *Metal deposits on well-ordered oxide film*, Prog. Surf. Sci. 61 (1999) 127-198
- [5] Kresse G. *et al*, *Structure of the ultrathin aluminium oxide film on NiAl(110)*, Science 308 (2005) 1440-1442
- [6] Kolasinski K. W., *Surface Science; Foundations of Catalysis and Nanoscience*, (2002) p183-184
- [7] Niemantsverdriet J. W., *Spectroscopy in Catalysis – An Introduction*, (2007) p40
- [8] Jablonski A., *Quantitative AES: Via the Inelastic Mean Free Path or the Attenuation Length*, Surf. Interface Anal. 15-9 (2004), 559-566
- [9] Tromp R. M., *Practical Surface Science (Second Edition) Volume 2: Ion and Neutral Spectroscopy*, (1992) John Wiley & Sons Ltd
- [10] Bailey P. *et al*, *A medium energy ion scattering study of the structure of Sb overlayers on Cu (111)*, Surf. Sci. 426 (1999) 358-372
- [11] Ziegler J. F., *SRIM-2003*, J.F. Ziegler, Nucl. Instrum. Meth. B. 219–220 (2004), 1027-1036
- [12] Bailey P. *et al*, *Monolayer resolution in medium energy ion scattering*, Nucl. Instrum. Meth. B. 183 (2001), 62-72

*Structural and Compositional Analysis
of CoPd Alloys on Pd{111} using
MEIS and STM*



3.1 Introduction

The goal of understanding cobalt based catalysts (including those with small added quantities of second or third row transition block metals) is discussed in *Chapter 1*. Examining how the bimetallic surface influences, and is influenced by, the adsorption of the gas phase requires the understanding of the structure and composition of the bimetallic surface in an inert atmosphere. This chapter aims to provide this understanding by studying cobalt and palladium across a range of different alloy concentrations. The focus of these experiments is to characterise the crystal structure and the composition of the surface and near surface regimes.

For this purpose a model of the surface consisting of a thin alloy film is created in order to remove the possible influence of additional variables such as the support material and morphology. The bulk structure of cobalt, considered in *Chapter 1*, exhibits a hexagonal close packed (hcp) structure below 723 K, above which the transition is to face centred cubic (fcc). Between room temperature and 723 K the preferred structure is strongly influenced by the particle size [1].

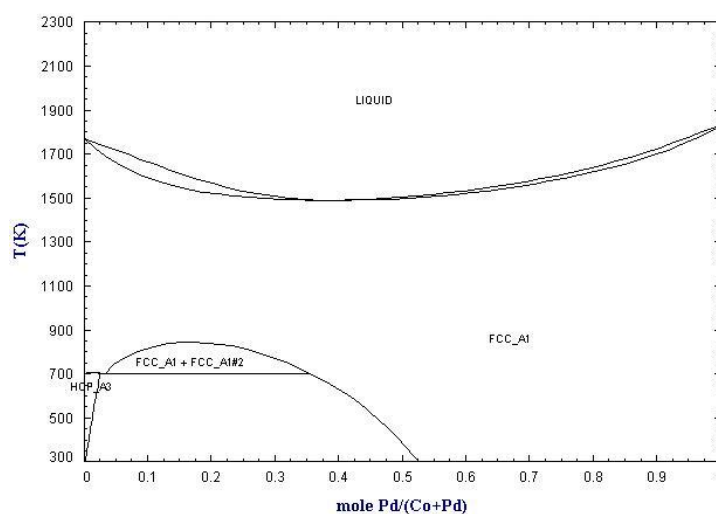


Figure 3.1:- Phase diagram of bulk palladium and cobalt [2].

The behaviour of the full range of cobalt palladium alloys is given for temperatures between 300 and 2300 K in *figure 3.1* [2]. This indicates that the fcc structure is favoured for all but the small composition range of the cobalt rich alloys below 700 K. The lattice mismatch of the Co and Pd alloy is 10.0% (calculated from fcc lattice parameters of 3.5368 [3] and 3.8907 Å [4] for cobalt and palladium respectively) and the heats of atomisation are 426 [5] and 377 kJ mol⁻¹[5] for cobalt and palladium respectively.

The values above are useful for making hypotheses on possible lattice strain and resulting reconstruction that can occur at the surface. Although the bulk structure is indicated as fcc, it is possible for the surface structure to reconstruct in various ways. Such a reconstruction could consist of a continuous hcp alloy overlayer or may also result in phase separation into layers of differing composition. In accordance with the influence of particle size on the structure of cobalt [1] the island size and shape may also influence the surface structure.

Ideally, a range of samples with different bulk alloy compositions would be synthesised and their surfaces examined. This is costly, however, and provides a number of experimental difficulties. The epitaxial growth of one metal on a single crystal of the other metal is a typical method employed in surface research. Subsequent annealing of the sample to create surface alloys is commonly used to avoid the need for bulk alloy samples. The main disadvantage is the influence of the substrate on the metal structure during nucleation and growth cannot be eliminated.

Although there are many examples of this type of research, one study of particular relevance is palladium on Cu(111) investigated by MEIS[6]. The methods used to collect and analyse the data are intended to permit quantitative characterisation of the structure and composition of the surface and near surface layers. As the surface is annealed above 500 K the amount of visible palladium decreases substantially as the metals alloy, causing the disruption to the copper structure several layers deep. Combining these data with STM the authors could confirm their hypotheses of the disruption being associated with inter-diffusion into the crystal or formation of alloy islands.

The growth of cobalt thin films on Pd{111} has been reported by Wasniowska *et al* [7] with deposition at 180, 300 and 550 K, examined using STM. The study indicates cobalt island growth displaying an irregular dendritic morphology at the lower deposition temperature. At the higher deposition temperatures the particles are more regular and hexagonal in shape at 300 K and triangular at 550 K. The islands have a close packed arrangement of atoms incorporated in a dislocation pattern. As a consequence of the lack of pseudomorphic growth, the cobalt is determined (by scanning tunnelling spectroscopy) to be in both fcc and hcp sites.

The sub-monolayer growth of cobalt on Pd(111) is examined more closely by this group in addition to a study on the magnetic properties of cobalt on different palladium surfaces [8-9]. The growth kinetics are strictly controlled, using a dosing rate of $0.001 \text{ ML min}^{-1}$, and as a result, the particles are highly ordered and well defined. Particle growth at room temperature proceeds with

the fcc structure, starting from both fcc and hcp nucleation sites. The growth dynamics are dominated by the cobalt-cobalt interactions, and hence multiple layer islands form with dislocation lines appearing along the [1-10] directions.

The growth of cobalt thin films on Pd{111} has also been examined by [10] using X-ray Absorption Near Edge Structure (XANES) and Extended X-ray Absorption Fine Structure (EXAFS). The results of this study confirm that cobalt grows with the fcc structure and the conclusion is made that the cobalt does not grow in a pseudomorphic manner, indicated by a low mechanical strain. This is also indicated in a surface x-ray diffraction study on Co-Pd{111} [11]. At room temperature there is no spontaneous alloying at the boundary of the two metals [10].

The condition of the surface is expected to change as the temperature increases upon annealing. Initially the cobalt can be expected to diffuse very slowly at room temperature with the structure influenced mainly by the dosing conditions. As the substrate is heated the rates of diffusion will increase significantly, permitting the metals to mix within the timescale of the experiment – providing it is thermodynamically favourable to do so. Additionally, as the temperature increases the most thermodynamically stable state will change and the metals will become increasingly soluble.

3.2 Experimental

The depth dependent structure and composition of CoPd alloys are examined on an fcc Pd{111} crystal substrate [Surface Preparation Laboratories]. This crystal is cleaned using cycles of Ar⁺ sputtering (1.5 keV, 10-20 μ A crystal current) followed by annealing to 1100 K. The condition of the surface is considered clean when a sharp 1x1 LEED pattern can be seen, combined with either an AES spectrum presenting no impurities for the MEIS experimental apparatus, or an STM image indicating a clean surface with large terraces for the STM apparatus.

5 ML of cobalt (1 ML is equivalent to 1.53×10^{15} atoms cm^{-2}) was then deposited using an approximate dosing rate of 0.1 ML min^{-1} . This was checked in the STM apparatus by taking images of the surface at coverages of 0.5, 1, 2 monolayers and at the final coverage. In the MEIS apparatus coverage was calculated from the attenuation of the Pd 330 eV Auger signal and confirmed by measuring the normalised peaks from the MEIS data. This initial coverage provides a starting point consisting of an essentially continuous cobalt overlayer and a high cobalt signal to noise ratio in the MEIS data.

The crystal is subsequently annealed for 5 minutes at increasing temperatures in order to increase the palladium content in the surface alloy. Between each temperature the crystal is cooled to room temperature and then transferred to MEIS/STM for data collection. Measurements were made following annealing at temperature intervals of 50-60 K from 300 (deposition temperature) to 850 K.

During all MEIS data collection, the crystal was in an aligned geometry along the [-1-12] azimuth with the beam incident along the [-1-1-4] direction which corresponds to an illumination of the top three layers of an ideal fcc {111} surface. The detector was aligned to two different scattering angle ranges centred at 86° and 106° – the subsequent data make up the blocking channels in 1-layer, 2-layer and 3-layer geometries of the ideal surface.

From the MEIS data, counts of scattered ion intensity are integrated across a narrow range of scattering angles corresponding to each of the defined blocking channels of the bulk Pd{111} crystal, resulting in plots of ion intensity versus energy. In addition the peaks corresponding to ions scattered from cobalt atoms and those scattered from palladium atoms are integrated as a function of scattering angle to give plots of scattered ion intensity versus scattering angle. These plots are subsequently compared to the scattered ion intensity versus scattering angle plots from an energy

corresponding to the bulk of the Pd{111} crystal. This allows any surface structures disparate to the bulk to be identified; these changes are indicated by changes in the blocking channel positions and intensities.

The VEGAS program described in *Chapter 2* is used to simulate the scattered ion intensity versus scattering angle for a range of possible surface structures for comparison with the experimental results. Initially the cobalt structure is 'grown' in layers on the palladium surface. The cobalt is grown as hcp and fcc structures in two different directions of growth, N and R, corresponding to 0° and 180° rotation of the cobalt layer. Due to the threefold symmetry of the fcc (111) surface these growth directions are not equivalent. Matching the approximate angular position and intensity of the blocking channels to the experimental data provides a structural identification. More complex configurations are investigated if an approximate match is not initially found. From this the best match is finely tuned by altering the relaxation in the surface layers and exact atomic positioning causing small shifts in the simulated blocking channels. A schematic summary of the initial simulated growth modes can be seen in *figure 3.2*.

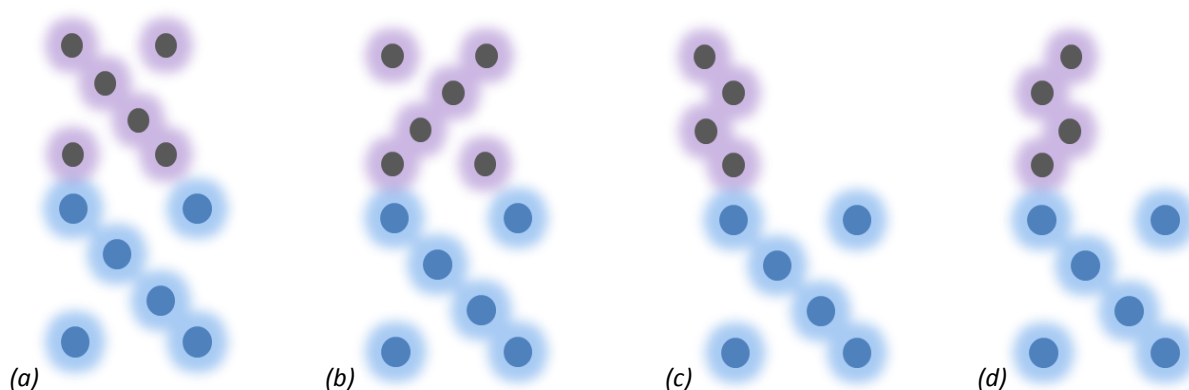


Figure 3.2:- Schematic diagram of the four fundamental simulated atomic arrangements in the cobalt overlayer. These structures include fcc N (a), fcc R (b), hcp N (c) and hcp R (d).

It is important to note that there is a clear discrepancy between thermocouples on the STM/RAIRS and MEIS apparatus. The temperature reading is approximately 75 K higher at 900 K on the MEIS apparatus and diminishes linearly to 0 at 300 K, as judged from the appearance of the crystal upon annealing beyond 850 K during the cleaning procedure. This is additionally confirmed by comparing the experimental results from the intermediate temperature between the two systems – which is discussed below. Temperatures given throughout are given as read experimentally.

3.3 Results

Cobalt on Pd{111} – Medium Energy Ion Scattering

The 1 layer scattered ion intensity versus energy data as a function of annealing for 5 ML cobalt on Pd{111} are shown in *figure 3.3*. Fundamentally, as the temperature is increased, the cobalt peak (84 keV) decreases in intensity as the cobalt is dissolved into the bulk. In addition the palladium peak initially presents as a 90 keV peak shifted down in energy with respect to the clean palladium surface peak. This peak moves up in energy at 560 K in addition to the appearance of a peak at the energy corresponding to surface palladium (approximately 91.5 keV). As the temperature increases further the surface peak intensity increases and the sub surface peak disappears as the cobalt peak diminishes. At 560 K a diffuse (2x2) pattern was observed with LEED which remained to some extent at 600 K.

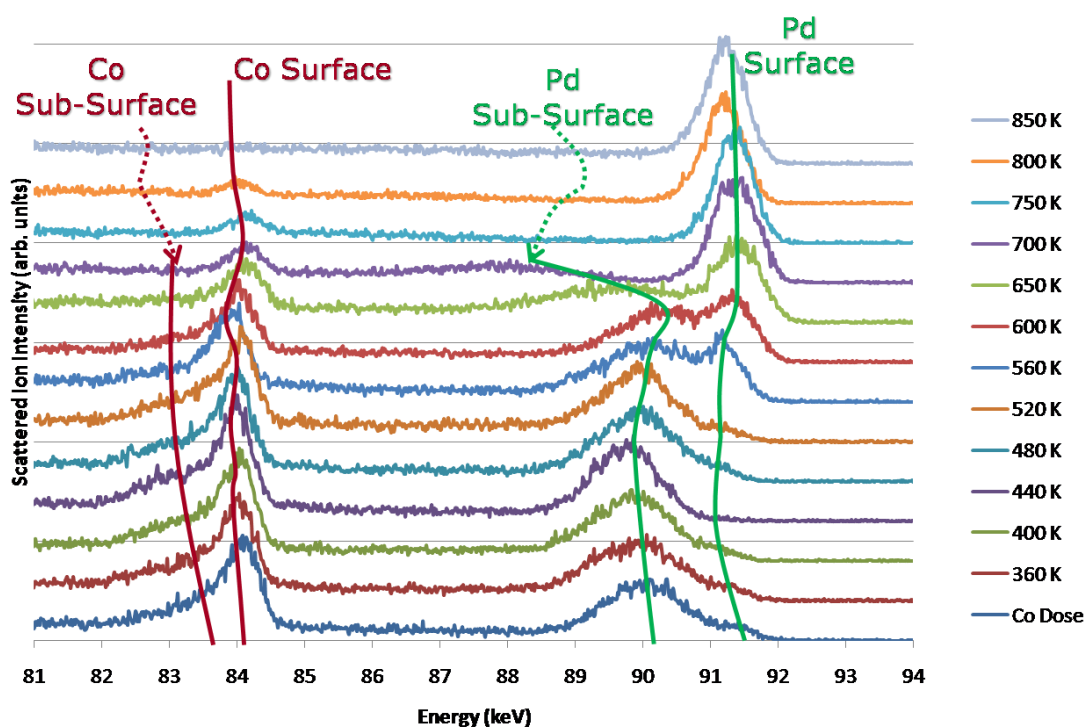


Figure 3.3:- Stacked scattered ion intensity versus energy data for 5 ML cobalt on Pd{111}, sequentially annealed to increased temperatures, annotated to indicate component peaks. The plots are integrated cuts taken from each 2D tile and have had a linear background correction applied.

In *figure 3.4* the integration of the palladium surface and sub-surface peaks (across all angles for which data were collected) are displayed. The data are also normalised to extract the number of visible layers from the scattered ion intensity, explained in *Chapter 2*. The absolute yields of the palladium surface increase with annealing temperature and the sub surface yields decrease – matching the peak intensities in *figure 3.3*. The blocking channels at approximately 84° , 90° and 109° are the 2-layer, 3-layer and the 1-layer channels respectively and correspond to the theoretical fcc

blocking channels at 84.3° , 90.0° and 109.4° . Notable shifts in the blocking channel positions occur between 650 and 700 K, however, relative intensities of the three blocking channels remain constant. It is also important to note the lack of any blocking features besides the regular fcc channels.

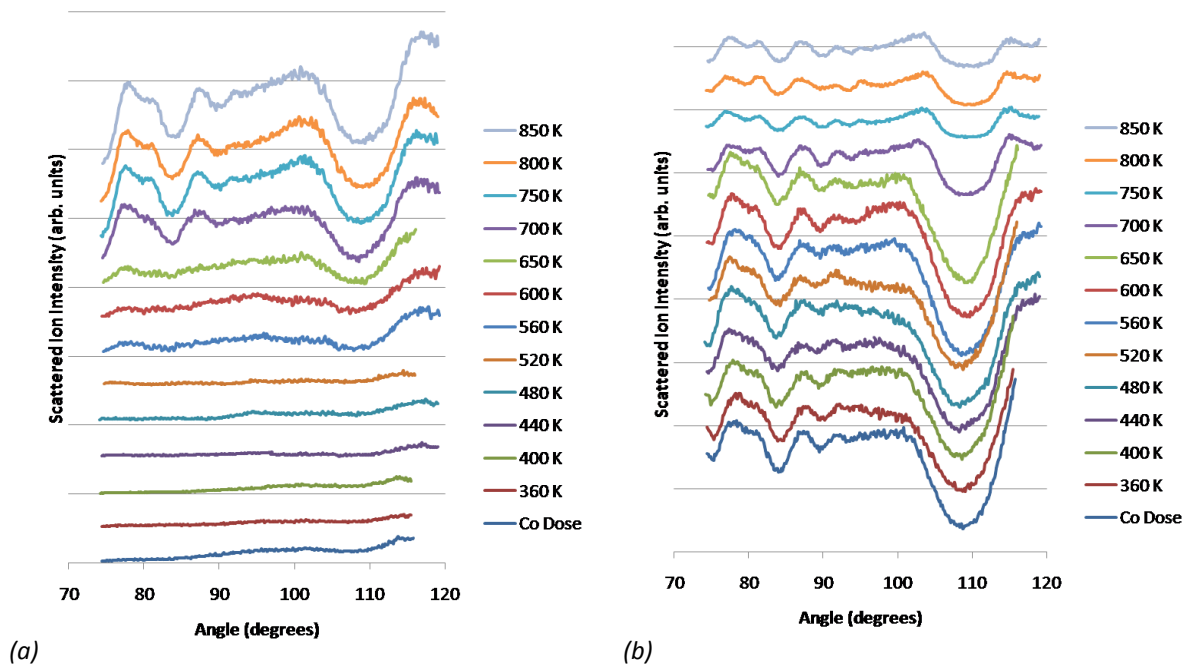


Figure 3.4a:- Angle versus scattering ion intensity – integrated counts for the palladium surface peak. Figure 3.4b:- Angle versus scattering ion intensity – integrated counts for the palladium sub surface peak.

Figure 3.5 displays the integration of the cobalt peak across all angles. These data are subtracted from the convoluted palladium bulk using the IGOR program for each separate channel along the angle axis. The data output is also corrected to give the number of visible layers. Again the absolute yields tie in with the cobalt peak intensities in figure 3.3: The visible cobalt decreases as the annealing temperature is increased. The large blocking channel around 109° corresponds to the 1 layer alignment as the same channel in the palladium spectrum. Other than the primary blocking channel the most apparent blocking channel appears at approximately 83° at the lower temperatures. In addition there are several smaller features observable in the blocking spectra: a channel at 88° is observed after dosing and disappears immediately on annealing to 360 K; and a channel at 97° is observed after dosing and remains visible until 440 K.

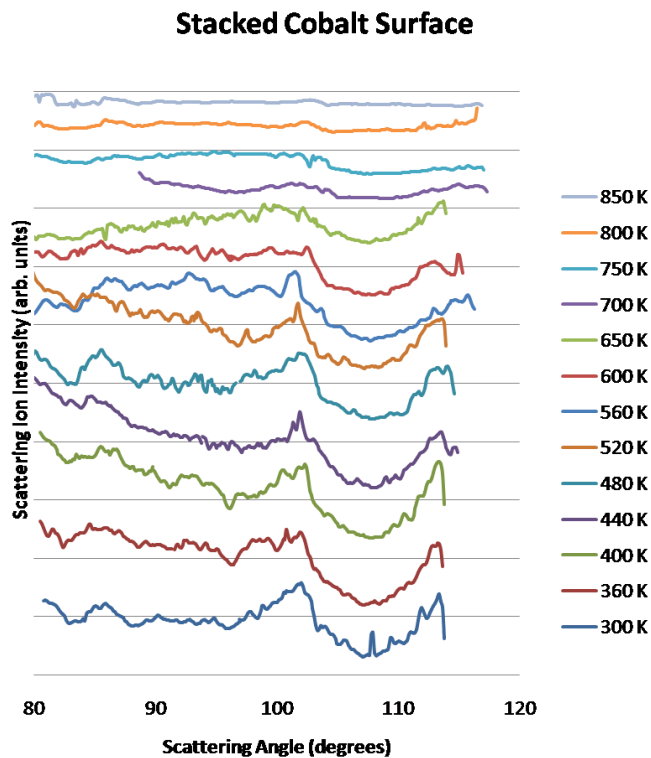


Figure 3.5:- Angle versus scattering ion intensity – integrated counts for the cobalt peak after subtraction of palladium bulk.

Cobalt on Pd{111} – Scanning Tunnelling Microscopy

The deposition of cobalt at 300 K is followed by taking STM images at 0.5 ML (*figure 3.6*) 1 ML (*figure 3.7*), 2 ML (*figure 3.8a*) and after dosing is complete (*figure 3.8b*). The images show particle growth nucleating at step edges and point defects growing with partially hexagonal morphology. The growth of the second layer can be seen before the first layer is complete. The first layer is mostly continuous as the third layer starts. The atomic structure includes a visible dislocation pattern.

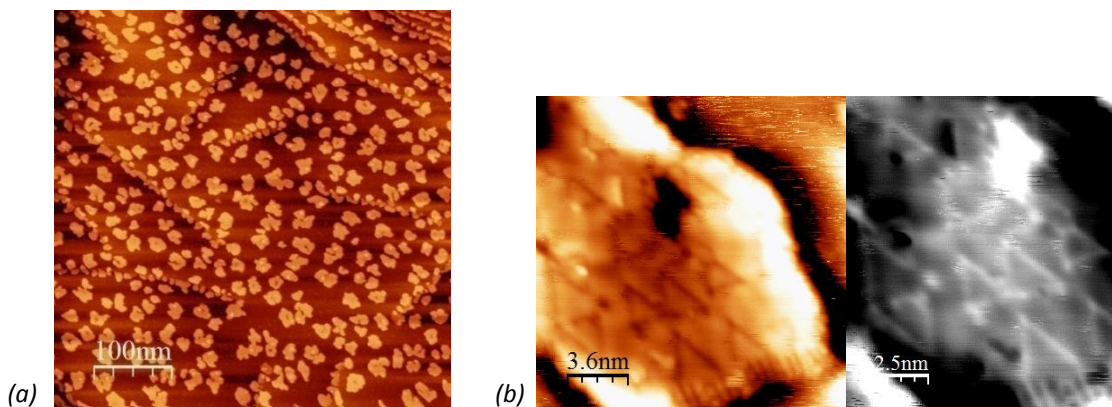


Figure 3.6:- STM images of 0.5 ML of Co on Pd{111}. The images include a scale of 500 x 500 nm (a) $\{V = 1 \text{ V}, I = 1 \text{ nA}\}$ indicating the particle distribution and magnification ($18 \times 18 \text{ nm}^2$) of the particle surface in different contrasts (b) $\{V = 1.37 \text{ V}, I = 0.71 \text{ nA}\}$ indicating the triangular dislocation pattern with an average size of 2.65 nm.

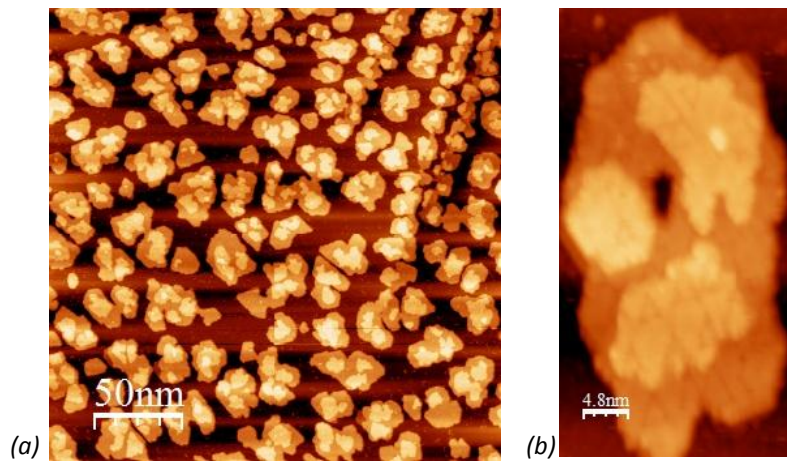


Figure 3.7:- STM images of 1 ML of Co on Pd{111} indicating particle distribution (a) {250 x 250 nm², V = 1 V, I = 1 nA} and detail of the second layer growth (b) {24 x 24 nm², V = 1 V, I = 1nA} with the dislocation pattern still visible.

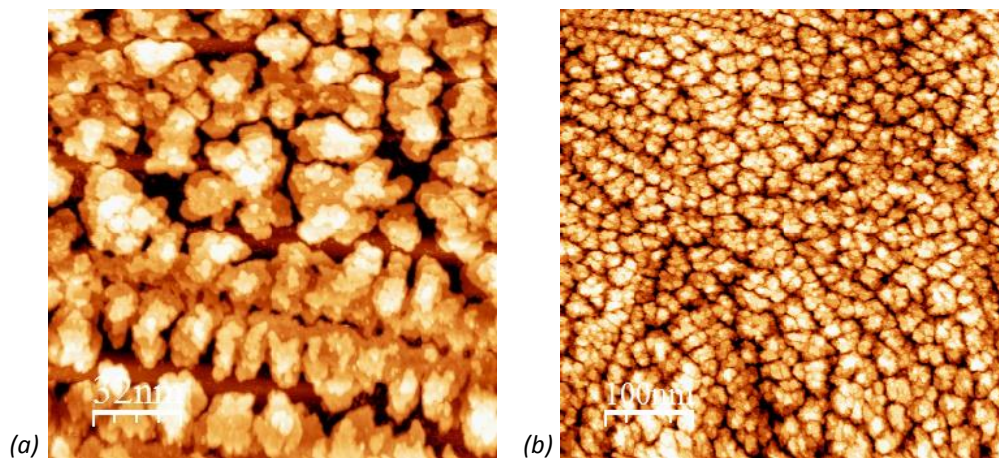


Figure 3.8:- STM images showing particle morphology at 2 ML (a) {160 x 160 nm², V = 1 V, I = 1 nA} and after dosing (b) {500 x 500 nm², V = 1 V, I = 1 nA} Co on Pd{111}. At 2 ML cobalt growth the palladium surface can still be clearly seen.

Once the growth of the Co thin film is complete, the surface is annealed to examine the formation and behaviour of surface cobalt palladium alloys. At lower annealing temperatures the surface appears to remain predominantly unchanged; seen in *figure 3.9*. After annealing to 550 K (*figure 3.9c*) and beyond, the island edges become increasingly ordered whilst the particle like morphology of the overlayer remains – the raised areas corresponding to where the original nucleation occurred. Due to the rough topography, the dislocation pattern seen in *figure 3.6b* could not be resolved after 2 ML of deposition and across the low annealing temperatures.

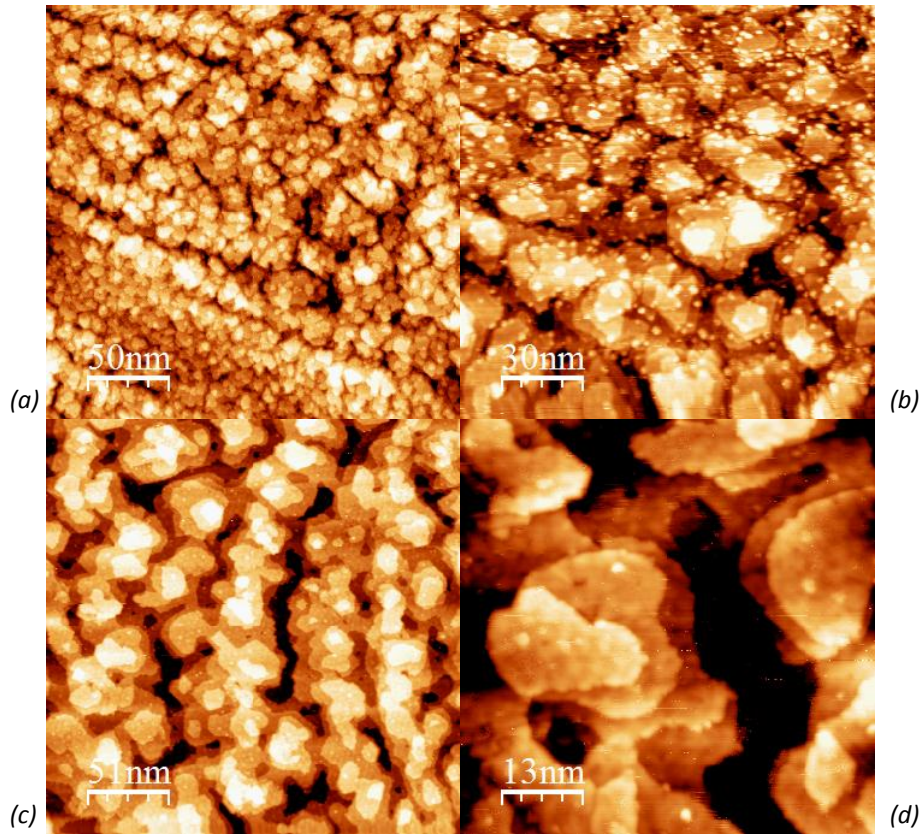


Figure 3.9:- STM images indicating particle type morphology after annealing to 450 K (a) $\{250 \times 250 \text{ nm}^2, V = 1 \text{ V}, I = 1 \text{ nA}\}$, 500 K (b) $\{150 \times 150 \text{ nm}^2, V = 3.14 \text{ V}, I = 1.67 \text{ nA}\}$ and 550 K (c) $\{250 \times 250 \text{ nm}^2, V = 0.7 \text{ V}, I = 1.4 \text{ nA}\}$. In addition, the higher magnification at 550 K (d) $\{66 \times 66 \text{ nm}^2, V = 0.69 \text{ V}, I = 1.55 \text{ nA}\}$ reveals a Moiré pattern with an average unit cell of 3.45 nm.

At 550 K and above, the morphology changes more noticeably. The islands partially coalesce, and the edges become increasingly ordered. This is illustrated by comparing figure 3.9b with figures 3.9c and 3.9d; the smaller features disappear, or combine into larger ordered structures, and the lower layers connect together – becoming increasingly continuous. In addition, the dislocation pattern – visible at low coverages – is replaced by a different Moiré pattern without dislocations (figure 3.9d) with an average unit cell of $3.45 \times 3.45 \text{ nm}^2$.

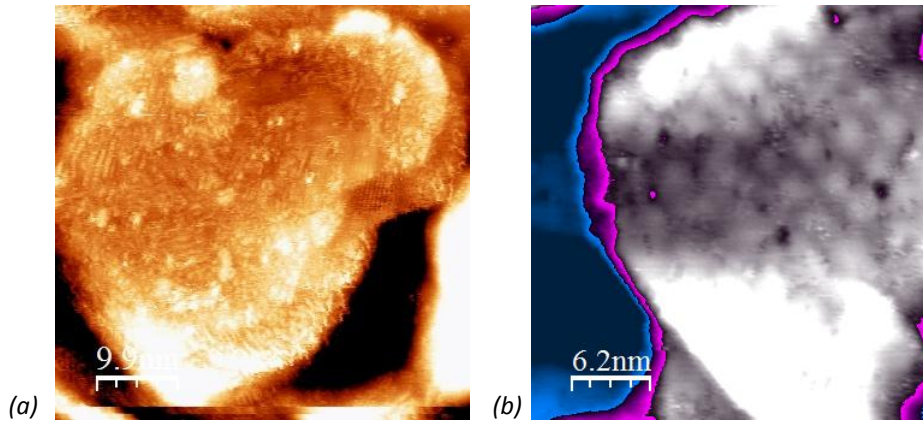


Figure 3.10 STM Images magnified to display a single particle with some reconstruction on the terraces (a) {84 x 85 nm², V = 0.74 V, I = 1.23 nA} and a high contrast image revealing the Moiré pattern (b) {50 x 50 nm², V = 0.5 V, I = 1.39 nA} at 600 K.

At 600 K the Moiré pattern becomes much clearer and is continuous over a large proportion of the surface as indicated in *figure 3.10*. At this temperature the island like morphology remains as it does at 550 K and there is no significant aggregation. However the trends of increasing ordering and agglomeration are still seen as well as the noted increasingly widespread Moiré pattern. In addition to the Moiré pattern further detail is also evident in some images which manifest as domains with a corrugated appearance (*figure 3.11*). The rows that form the corrugation are not well resolved in the images taken after annealing to 600 K, but do appear to be a feature of the majority of the surface. The extent of the individual domains is limited at this annealing temperature and along the rows there are numerous breaks.

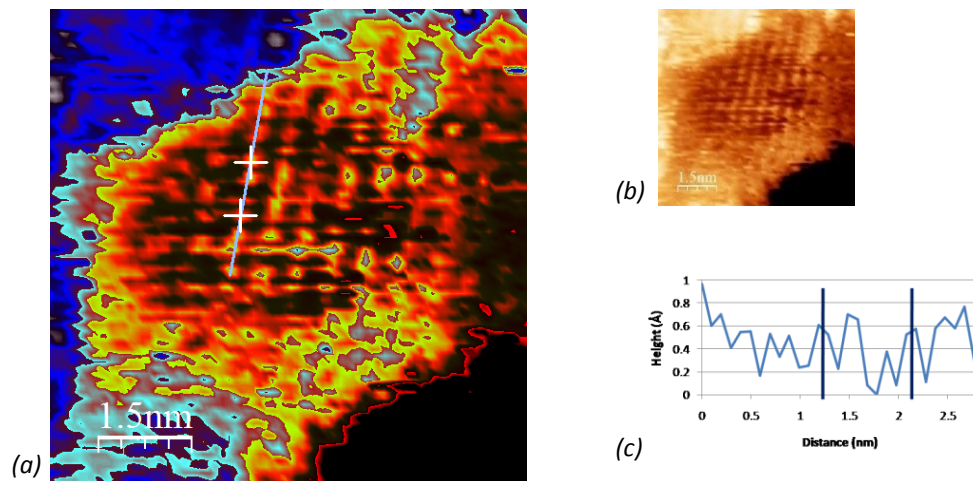


Figure 3.11 High magnification STM image with high contrast (a) displaying measured atomic spacing on a particle, original image (b) and line profile of height (c). {Images – V = 0.74 V, I = 1.23 nA}

The corrugated domains are much clearer and increasingly well ordered after annealing to 650 K. *Figure 3.12* demonstrates that the corrugation and Moiré pattern are convoluted together by revealing elements of the Moiré pattern within individual domains of corrugation. The ridges of the

corrugation have an average spacing of 5.22 Å as measured from the image in *figure 3.12b*. The larger scale morphology remains mostly unchanged from 550 K with island size remaining around 20-25 nm on average.

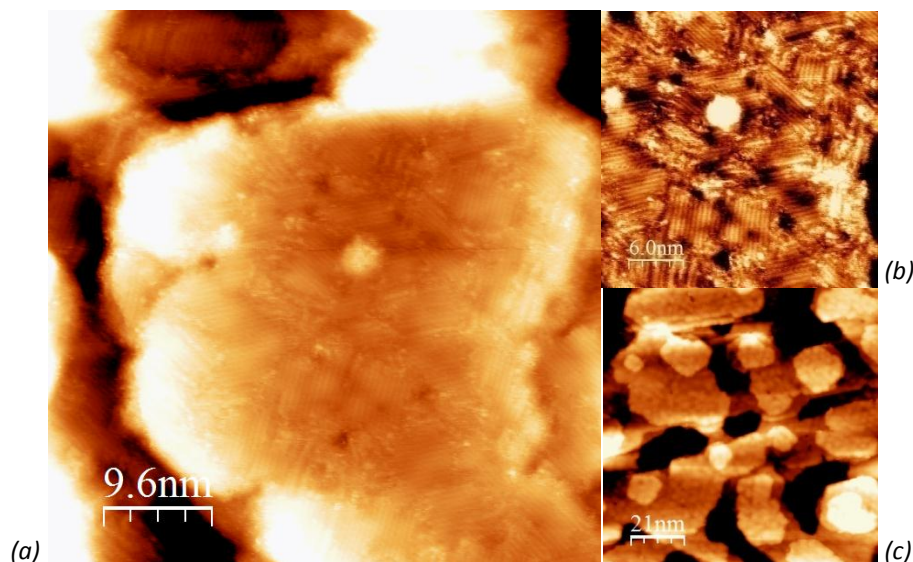


Figure 3.12 STM images at 650 K including enlargement of the top of a particle (a) {48 x 48 nm², V = -0.51 V, I = 1.18 nA} further enlarged high contrast image (b) {V = -0.51 V, I = 1.18 nA} indicating surface reconstruction and wider view showing the changes in the surface morphology (c) {120 x 120 nm², V = -0.055 V, I = 0.63 nA}.

As the annealing temperature increases into the upper temperature range the surface morphology changes to give a stepped appearance, displayed in *figures 3.13 and 3.14*. Above 750 K the island morphology fully dissipates leaving moderately stepped terraces. These terraces still incorporate a Moiré pattern, but the dimensions increase gradually from a mean distance of 3.34 nm (averaged for 550, 600 and 650 K Moiré pattern measurements) to 4.0 nm at 700 K and 9.5 nm at 750 K.

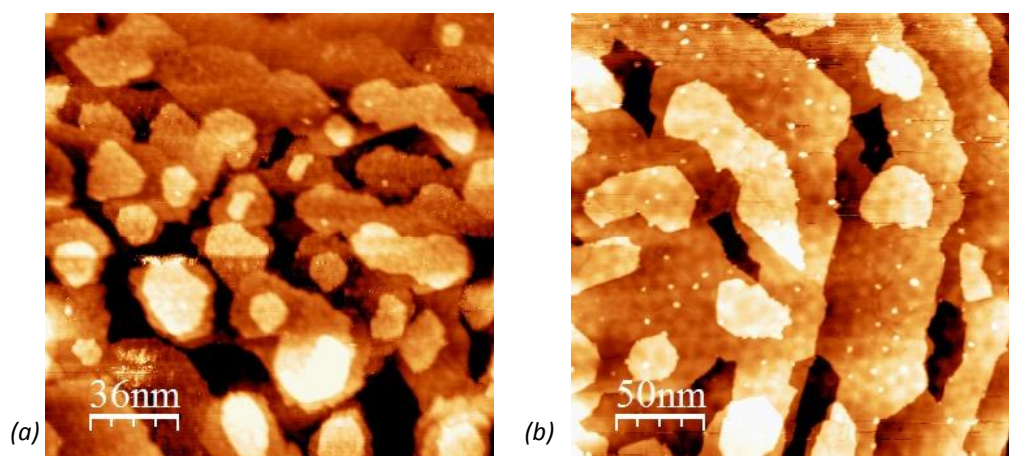


Figure 3.13:- STM images at 700 K (a) {180 x 180 nm², V = -0.5 V, I = 1 nA} and 750 K (b) {250 x 250 nm², V = 0.42 V, I = 1.39 nA} demonstrating the changes in morphology at high temperatures.

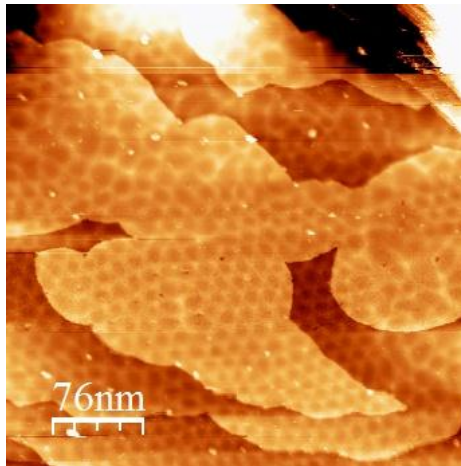


Figure 3.14:- STM image at 800 K displaying the terrace morphology { $380 \times 380 \text{ nm}^2$, $V = -1.37$, $I = 1.07 \text{ nA}$ }.

The images of the surface after annealing to 800 K (figure 3.14) demonstrate an expansion of the terraces and a change in the Moiré pattern dimensions – from 9.5 nm at 750 K to 14.46 nm at 800 K. The general appearance of the surface after annealing to this temperature is well ordered with terraces extending for several hundred nanometres. The steps on this surface are also well ordered, exhibiting a smooth appearance.

3.4 Discussion

Low Temperature Regime (300 – 500 K)

The STM images taken during the cobalt growth are in strong agreement with the data reported by Wasniowska *et al* [7-9]. These data differ in the cobalt quantities deposited and the deposition method. In contrast to the 4 ML deposited from the thermal doser in these experiments, Wasniowska *et al* examine 0.6, 2.3, 3 and 10 ML deposited using an E-beam doser – dosing rates used are comparable (0.2 ML min^{-1} compared with *ca.* 0.4 ML min^{-1} [7], respectively). The comparatively rough appearance of the islands in these data is attributed to decreased kinetic control due to higher cobalt deposition rate. The measurement of the dislocation patterns seen in the low coverage image corresponds most closely to a unit cell of ten palladium atomic spacings (calculated theoretically as 2.75 nm) and eleven cobalt spacings.

From immediate qualitative inspection of the 1 layer ion intensity plot at room temperature (and the lower annealing temperatures) it is concluded that the growth is not pseudomorphic. The presence of the palladium peak at 90 keV (with a sub-surface profile) indicates that the cobalt surface layers as being out of alignment with the bulk lattice, therefore not blocking the palladium. The small feature on the high energy side of this peak (at 91.5 keV) confirms that a small amount of palladium is not covered with cobalt.

The low yield in scattering ion intensity versus scattering angle data of the surface palladium after deposition and the lack of blocking features is consistent with Pd being covered by the Co film. The sub-surface data with a relatively high absolute yield and corresponding large blocking features is characteristic of a non-pseudomorphic overlayer. Although the cobalt is not pseudomorphic, the cobalt scattered ion intensity versus scattering angle spectra contain discernible blocking features and is therefore quite well ordered. The similarity of the blocking feature positions to those of the palladium bulk indicate that the growth proceeds along the same stacking vectors as the crystal.

The STM data of the low annealing temperatures (up to 500 K) depict few changes in the macroscopic structure. In the MEIS experiments, the 1 layer scattered ion intensity versus energy MEIS data also exhibit few changes in the intensity versus energy profiles in agreement with the STM data. There are, however, notable differences that can't be seen in the STM images. The small surface palladium feature at 91.5 keV disappears with increasing annealing temperature and the main peak, *ca.* 90 keV, becomes increasingly narrow. These observations indicate that the cobalt overlayer becomes increasingly homogeneous in thickness and fully wets the Pd surface.

Across these temperatures the structure of the sub-surface region remains constant, depicted in the scattered ion intensity versus angle plots (*figure 3.4a*). As the surface Pd composition drops due to wetting by the Co film, there is a loss of intensity in the Pd surface signal across the whole angular range as expected (*figure 3.3*).

Middle Temperature Regime (500 – 700 K)

Between 500 K and 700 K the most complex behaviour is observed. At these temperatures a cobalt palladium alloy is formed as indicated in *figure 3.15*. The dislocation pattern in these islands disappears, replaced by a Moiré pattern which may be explained by a reduction in strain as the lattice parameter of the alloy becomes more Pd-like than was the case in the pure Co overlayer. The appearance of the surface clearly changes from rough islands to an intermediate with characteristics that are both island like and terrace like.

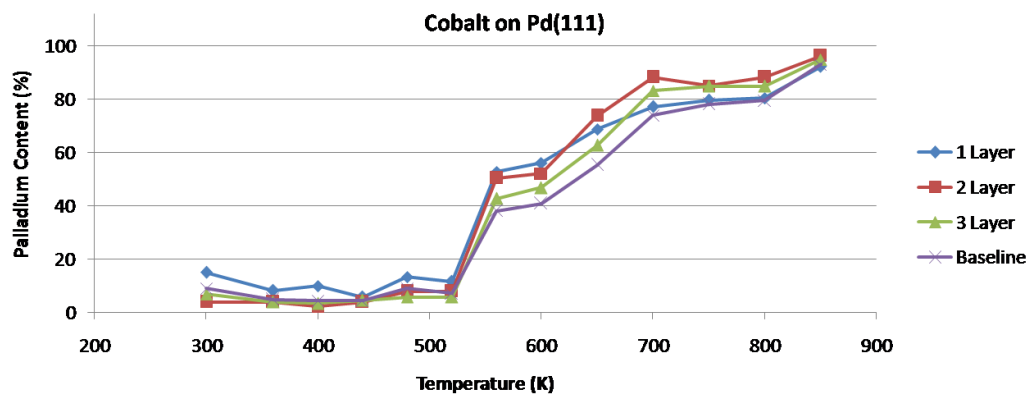


Figure 3.15:- Composition graph indicating the percentage of palladium after each annealing temperature relative to the clean Pd{111} data. Each data series corresponds to the yield from the main blocking channels as well as the estimated absolute yield.

Qualitatively, each of the scattered ion intensity versus energy plots remain essentially constant until 560 K (*figure 3.15*). While the surface palladium peak begins to appear in the scattered ion intensity versus energy, the relative peak intensity also remains constant. The I vs. E spectra change at 560 K to feature a convoluted double palladium peak, associated with the corresponding I vs. θ changes. The peaks are almost unchanged in the 600 K spectra indicating a stable alloy composition formed at these temperatures. Measurement of the yields at the bottom of the blocking channels quantitatively confirms this, giving an initial figure of 45% palladium in the 2 and 3 layer geometries and 55% in the 1 layer geometry (as a fraction of the visible palladium in the clean surface – presented in *figure 3.15*).

The intensity decreases in the cobalt across these temperatures occur in a more linear fashion. As the technique is less sensitive to cobalt this probably partly explains why the changes appear to be less abrupt. The structure of the cobalt I vs. θ spectra does coincide more convincingly with the palladium spectra. The spectra at 560 and 600 K clearly stand apart in shape from the spectra at lower and higher annealing temperatures.

The corrugated structures seen in the STM images after annealing to 600 and 650 K can be attributed to a (2×1) structure which consists of alternating rows of palladium and rows of cobalt. The composition of such a structure in the top layer is 50% Palladium which closely agrees with the MEIS data. The (2×2) LEED pattern that was observed during the experiments (*figure 3.16*) can consequently be concluded to be the result of the three rotated domains of (2×1) convoluting together to give an apparent (2×2) – as detailed below in *figure 3.16*.

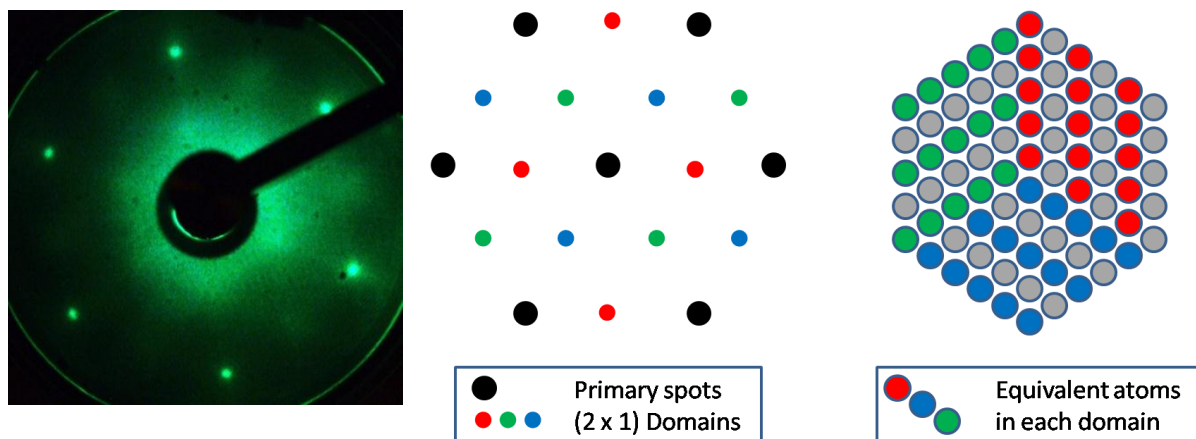


Figure 3.16:- Colour enhanced LEED pattern, Illustrative schematic of the (2×2) pattern formed from the convolution (2×1) domains aligned along three different vectors as well as a model of the corresponding surface domains.

Annealing from 650 to 700 K the spectra then change again as the cobalt begins to diffuse into the palladium bulk. The structure of the cobalt and sub-surface palladium I vs. θ diminishes along with a decreasing absolute yield whilst the blocking features get stronger in the palladium surface spectra, and the absolute yield becomes closed to the yield seen for clean palladium.

High Temperature Regime (Above 700 K)

Above 700 K the majority of the cobalt is dissolved into the palladium bulk. A small quantity remains causing continued, but diminishing disruption at the surface in the form of a Moiré pattern. As the annealing temperature gets higher, the unit cell of the Moiré pattern expands due to the increasingly palladium rich surface composition. At 800 K the STM images show the surface to be

entirely made up of terraces and steps. The Moiré pattern arises from the lattice mismatch between the alloy and the underlying substrate. Assuming a linear variation in the lattice spacing as the composition becomes increasingly palladium rich, the composition can be estimated from the average lattice spacing. The Moiré pattern in the images after annealing to 800 K have a periodicity of 14.5 nm (corresponding to 51 Pd-Pd spacings – defined as 2.75 Å), giving an average lattice spacing of 2.7 Å. This corresponds to an expected 80% palladium in the surface alloy, assuming close packing is retained.

At 700 K, the blocking features and yields of the structural MEIS data are close to those expected for a clean palladium sample. As the sample is annealed further the sub-surface feature fully diminishes and the surface peak blocking channels become increasingly well defined. The cobalt peak continues to drop in intensity until 850 K when there is no trace of cobalt in the MEIS spectrum. The cobalt I vs. θ data at these temperatures show lower yields and associated reduction in blocking feature intensity. However the spectra at this point are not quantifiable because a small error in the background subtraction of the palladium bulk would be easily mistaken as cobalt information. The cobalt atoms at the higher temperatures can be assumed with confidence to be fully integrated into the palladium lattice and therefore the cobalt data should show fcc characteristic blocking features.

It is important to consider that the experiments are carried out in two different systems at different times. The main concern is accurately correlating the thermocouple measurements in each system. There is a confirmed discrepancy where the STM thermocouple indicated the crystal temperature gave a reading higher than the actual surface temperature. In the MEIS system the thermocouple readings were confirmed using a pyrometer providing a higher confidence in the measured temperature. This problem was considered while comparing all STM images with MEIS data, and the separation of the results into different regimes of several hundred degrees largely negates this issue.

VEGAS Simulation of the Growth of Cobalt on Pd{111}

The cobalt has been described as growing in a non-pseudomorphic manner, but with the same structure as palladium. As discussed this agrees well with previous studies on the growth of cobalt at room temperature [7-9], and also fits with the appearance of the dislocation pattern. An unstrained lattice of cobalt (without dislocation lines) would consist of 11 Co atoms to every 10 Pd atoms due to the lattice mismatch. This provides a starting point to focus the VEGAS simulations on.

A number of VEGAS simulations were carried out to identify the growth mode of cobalt on Pd{111}. The presence of blocking channels in the cobalt data that correspond to the substrate blocking features immediately discount hcp or rotated fcc growth modes. Simulation of the fcc N growth mode was in good agreement with the blocking channels at 84° and 109°, the absolute yield was underestimated. By factoring in disorder (assuming an amorphous fraction of the surface) in the simulated cobalt layers a close match to the experimental yield was obtained (presented in *figure 3.17*). This simulation also includes a 10 pm contraction in the cobalt layers compared to the bulk spacing in fcc Co{111}, which was included to ‘tune’ the position of the blocking channels to match the experimental spectrum. A clear problem with the fcc N cobalt simulation is that it does not account for the peak at 97-98 keV in the experimental data.

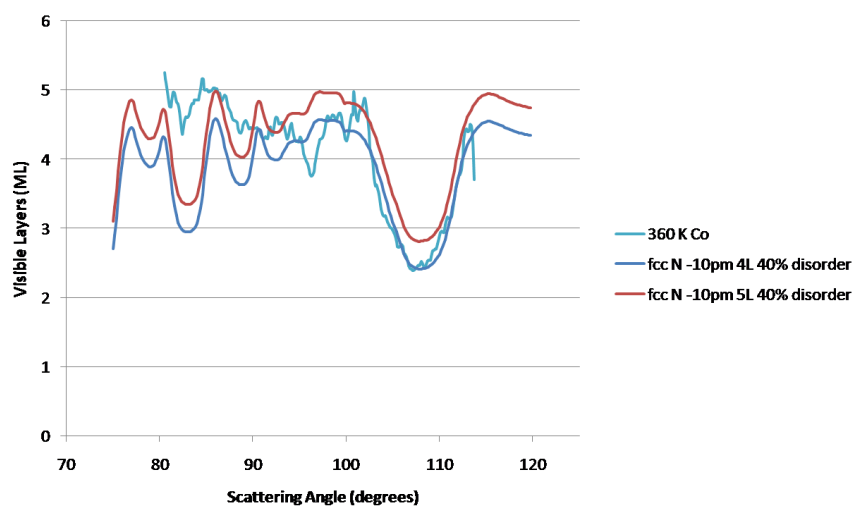


Figure 3.17:- Visible layers of cobalt versus scattering angle spectra after annealing to 360 K along with VEGAS simulations of fcc N growth with 40% disorder and 10 pm relaxation.

A blocking feature in the region of the 98° feature can be simulated by introducing a stacking fault into the cobalt structure. The stacking faults that are represented schematically in *figure 3.18* correspond to a change in the growth mode at a given film thickness. This type of structural change has been suggested in similar studies of cobalt on Pd{111} [7], and would not be unexpected, considering the phase behaviour of pure cobalt. The stacking fault with the notation; CBCABC, was found to provide a suitable match to the additional blocking feature. Modification of the model to include different Moiré pattern periodicities was carried out in order to attain a closer fit to the data. The simulated spectra along with the 360 K experimental data are shown in *figure 3.19*. With so many simulation parameters, R-factor analysis to optimise the fit would be impractical, however the simulations can be used qualitatively to conclude that there is a stacking fault in the cobalt structure when grown on Pd{111}, but the structural parameters cannot be conclusively identified.

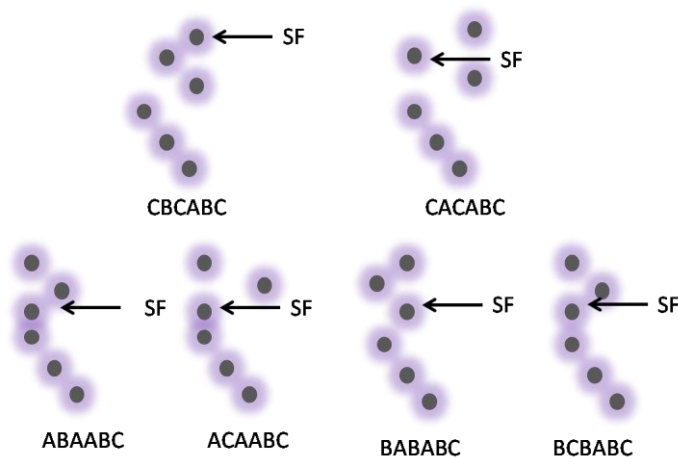


Figure 3.18:- Schematic diagram of the six possible stacking faults in the overlayer simulated using VEGAS.

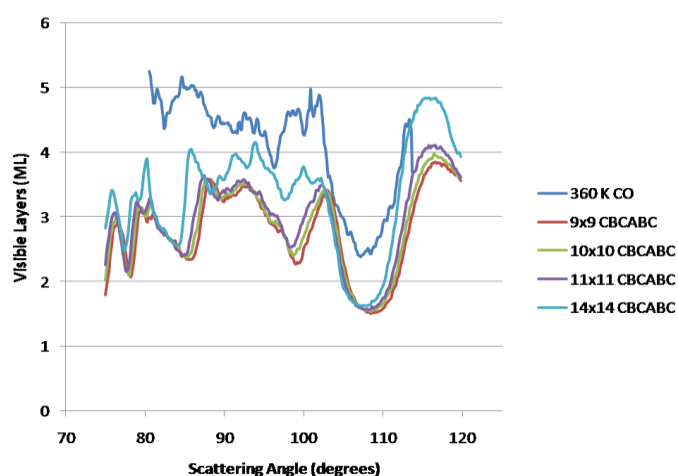


Figure 3.19:- Visible layers of cobalt versus scattering angle spectra after annealing to 360 K along with VEGAS simulations of fcc N growth containing a stacking fault. The simulations include a range of cobalt lattice sizes.

VEGAS Simulation of the CoPd Alloy on Pd{111}

Across the annealing temperature range of 550-700 K, the formation of a well-defined surface alloy (concluded as possessing a $p(2 \times 1)$ unit cell based on the {111} plane of a bulk CoPd alloy) is observed. Analysis of the palladium polygon data relative to the clean surface suggest that the alloy has a constant composition across the top three layers, however the extent of this alloy beyond this depth is not clear, nor is it clear whether the alloy sits on pure Pd{111} or on a thin cobalt film.

The aim of the VEGAS simulations for this annealing temperature regime is to address these unknowns. Two structures were tested for comparison with the experimental spectra: The first comprised of 9 ML of 50-50 CoPd alloy and the other consisting of 3 ML of 50-50 CoPd alloy on 3 ML of pure cobalt grown on Pd{111}. The total cobalt in each case corresponds to 4.5 MLE of cobalt

which relates to the initial cobalt coverage after deposition. The simulations in each case comprise of three equivalent structures (with unit cell of 12 x 12 Pd atoms, and 13 x 13 'alloy' atoms) with the scattering plane rotated by 120° to account for the three different rotational domains – the VEGAS outputs are averaged together to provide the final result. At the intermediate temperatures the surface exhibits a Moiré pattern with larger dimensions than the dislocation pattern (3.45 nm). These simulations along with the experimental data at 560 K are presented in *figure 3.20*.

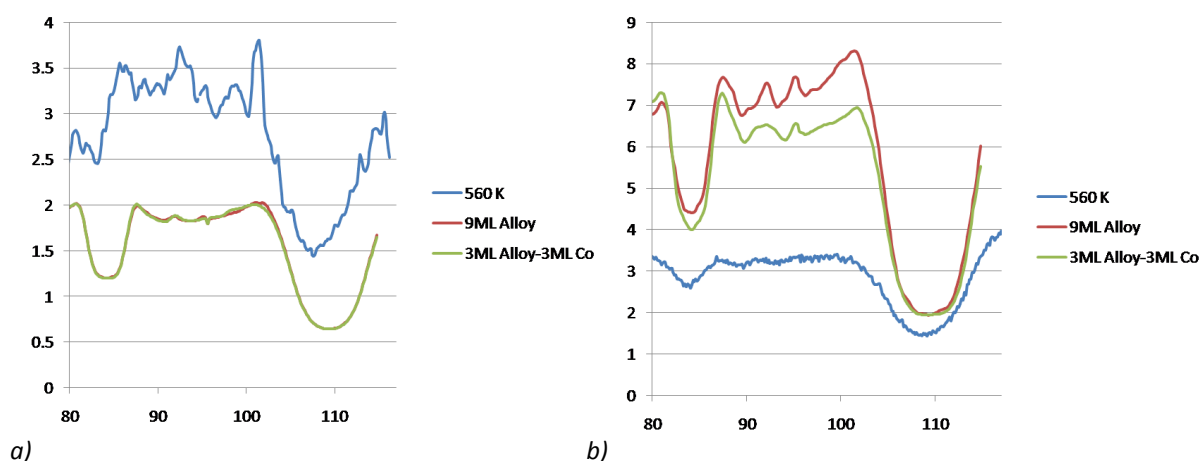


Figure 3.20:- VEGAS simulations of scattered ion intensity versus scattering angle corresponding to the Co experimental data (a) and the Pd data (b). The simulated lattice consists of 6 ML of 14 x 14 overlayer atoms to 13 x 13 palladium atoms. Figures also include the experimental data for the 560 K anneal – analysed using the IGOR programme.

The simulated data in each case, is in close agreement with the blocking channel positions of the experimental I vs. θ spectra, but not the absolute yields. It appears that the simulations overestimate the palladium visibility and underestimate the cobalt visibility. On close scrutiny of the VEGAS outputs the mismatch may be explained by the inadequacies of the VEGAS simulation itself. VEGAS was designed with well-defined crystalline structures in mind – VEGAS is expected to overestimate certain ion focusing effects known to occur [12] at skimming geometries that are extremely close, but not completely aligned with the atomic lattice directions. With the beam aligned with respect to the underlying Pd{111} substrate the slightly misaligned geometry occurs in the alloy due to the smaller layer spacings. The contribution from these focusing effects was examined and the contribution from the top three layers of the Pd bulk was found to be 2 ML for each layer, confirming a large overestimation. The explanation for the cobalt underestimation is based on the atomic disorder for cobalt (as discussed for the simulations of Co growth at 300 K). Further work to establish the depth dependent composition, but on the basis of the MEIS analysis it is likely that the composition is uniform in top three layers at least.

3.5 Conclusions

The growth and alloying behaviour through sequential annealing of cobalt on palladium {111} is examined. The deposition of cobalt (in close agreement with the literature) gives rise to nucleation of cobalt in both fcc and hcp surface sites. The growth of islands continues from these nucleation sites along the crystal directions in a non-pseudomorphic way resulting in the appearance of dislocation lines to release the strain in the lattice. After further deposition to form multiple layers the cobalt assumes an fcc structure with layer growth continuing along the same direction as the substrate.

Annealing of cobalt gives rise to three separately defined regimes which are defined by their surface morphology. Annealing up to 500 K is associated with a cobalt rich surface dominated by the continuing island-type morphology. Although the island appearance is constant across these temperatures, the small proportion of visible surface palladium seen after deposition disappears.

Between 500 and 700 K the majority of the surface thin film consists of stable cobalt palladium alloys. These alloys exhibit a corrugated arrangement of atoms and include a Moiré pattern with a unit cell dimension of 3.45 nm, corresponding approximately to 14 atoms of cobalt on 13 atoms of palladium.

Cobalt fully integrates into the palladium lattice beyond 700 K, thus resulting in a palladium rich surface. The cobalt in the surface alloy gives rise to Moiré patterns, the unit cell of which increases as the cobalt concentration drops. At these annealing temperatures the appearance of the surface is that of large terraces as the islands are dissolved into the substrate.



3.6 Bibliography

- [1] Owen E. A. *et al*, *Effect of Grain Size on the Crystal Structure of Cobalt*, Proc. Phys. Soc. (1954), 456-466
- [2] Bidwell L. R. *et al*, *The thermodynamic properties of cobalt-palladium solid solutions*, Acta Metallurgica 18 (1970), 1013-1019
- [3] Lee B. W. *et al*, *Surface structures of the two allotropic phases of cobalt*, Phys. Rev. B 17-4 (1978), 1510-1520
- [4] Rao C. N. and Rao K. K., Can. J. Phys. 42 (1964), 1336
- [5] Betteridge W., *The properties of metallic cobalt*, Prog. Mater. Sci. 24 (1980), 51-142
- [6] Howe C. J. *et al*, *Ultra-thin films and surface alloying of Pd on Cu(111) investigated by medium energy ion scattering*, Surf. Sci. 604 (2010), 201-209
- [7] Wasniowska M. *et al*, *Growth and morphology of cobalt thin films on Pd(111)*, Surf. Sci. 601 (2007), 3073-3081
- [8] Przybylski M. *et al*, *Topology-dependent interface contribution to magneto-optical response from ultrathin cobalt films grown on the (001), (110), and (111) surfaces of Pd*, Phys. Rev. B 73 (2006), 085413, 1-9
- [9] Wasniowska M. *et al*, *Submonolayer regime of Co epitaxy on Pd(111): Morphology and electronic structure*, Phys. Rev. B 78 (2008), 035405
- [10] Miyawaki J. *et al*, *Structural study of Co/Pd(111) and CO/Co/Pd(111) by surface X-ray absorption fine structure spectroscopy*, Surf. Sci. 601 (2007), 95-103
- [11] Boukari S. *et al*, *Strain induced epitaxial relationships of Cr on Co/Pd(111)*, Surf. Sci. 430 (1999), 37-44
- [12] Tromp R. M., *Practical Surface Science (Second Edition) Volume 2: Ion and Neutral Spectroscopy*, (1992) John Wiley & Sons Ltd

*Structure and Composition of Cobalt
Oxide Thin Films and Oxidised
CoPd Alloys on Pd{111}*

4.1 Introduction

In *Chapter 3*, the structure and composition of cobalt palladium alloys on a Pd{111} substrate are characterised under UHV conditions. In this chapter, MEIS is used to examine the thermal behaviour of a pre-formed cobalt oxide film on Pd{111} and the influence of oxygen adsorption on bimetallic CoPd surfaces of various compositions. As discussed in *Chapter 1*, the oxidation of the FTS catalyst is an important consideration, and the purpose of the experiments in this chapter is to gain an understanding of the influence of the noble metal present.

During catalyst preparation the thermal decomposition of the cobalt precursor gives rise to an inactive cobalt oxide, which is then reduced to the active metal. From the commonly used cobalt nitrate [1], Co_3O_4 is formed which is then reduced *via* CoO leaving the cobalt metal. In addition to these two oxides, Co_2O_3 can also exist [2] although this compound is rare and difficult to synthesise. The stoichiometry of the cobalt oxide synthesised from metal vapour deposition in an oxygen atmosphere may be one of these phases or a mixture of different phases.

Cobalt oxide has been deposited in UHV conditions on Ag(001) [3] and on Pd(100) [4]. The cobalt oxide on silver [3] was determined to be CoO using LEED-I(V) and comparing the experimental data with theoretical I(V) plots. Although the CoO exhibited the expected rocksalt structure, the layer distances were shown to be slightly expanded in comparison to bulk CoO. The thermal evaporation of cobalt was carried out using a K-cell at a rate of 0.2 ML min^{-1} in an oxygen environment of 10^{-6} mbar.

The analysis of cobalt oxide growth on Pd(100), as examined [4] using STM, Photoemission Spectroscopy (PES) and X-ray Absorption Spectroscopy (XAS), also indicated formation of CoO at a similar film thickness. In addition to this coverage, 10 and 20 ML of the oxide were also deposited on Pd(100) and the data from the PES showed that the oxide exhibits a Co_3O_4 stoichiometry at coverages higher than 10 ML.

The overall view of cobalt oxide stoichiometry is that the two oxidation states of cobalt compete thermodynamically and that reduction/oxidation easily occurs at the surface [5] resulting in either CoO or Co_3O_4 depending on the conditions of the system. Although the structures are readily interchangeable, either one may be locked by defects on the surface.

The experiments in *Chapter 3* were carried out in UHV, an inert environment in which the sample is subject to the minimum external influence. In most catalytic systems the catalyst surface is exposed to a complex mixture of compounds and reactive intermediates – some strongly influencing the active surface or the support. Also the pressure and temperature of this complex mixture – chosen to give favourable reaction thermodynamics and kinetics – changes the influence of each individual species on the surface.

The behaviour of cobalt in the presence of an oxidising agent has been previously shown to be relevant in FTS conditions. Although molecular oxygen is not considered to be present under such high partial pressures of hydrogen, it remains important in representing oxidation processes known to occur in FTS conditions [6].

Oxidation of cobalt is facile at room temperature [7] and occurs down to 120 K [8] through dissociative adsorption followed by absorption into the bulk – occurring increasingly rapid as the temperature is increased. Above approximately 1000 K the absorption is essentially immediate; associated with no discrete chemisorbed phase. In these examples the substrate used is Co(0001) and the oxygen is absorbed into the bulk as defects. A thin layer of around 4 ML of cobalt would become quickly saturated above 10^{-6} mbar of oxygen, even at room temperature.

On palladium, oxygen also adsorbs dissociatively [9, 10], although in contrast to cobalt the rate of absorption into the bulk is relatively slow. The slow absorption rate may be accredited to a build up of oxygen in the near surface. The adsorbed oxygen that remains at the surface is easily removed in the presence of carbon monoxide [9]. The oxygen adatoms on the Pd(111) surface sit in threefold hollow sites with a $c(2 \times 2)$ unit cell.

Oxygen adsorption has previously been studied on two polycrystalline $\text{Co}_{50}\text{Pd}_{50}$ [11] and $\text{Co}_{37}\text{Pd}_{63}$ [12] alloys (mol. %). TPD was used in this case to examine the surface using oxygen as a probe [11] as well as N_2O and CO [12]. As in the examples of the individual metals, the oxygen adsorption is dissociative in nature, but in place of diffusion into the bulk, the cobalt is segregated to the surface and a cobalt oxide overlayer is formed. The oxide formation is associated with a drop in N_2O adsorption. In this study the authors referred to oxygen segregation on $\text{Pt}_3\text{Co}(110)$ [13] where both typical cobalt oxide structures are detected, but the stoichiometry could not be determined from the TPD or AES for the cobalt palladium system.



Cobalt oxide films on Pd{111} were examined using XPS and magneto-optical Kerr effect spectroscopy by Kim *et al* [14]. The oxide is found to exist mainly as CoO, although small amounts of Co₃O₄ were also detected. Annealing to temperatures beyond 700 K caused the Co₃O₄ to decompose into CoO. The oxide is also concluded to be without ferromagnetic properties, unlike metallic cobalt.

The importance of structure and the reduction of the catalyst in FTS have been considered. This chapter will investigate thin films of cobalt oxide formed from cobalt deposition in an oxygen atmosphere and will examine the effect of oxygen on several cobalt palladium alloy compositions across a range of oxygen pressures.

4.2 Experimental

Cobalt Oxide on Pd{111} – Medium Energy Ion Scattering

The fcc Pd{111} crystal substrate [Surface Preparation Laboratories] used in all experiments, was cleaned using cycles of Ar⁺ sputtering (1.5 keV, 10-20 μ A crystal current) followed by annealing to 1100 K. The condition of the surface was considered to be clean when a clear (1x1) LEED pattern could be seen, combined with either an AES spectrum presenting no impurities (MEIS apparatus), or an STM image indicating a clean surface with large terraces (STM apparatus).

To prepare thin films of cobalt oxide, 4 ML of cobalt was deposited using an approximate dosing rate of 0.04 ML min⁻¹ thermally evaporated from a cobalt filament as described in *Chapter 2*. Cobalt was dosed in a background oxygen atmosphere of 2×10^{-7} mbar. The correct dose was achieved in the STM apparatus by taking images of the surface after 5 minutes dosing, assessing the coverage and multiplying up to give the remaining dose time for 4 ML. In the MEIS apparatus coverage was calculated from the attenuation of the Pd 330 eV Auger signal and confirmed using MEIS. This initial coverage is sufficient to create a continuous cobalt overlayer and provide a high signal to noise ratio in the MEIS data.

STM and MEIS data were collected for the prepared surfaces and for consecutive annealing every 100 K (for five minutes) until 1100 K. In between annealing the crystal was allowed to cool to room temperature before transfer and data collection. In addition LEED patterns and AES spectra were monitored after each annealing temperature.

Oxygen Adsorption on CoPd alloys on Pd{111}

For the oxygen segregation experiments, the alloy was first prepared in accordance with the experiments in *Chapter 3*. Approximately 4 ML of cobalt (estimated with MEIS) were deposited onto Pd(111) and then annealed for 5 minutes to one of the selected temperatures – 560, 600 and 700 K – chosen to give surface compositions ranging from cobalt rich to palladium rich. For reference, data were collected for the prepared samples before exposure to oxygen. In addition these preparation temperatures correspond to earlier TPD/AES surface analysis of the binary bulk alloy [11, 12].

Oxygen was dosed in the preparation chamber at progressively increasing pressures, specifically 10^{-7} , 10^{-6} , 10^{-5} and 10^{-4} mbar, transferring and collecting MEIS data in between. The

oxygen dose was kept constant for each pressure, maintaining 1000 L of oxygen in each case by altering the dose time –the basis of this is discussed in *Section 2.2*.

During all MEIS data collection, the crystal was in an aligned geometry along the [-1-12] azimuth with the beam incident along the [-1-1-4] direction which corresponds to an illumination of the top three layers of an ideal fcc {111} surface. The detector was aligned to two different scattering angle ranges centred at 86° and 106° – the subsequent data make up the blocking channels in 1-layer, 2-layer and 3-layer geometries of the ideal surface.

4.3 Results

Cobalt Oxide on Pd{111} – Medium Energy Ion Scattering

The MEIS intensity versus energy spectra cut through the 1-layer blocking channel, seen in *figure 4.1*, remain very similar from room temperature up to 700 K. The palladium manifests as a sub-surface peak with a double cobalt feature consisting of a peak at 85 keV and a broad symmetrical feature centred at 83 keV. The feature at 83 keV slowly decreases in intensity as the annealing temperature increases. In addition, the high energy edge of the palladium peak at 89-91 keV includes minor shifts up in energy from 400 to 700 K. At 800 K the peak at 90 keV changes, shifting up in energy to 92.2 keV while changing profile and intensity. At this point the cobalt feature reduces to a single low intensity peak at 85 keV with a narrow surface like profile.

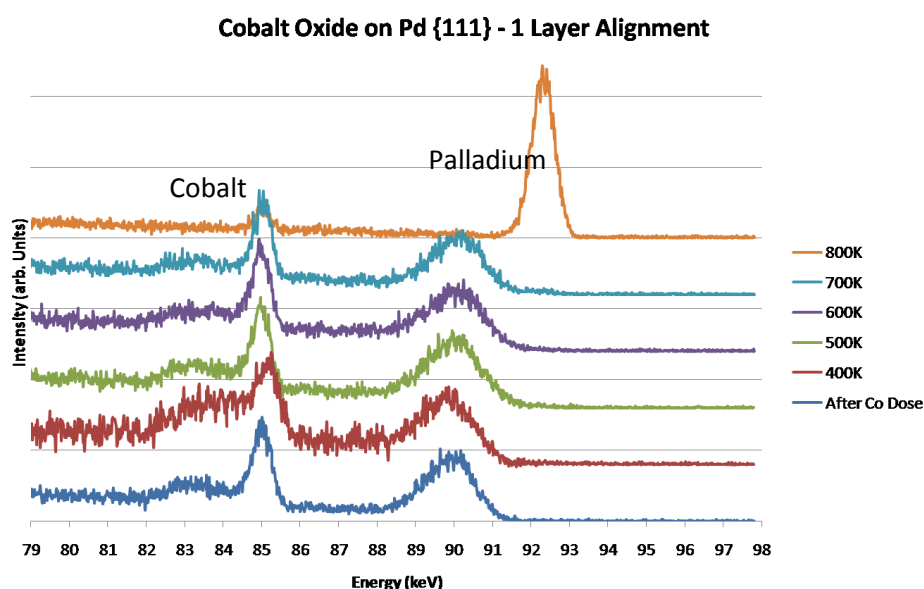


Figure 4.1:- Stacked energy versus intensity data of 4 MLE cobalt oxide on Pd{111}, sequentially annealed to increasing temperature increments.

The background of the second data set, after annealing to 400 K, was higher than the other data tiles – best explained by the beam scanning an area of sub-surface disruption to the crystal structure. To counter this, a partial background correction was applied, allowing the data to be read more clearly.

The LEED pattern for the oxide consists of six primary spots that are characteristic of the underlying fcc {111} surface. Although other features were visible, the resolution was not high enough to provide any meaningful information on the oxide layer periodicity.

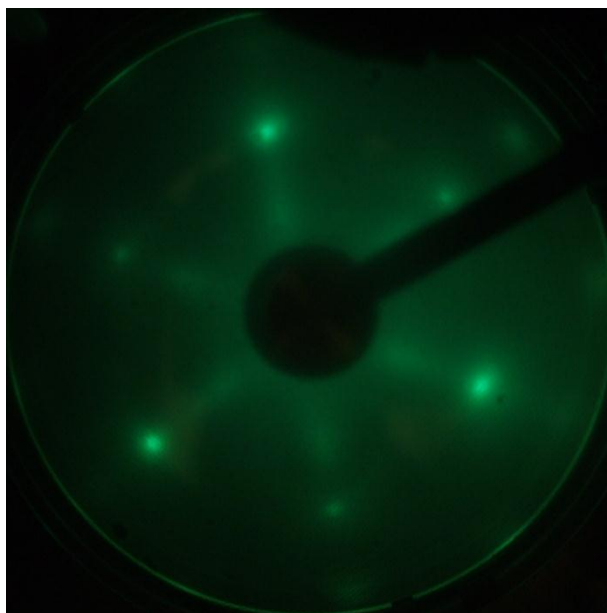


Figure 4.2:- LEED screen photograph of 4 MLE cobalt oxide on Pd{111} annealed to 700 K; indicating the 3-fold symmetry.

Cobalt Oxide on Pd{111} – Scanning Tunnelling Microscopy

0.1 MLE of cobalt oxide is deposited (300 K, 1.4×10^{-7} mbar O_2) on the palladium surface, and nucleation is observed on the terraces with a high level of dispersion (*figure 4.3a*). There are a large number of very small particles which do not aggregate at room temperature. The cobalt oxide islands are similar in appearance to the cobalt metal islands (*Chapter 3*); the greater dispersion is apparent when comparing images of similar magnification.

As the coverage is increased the high dispersion remains; as expected the particles grow as more material is deposited, but the large number of particles is still apparent. Second layer growth begins after approximately 80% of the first layer is completed, evident in *figure 4.3b*. The palladium is fully covered in the images taken at 2 MLE growth, and from there up to 4 MLE (*figure 4.3c*) while the island morphology remains outwardly consistent. At 0.8 MLE the average particle size is 6.5 Å.

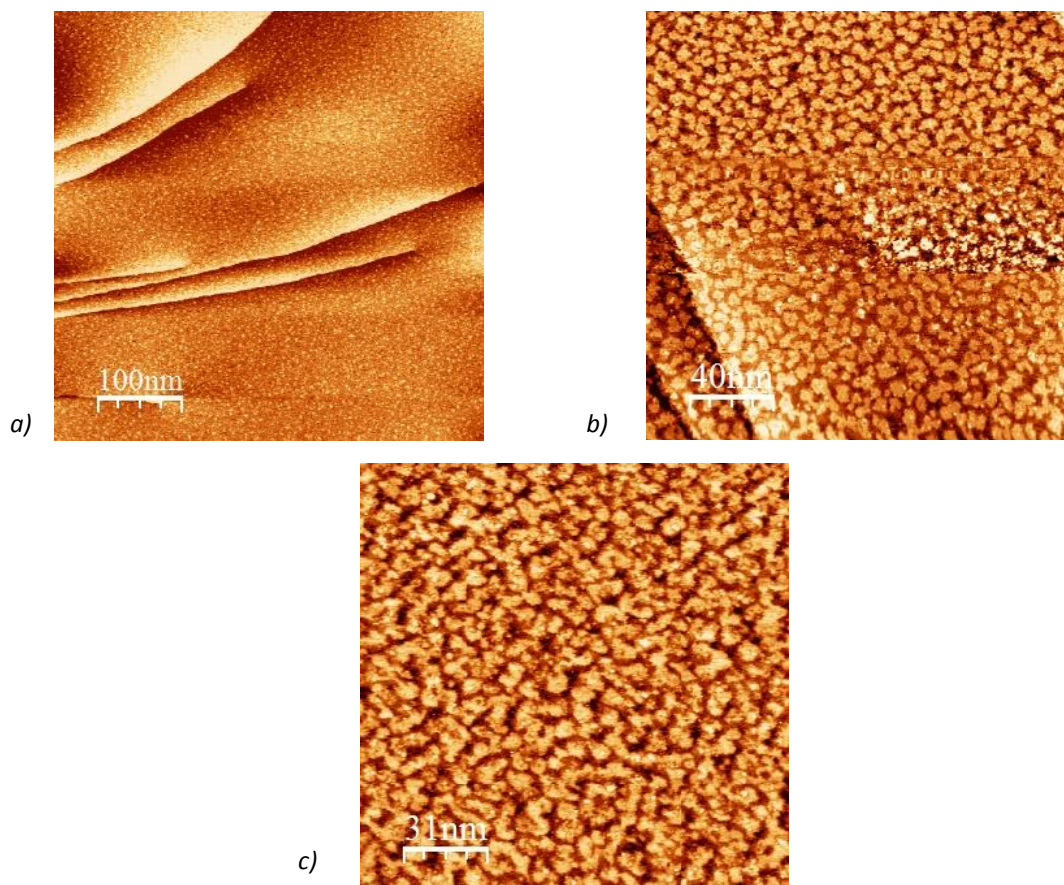


Figure 4.3:- STM images of the growth of cobalt oxide at 0.1 MLE (a) $\{500 \times 500 \text{ nm}^2, V = 0.84, I = 0.51 \text{ nA}\}$, 0.8 MLE (b) $\{200 \times 200 \text{ nm}^2, V = -1.2, I = 0.99 \text{ nA}\}$ and 4 MLE (c) $\{150 \times 150 \text{ nm}^2, V = 1.3 \text{ V}, I = 0.71 \text{ nA}\}$ coverage.

The changes in the surface after the sample is annealed to 400 K (figure 4.4) are initially small. The particles begin to amalgamate at the edges, but the overall large scale morphology remains unchanged. The surface continues to include the island like morphology with an increased number of islands joined in the uppermost layers compared with the image taken after 4 MLE dosing.

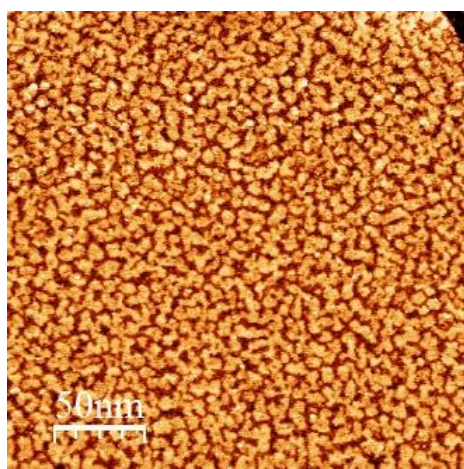


Figure 4.4:- STM image of 4 MLE cobalt oxide on Pd{111} after annealing to 400 K $\{250 \times 250 \text{ nm}^2, V = 1 \text{ V}, I = 0.68 \text{ nA}\}$

After annealing to 700 K the island morphology is replaced by a porous overlayer. The pores are one layer deep (average; 2.1 Å – consistent with a single atomic layer) with a fully continuous layer beneath. The size distribution of the pores is reasonably large and the shapes are irregular with smooth edges, however they generally do not exceed 100 nm in size and few under 10 nm. The steps in this surface are irregular comprising of buttresses and recessions; having the appearance of pores joined together, seen in *figure 4.5*.

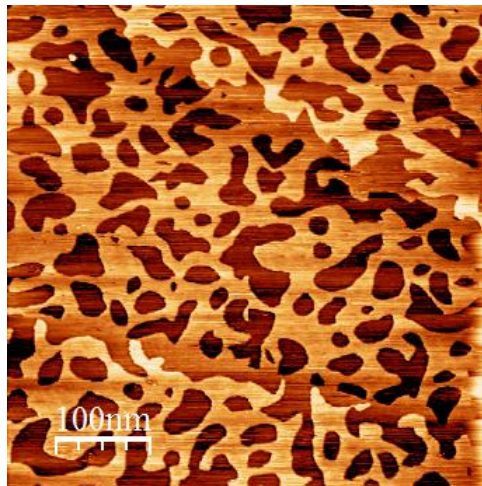


Figure 4.5:- STM image of 4MLE cobalt oxide on Pd{111} after annealing to 700 K {500 x 500 nm², V = 0.67 V, I = 1.282 nA}

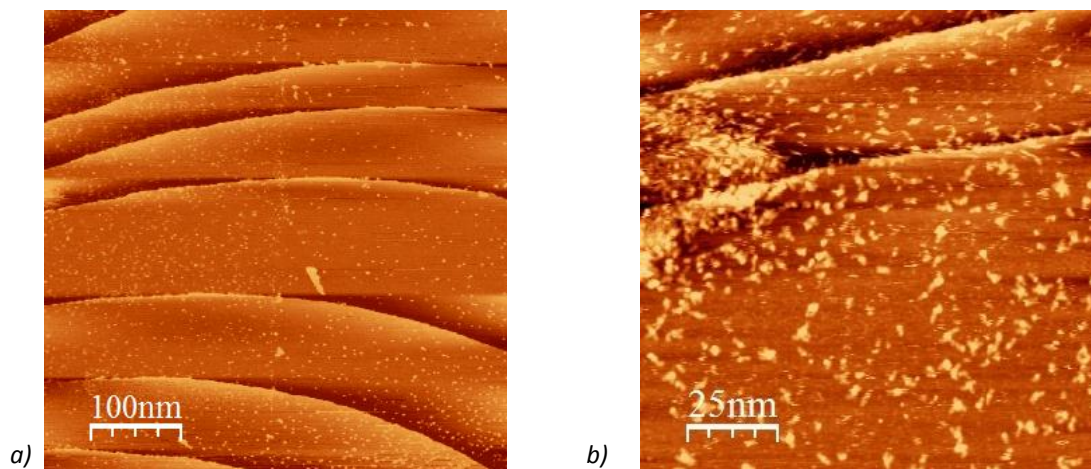
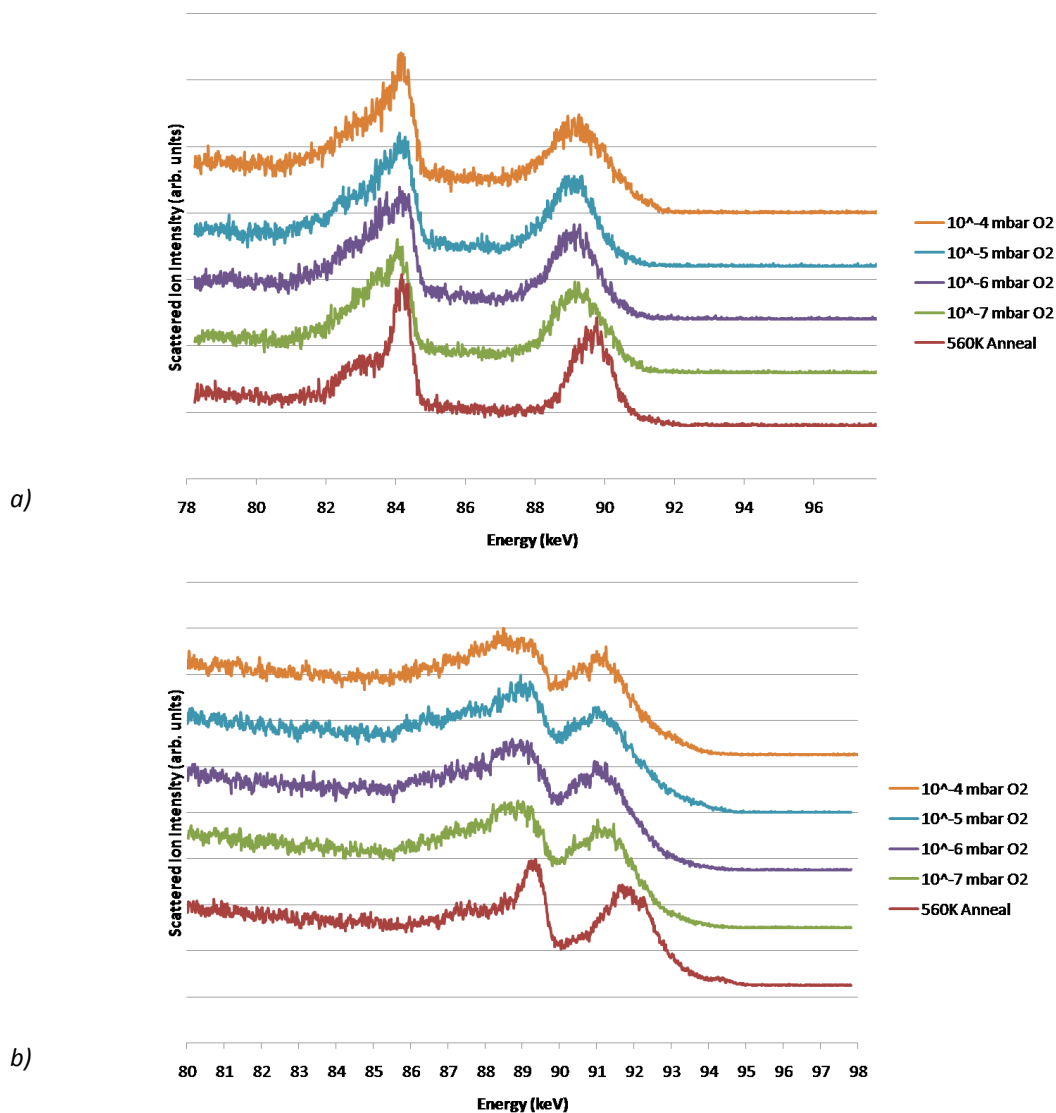


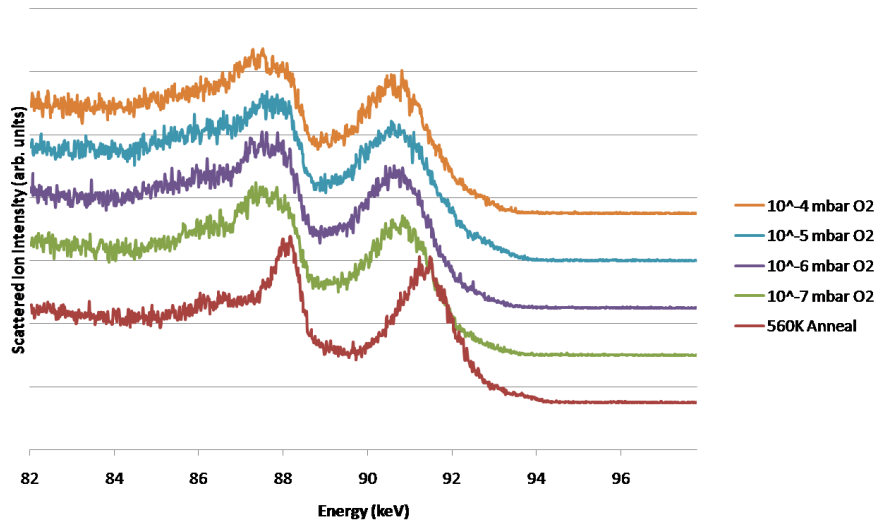
Figure 4.6:- STM images of 4MLE cobalt oxide on Pd{111} after annealing to 800 K displaying step morphology (a) {500 x 500 nm², V = 1.74 V, I = 1.159 nA} and additional defect material (b) {130 x 130 nm², V = 2.8 V, I = 0.63 nA}.

Annealing to 800 K results in the breakup of the porous structure to be replaced by a structure similar in appearance to the surface of the clean palladium crystal with minor imperfections or defect material. This surface consists of large terraces with an average step height of 2.2 Å. *Figure 4.6a* indicates the large terraces with the additional defect material visible as small specks on the terraces – increasingly evident in *figure 4.6b*.

Oxygen Adsorption on CoPd alloys on Pd{111}

Figure 4.4 presents the I vs. E MEIS spectra for oxygen exposure on a CoPd alloy surface – formed after annealing to 560 K – the composition of which (approximately 10%) corresponds to the Co-rich regime described in Chapter 3. During the first exposure at 10^{-7} mbar the large Pd peak shifts down by approximately 1 keV along with the disappearance of the very small feature at 94.3 keV. The Co peak before O_2 exposure consists of a discernible surface peak at 89.4 keV and a sub-surface shoulder of a relatively low intensity extending by more than 2.5 keV below the main peak. After the oxygen dosing the sub surface component increases in intensity while the surface component decreases, the overall result manifesting as an apparent asymmetric single feature. For all exposures including the 10^{-7} mbar O_2 the spectra are consistent, with the exception of a minor decrease at 89-90 keV corresponding to the Co surface peak component at 10^{-4} mbar O_2 .

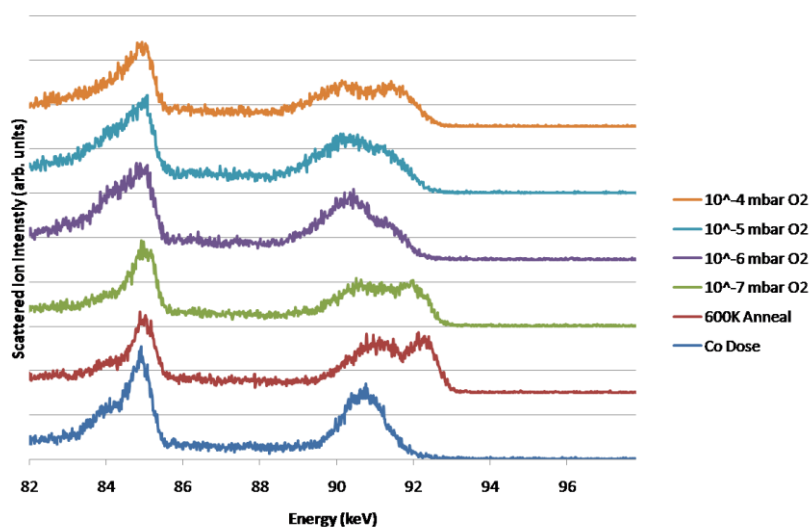




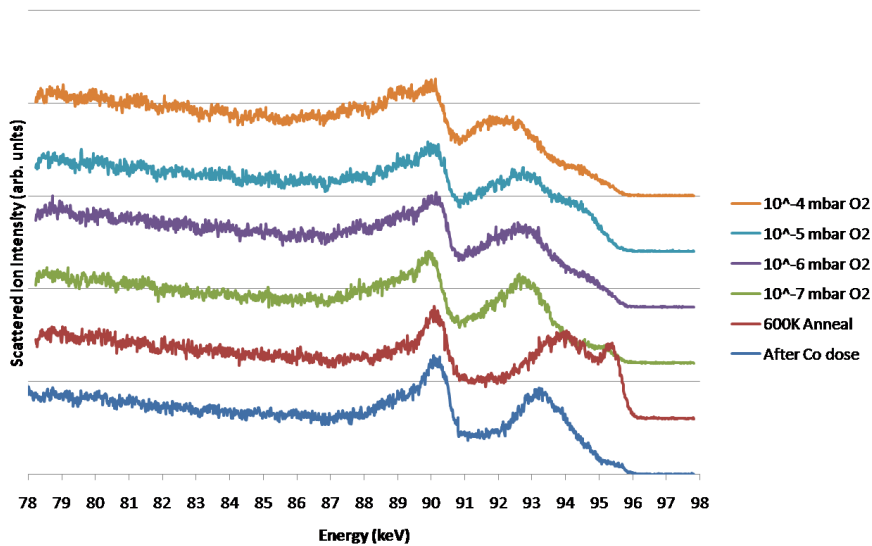
c)

Figure 4.4:- Stacked energy versus intensity data of 4 ML cobalt on Pd{111}, annealed to 560 K before being sequentially exposed to O₂ at increasing pressure increments. The data series correspond to the 1 layer (a), 2 layer (b) and 3 layer (c) alignments.

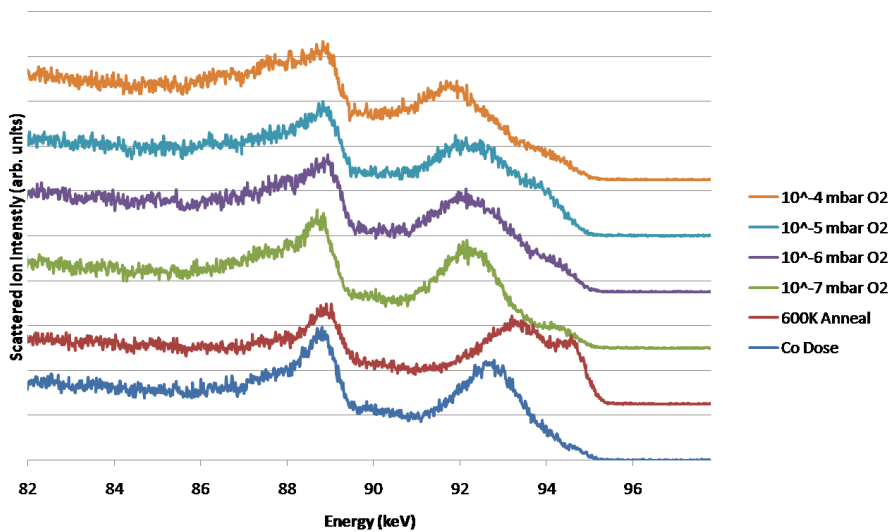
The I vs. E MEIS data for the intermediate alloy composition (figure 4.5) corresponds to the lower limit of the ordered alloy regime discussed in Chapter 3, and exhibits similar behaviour to the 560 K alloy – with changes being observed in the peak profiles with oxygen pressure increases. As before the cobalt feature begins with a strong surface component at 85 keV before developing into an asymmetric peak. The palladium peak, starting with a stronger surface feature at 92 keV (consistent with the intermediate alloy regime in Chapter 3), undergoes large changes. The main sub-surface component shifts down while the surface peak diminishes. As the pressure of the oxygen is sequentially increased, the intensity at 84.5 keV increases until 10⁻⁵ mbar then decreasing at 10⁻⁴ mbar. In addition to this decrease there is also a 0.5 keV shift down in energy for the main palladium feature.



a)



b)



c)

Figure 4.5:- Stacked energy versus intensity data of 4 ML cobalt on Pd{111}, annealed to 600 K before being sequentially exposed to O₂ at increasing pressure increments. The data series correspond to the 1 layer (a), 2 layer (b) and 3 layer (c) alignments.

The MEIS I vs. E data for the CoPd alloy formed at 700 K exposed to oxygen, in figure 4.6, corresponds to the Pd-rich alloy regime, and features consistent peak profiles and intensities throughout the increasing oxygen pressures. The data for 10⁻⁷ mbar O₂ indicates a small increase in the palladium concentration which returns at the next pressure – manifested by an increase in the Pd peak intensity and a drop in the Co peak. In addition there is a lesser increase of the Pd peak in the 10⁻⁵ mbar O₂ data, however there is no noticeable decrease in the Co peak intensity. The palladium peak shifts slightly down in energy after dosing at 10⁻⁶ mbar O₂ and slightly up in energy at 10⁻⁷ mbar O₂.

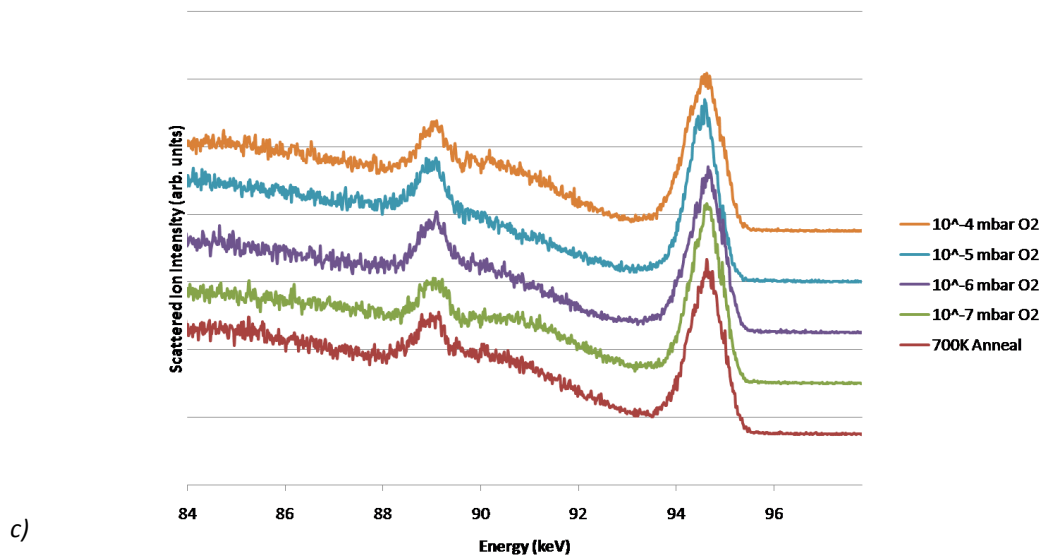
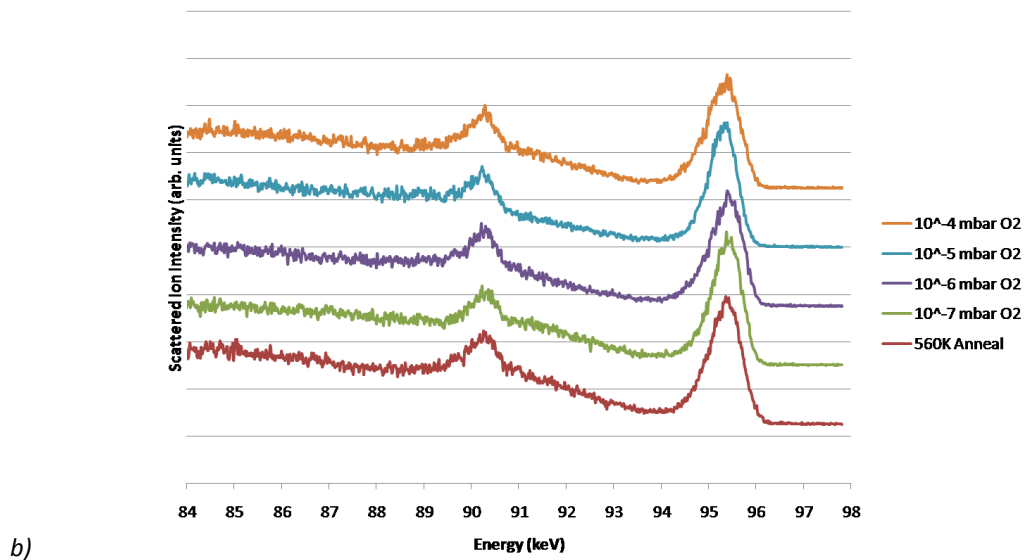
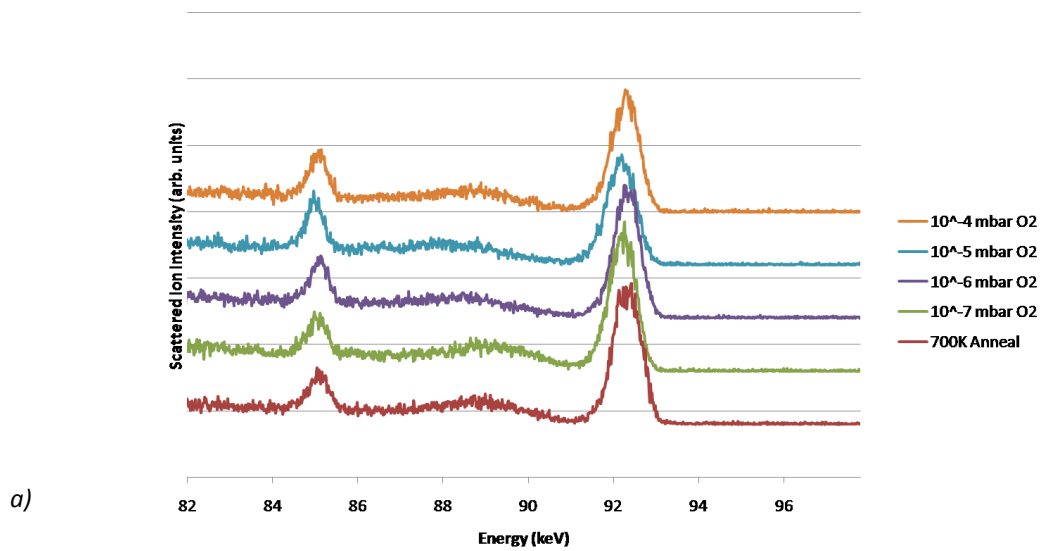


Figure 4.6:- Stacked energy versus intensity data of 4 ML cobalt on Pd{111}, annealed to 700 K before being sequentially exposed to O₂ at increasing pressure increments. The data series correspond to the 1 layer (a), 2 layer (b) and 3 layer (c) alignments.

4.4 Discussion

Cobalt Oxide on Pd{111} - MEIS

After deposition of the cobalt oxide the MEIS spectrum in *figure 4.1* is representative of a fully continuous surface layer. The key indication of this is the palladium peak shifted several electron volts lower in comparison to the clean palladium spectra. At this point the majority of the cobalt (67%) is represented in the surface peak – the other peak at lower energy indicates a non-homogeneous distribution of cobalt. This could result from incomplete oxidation of the cobalt, or a separate, structurally different cobalt oxide phase (possibly with a different stoichiometry). The latter would be agreeable with a similar study [13] where CoO was indicative of lower coverages and Co₃O₄ appeared as the coverage was increased.

The spectra indicate a very stable surface configuration up until 800 K. The shift of the palladium peak as the sample is heated through 400, 500, 600 and 700 K can be explained by the cobalt oxide layer thickness becoming more homogeneous. However this shift is very small and difficult to detect against the spectral noise. Therefore the minor change in homogeneity would be considered as being negligible without the STM as a supporting technique.

The data collected after the 800 K anneal are similar to the 750 K alloy data in *Chapter 3*. After decomposition the spectrum corresponds to a palladium surface with a small percentage of cobalt in solid solution.

Cobalt Oxide on Pd{111} - STM

The island appearance of the surface after deposition in the STM images is indicative of a relatively weak attraction between the surface and the overlayer. The nucleation of these islands is widespread leading to the relatively high dispersion in comparison with the growth of metal on metal islands described in *Chapter 3*.

As the surface is annealed to 400 K the lack of substantial change in the morphology corresponds to the information provided by the MEIS data. The atoms on the surface would therefore have a sufficient diffusion barrier at this temperature to preserve the as deposited structure. The hypothesis was made after the MEIS experiments (along with LEED) that the morphology changes from 400 to 700 K would be slight. The STM images after the 700 K anneal

suggest an alternative hypothesis. The visible surface of the porous surface is clearly different from the island morphology at lower temperatures, however the MEIS indicates that this change is relatively shallow in the deposited oxide and that the structure remains constant.

The decomposition after annealing to 800 K is clearly consistent between the two techniques as well as with the AES and LEED supporting techniques.

CoPd Alloy Segregation – MEIS

Oxygen Adsorption on CoPd (560 K) Alloy on Pd{111}

The cobalt in the 560 K alloy is strongly segregated to the surface during the first oxygen dose at 10^{-7} mbar. Above this pressure the spectra do not drastically change. The spectra at the elevated pressures indicate the surface is essentially 100% cobalt (presumably in the form of cobalt oxide). This is in agreement with the discussed TPD study [11] where the cobalt segregates to the surface, forming cobalt oxide. At the angle corresponding to the 2 layer alignment the surface palladium peak lies at 95.4 keV and above 94 keV there are no counts (excluding the background noise). The changes in the cobalt peak from a well defined surface peak to a wide convoluted peak describe a significant disruption in the cobalt structure preventing efficient blocking.

Oxygen Adsorption on CoPd (600 K) Alloy on Pd{111}

In the 600 K annealed CoPd alloy, the cobalt is again strongly segregated by the oxygen. In contrast to the 560 K alloy the segregation of cobalt is not complete after the 10^{-7} mbar oxygen dose. After dosing at 10^{-6} mbar the segregation partially reverses, signified by the increase in peak intensity around 95 keV corresponding to the palladium surface peak. At this pressure there are no detectable changes in the cobalt surface peak, however this is not surprising with palladium being three times as sensitive. The sub-surface proportion of the cobalt does increase however, indicating a disruption to the cobalt structure – as seen in the 560 K alloy data.

After the 10^{-5} mbar oxygen dose the segregation has reversed further still, although the spectra remains representative of an increase in cobalt composition relative to the alloy before oxygen dosing. The total cobalt peak remains completely unchanged compared to the 10^{-6} mbar spectrum.

The segregation at 10^{-4} mbar dosing reverts back to favouring cobalt indicated by the large decrease in the palladium surface peak. The peak intensity after 10^{-4} mbar decreases substantially but in comparison to 10^{-7} mbar, the segregation does not fully revert. The short length of time dosing 10^{-4} mbar potentially means the diffusion is kinetically inhibited at this pressure.

Oxygen Adsorption on CoPd (700 K) Alloy on Pd{111}

Adsorption of oxygen at a pressure of 10^{-7} mbar causes no measurable segregation of the 700 K alloy. The alloy composition is high in palladium before dosing although substantial cobalt is still present at the surface. Beyond the 10^{-7} mbar dose the changes in the palladium peak are small and undetectable in the cobalt. In view of the aforementioned high sensitivity of palladium this is to be expected – small changes in palladium rich compositions would manifest as small changes in the data.

Segregation begins to be evident from 10^{-6} mbar, evident from careful measurement of the palladium peak. The segregation continues after exposure to oxygen at a pressure 10^{-5} mbar, primarily in the top surface layer. The 2 layer data indicates a small increase in palladium intensity, which is likely to be a consequence of cobalt being depleted as it moves into the top layer. After exposure to oxygen at 10^{-4} mbar the palladium composition remains essentially constant in each geometry.

It is also important to discuss the possible cobalt oxidation states, and therefore the stoichiometry of the cobalt oxide. These data do not provide enough clear information to conclusively point to either CoO or Co_3O_4 , although previous work [7, 8, 11-14] would suggest both structures exist and are highly likely to be dependent on the surface defects. The large doses of oxygen certainly provide more than enough oxygen atoms to saturate the surface and with the large sticking coefficients and fast bulk absorption rates for cobalt [7], the existence of metallic cobalt is effectively ruled out. The evidence given by Kim *et al* [14] indicates that both structures are formed and the decomposition of the Co_3O_4 at 700 K could explain the change in morphology seen in the STM images.

A valuable continuation to this work would be to use photoelectron spectroscopy such as XPS to characterise the chemical environments in these particular experiments and compare these to the Pt_3Co study [13] discussed previously.

Extending these experiments to examine chemical reduction of the oxidised surfaces, possibly using analogous pressure experiments, using H₂ and CO would also be useful. Such experiments, including a comparison with the oxygen on palladium experiments [9], would provide direct quantification on the reducibility under FTS conditions, adding to the above thermal decomposition data.

4.5 Conclusions

Cobalt Oxide on Pd{111}

At low coverages cobalt oxide deposited on palladium possesses an island like morphology with a high dispersion, associated by small particle sizes (average diameter 6.5 Å). As further material is deposited the particles grow according to Volmer-Weber particle growth theory and eventually forms a fully continuous overlayer; with no surface palladium visible, but still outwardly appearing to have island like morphology.

As the sample is heated the island morphology remains through 400, 500 and 600 K before changing in appearance at 700 K to a flat overlayer with pore type structures limited to the uppermost cobalt oxide layer. After deposition and throughout annealing the cobalt oxide maintains the same average thickness and the structure does not become pseudomorphic with the underlying palladium at any point. At 700 K a small amount of palladium begins to diffuse through into the oxide overlayer.

The cobalt oxide overlayer decomposes after 800 K with the majority of the cobalt being absorbed into the bulk. The appearance of the surface is comparable with the crystal close to the end of the cleaning process, and a small quantity of cobalt remains detectable in the near surface region.

Oxygen Adsorption on CoPd alloys on Pd{111}

In a cobalt palladium alloy, oxygen strongly segregates cobalt to the surface across a range of alloy compositions. The segregation associated with reaction of the cobalt with the oxygen atoms resulting in the formation of a cobalt oxide overlayer. After saturation there is a small reverse in the segregation, coupled with increases in the palladium MEIS and AES peaks.

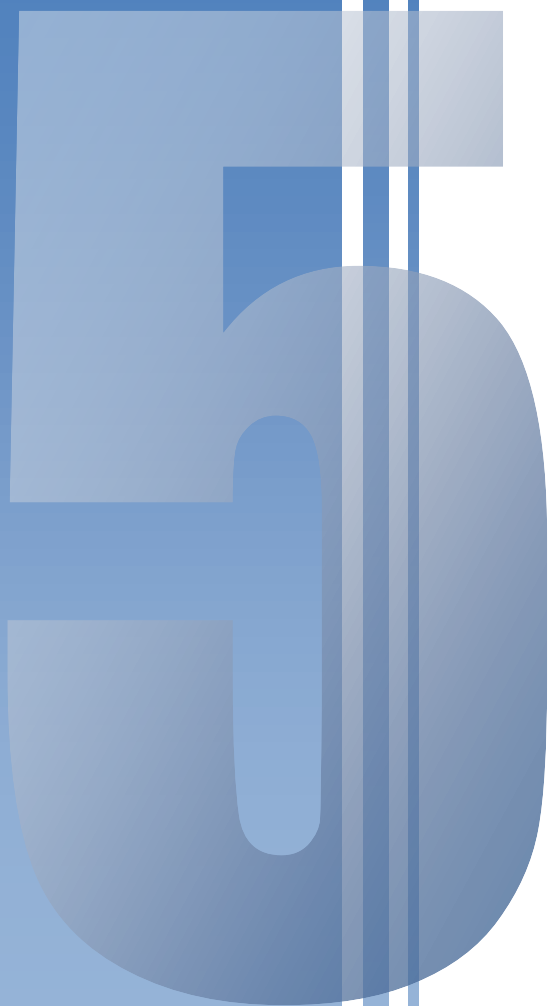
The cobalt-rich alloy (560 K anneal) oxidises rapidly at 10^{-7} mbar, with the oxygen AES signal reaching maximum intensity at this pressure. In the intermediate, 600 K alloy, the segregation at 10^{-7} mbar continues at 10^{-6} mbar. After 10^{-5} mbar there is an increase in the surface palladium content, more prominent than that of the cobalt rich alloy. The increased cobalt visibility in the MEIS spectra of each alloy adds to the hypothesis of cobalt oxidation, explained by a change in cobalt atomic sites in the oxide structure compared to metallic cobalt.

Palladium rich alloys indicate the same cobalt segregation, but the effects are less noticeable due to the reduced cobalt reservoir at near-surface depths.

4.6 Bibliography

- [1] Khodakov A. Y. *et al*, Advances in the Development of Novel Cobalt Fischer-Tropsch Catalysts for Synthesis of Long-Chain Hydrocarbons and Clean Fuels, *Chem. Rev.* 107 (2007), 1692-1744
- [2] *Handbook of Preparative Inorganic Chemistry, 2nd Ed.* Edited by G. Bauer, Academic Press, 1963, NY. p. 1675.
- [3] Schindler K. M. *et al*, Low-energy diffraction structure determination of an ultrathin CoO film on Ag(001), *Surf. Sci.* 603 (2009), 2658-2663
- [4] Gragnaniello L. *et al*, *Cobalt oxide nanolayers on Pd(100): The thickness-dependent structural evolution*, *Surf. Sci.* 604 (2010) 2002-2011
- [5] Petitto S. C. *et al*, *Cobalt oxide surface chemistry: The interaction of CoO(100), Co₃O₄(110) and Co₃O₄(111) with oxygen and water*, *J. Mol. Catal. A* 281, 1-2 (2008), 49-58
- [6] Van de Loosdrecht J. *et al*, *Cobalt Fischer-Tropsch synthesis: Deactivation by oxidation?*, *Catal. Today* 123 (2007), 293-302
- [7] Matsuyama T. *et al*, *LEED-AES study of the temperature dependent oxidation of the Co(0001)*, *Surf. Sci.* 102, 1 (1981), 18-28
- [8] Castro G. R. *et al*, *Interaction of oxygen with hcp (0001) recrystallised cobalt surfaces*, *Surf. Sci.* 123, 2-3 (1982), 456-470
- [9] Leisenberger F. P. *et al*, *Surface and subsurface oxygen on Pd(111)*, *Surf. Sci.* 445, 2-3 (2000), 380-393
- [10] Klötzer B. *et al*, *Oxygen-induced surface phase transformation of Pd(111): sticking, adsorption and desorption kinetics*, *Surf. Sci.* 482-485 (2001), 237-242
- [11] Krawczyk M., *Oxygen adsorption on binary Co₅₀Pd₅₀ alloy surfaces*, *Vacuum* 63 (2001), 23-27
- [12] Krawczyk M. *et al*, *Surface characterisation of cobalt-palladium alloys*, *Appl. Surf. Sci.* 235 (2004), 49-52
- [13] An K. S. *et al*, *Surface structure and segregation of ordered Pt₃Co(110) induced by oxygen*, *Surf. Sci.* 401, 3 (1998), 336-343
- [14] Kim W. *et al*, *Oxidation and Annealing Effect on Cobalt Films On Palladium(111)*, *Surf. Rev. Lett.* 9 (2002), 931-936

*The Adsorption of CO, H₂ and Syngas
on CoPd Alloys on Pd{111}*



5.1 Introduction

In *Chapter 3* the structure and composition of cobalt palladium alloys on a Pd{111} surface were characterised under UHV conditions by STM and MEIS. In *Chapter 4* the interaction of oxygen with cobalt palladium bimetallic surfaces was studied. In this chapter a range of alloy surfaces of different compositions are exposed to pure carbon monoxide and hydrogen as well as a hydrogen rich mixture of the two gases, known in FTS as ‘syngas’. The aim of these experiments is to provide a closer understanding of how the alloys behave under chemical environments more closely correlated with the ‘real’ catalyst system.

In bimetallic alloys the surface composition is likely to be different to that of the bulk composition [1]. The behaviour of the surface in an inert atmosphere, such as an ultra high vacuum, will be governed by the thermodynamic properties of the metals present as well as the atomic sizes. When the alloy surface is exposed to a reactive gas each metal will interact differently with the gas molecules causing the thermodynamic equilibrium between the bulk and surface compositions to change. This change manifests itself in a change in the composition of the surface, also known as adsorbate induced segregation [1].

The most significant influence on the surface is the bonding energies of the adsorbate to each metal. In theory, the metal with the highest bonding energy to the gas should segregate to the surface. Additional factors to this hypothesis include; which adsorption sites are ‘preferred’ by the adsorbate and how electronic effects from alloying of the two metals affect the metal-adsorbate bonding. In practice the gas may adsorb on each metal at different sites, have different geometries and have a difference in packing density. These properties are therefore difficult to predict for the bimetallic alloy. However, it is important to consider the behaviour of the gases on each metal.

The Adsorption of Carbon Monoxide on Cobalt Surfaces

Under UHV conditions the adsorption of carbon monoxide on the Co{0001} surfaces are examined by Lahtinen and co-workers using several techniques [2-3]. The first of these studies [2], using XPS, TPD and LEED, indicated a $(\sqrt{3}\times\sqrt{3})R30^\circ$ -CO structure at room temperature with CO adsorbed at atop sites (higher packing densities are possible at lower temperatures). Another study [3] using I-V-LEED expands on the initial study with the conclusion that CO induces a buckling of the cobalt surface resulting from the adsorption site atoms being ‘pulled’ up by 0.04 Å. A number of

other studies on the Co {0001} surface corroborate the $(\sqrt{3}\times\sqrt{3})R30^\circ$ -CO structure [4-5] as part of larger studies on this surface.

DFT calculations [6] of adsorbed carbon on an fcc Co{111} surface indicate that the surface could reconstruct to a {100} type surface above a coverage of 0.25 ML. This possible reconstruction is based on the adsorbed species preferring a more open surface. Carbon monoxide does not have such a large influence on the surface and no reconstruction is expected, however the data signify that the bonding energy is coverage dependent above 0.5 ML coverage [6].

Beitel and co-workers have examined the adsorption of CO on the Co{0001} surface using RAIRS [7]. CO adsorption is examined *in situ* at pressures ranging from 10^{-7} to 10^3 mbar using a high pressure cell. Only one peak associated with atop adsorption was observed for the low defect surface which shifts up in wavenumbers from 2012 to 2047 cm^{-1} with an approximately linear trend relative to the logarithmic pressure axis. The trend continues until 1 mbar then the peak shifts down with increasing pressure to 2025 cm^{-1} . The RAIRS data for these experiments are represented in figure 5.1.

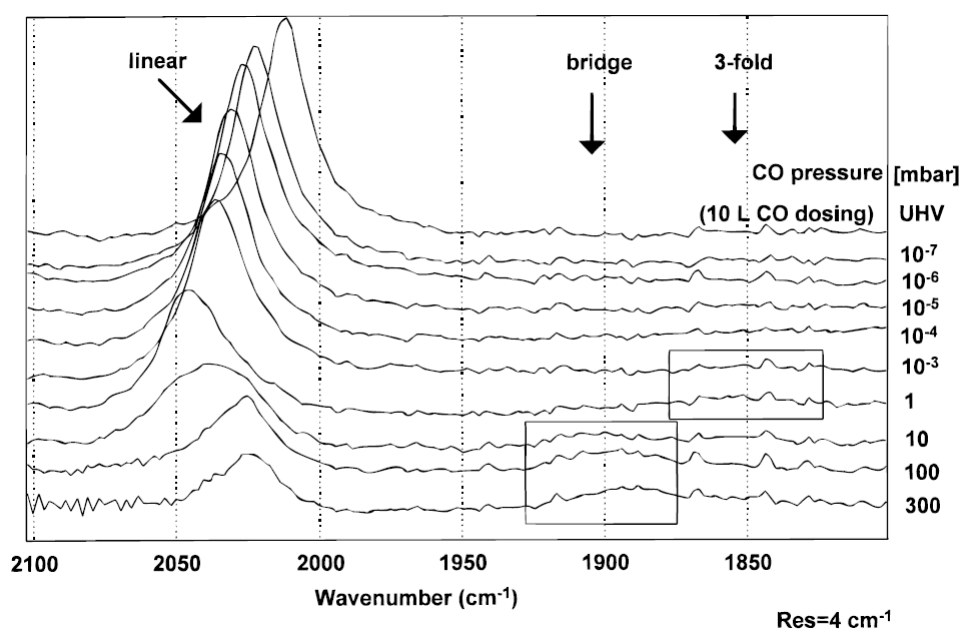


Figure 5.1:- CO adsorption on Co{0001} as a function of pressure as examined using RAIRS [7].

The adsorption of carbon monoxide on Co{10-10} (a surface with a corrugated structure) was studied by Toomes *et al* using RAIRS [8]. Initially, at low coverages, the CO adsorbs on atop sites characterised by a C-O stretch between 1972 and 2020 cm^{-1} and a $p(2\times 1)$ LEED pattern. At exposures greater than 0.5 L the atop adsorption is gradually replaced by bridge site adsorption giving rise to a more complex LEED pattern (figure 5.2b) and an additional peak in the RAIRS spectra starting at

1926 cm^{-1} , then shifting up to 1963 cm^{-1} . At exposures exceeding 1 L the RAIRS was dominated by a single peak at 1984 cm^{-1} and the LEED pattern became an incommensurate $c(2 \times 6)$ – similar to a $c(2 \times 1)$ where the positions of the CO molecules are offset, giving a concertina-like distribution of molecules.

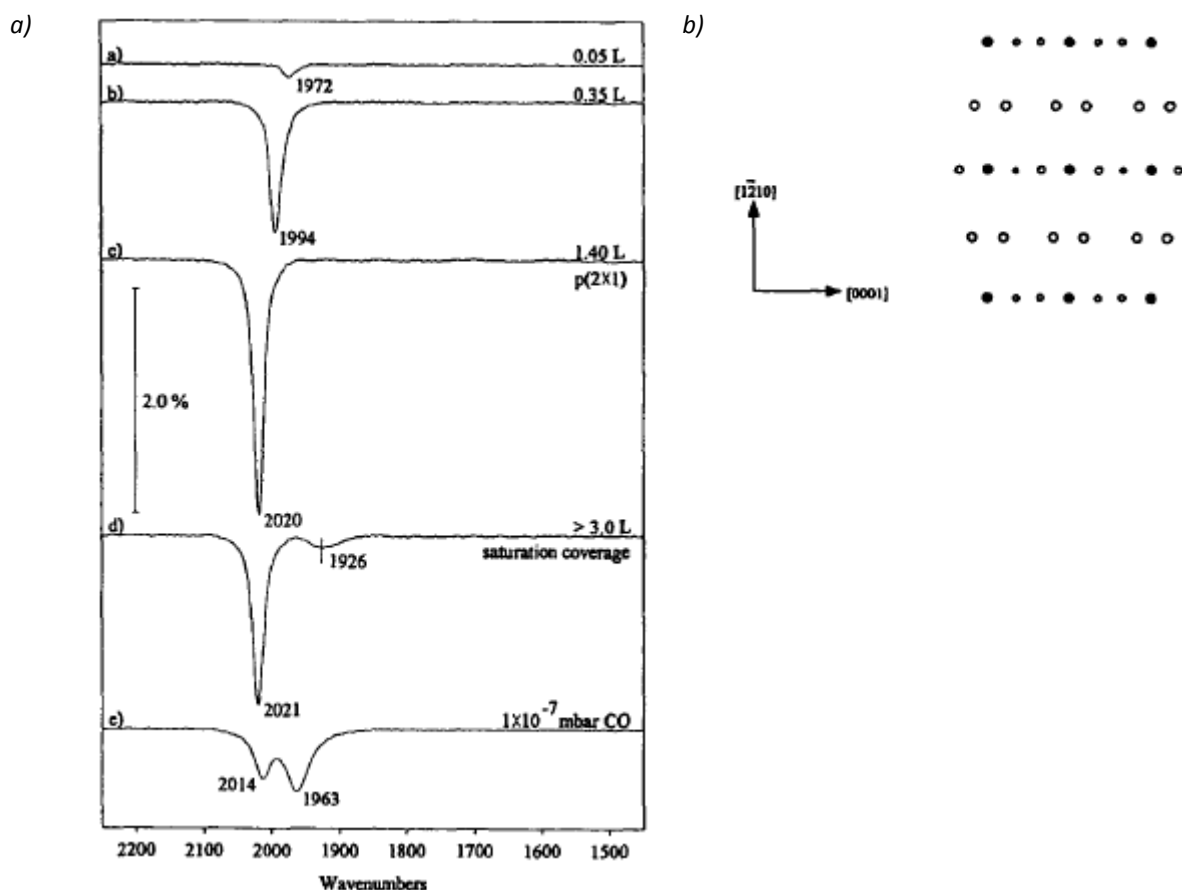


Figure 5.2:- RAIRS spectra describing the behaviour of CO on Co{10-10} at various coverages (a) and schematic representation of the LEED pattern observed at saturation coverage (b) [8].

The Adsorption of Carbon Monoxide on Palladium Surfaces

The adsorption of CO on Pd{111} at room temperature was examined using high resolution XPS and HREELS [9]. Low exposures of CO were dominated by threefold hollow sites which gave rise to a $(\sqrt{3} \times \sqrt{3}) R30^\circ$ LEED structure. As the coverage was increased towards the saturation coverage of 0.5 L, the spectra indicated the appearance of bridge site adsorption accompanied by a decrease in the ordering of the observed LEED pattern.

The adsorption on Pd{111} was also examined using RAIRS [10], as well as on the {100} and {210} faces. Below exposures of 0.5 L of CO the infrared peaks corresponded to adsorption in 3-fold hollow sites; the peak then shifted up in frequency as the coverage was increased to 1946 cm^{-1} at 10^{-5} torr. The change in peak position was attributed to CO being pushed into the bridging sites as



the number of molecules on the surface increase. As the pressure of CO was increased to 10^{-5} torr an additional peak appeared at 2092 cm^{-1} that can be assigned as adsorption at the Pd atop sites.

Kuhn *et al* have examined the pressure and temperature dependence of CO adsorption on the Pd{111} substrate [11]. Adsorption of CO at 10^{-6} mbar at elevated temperatures was in the 3 fold hollow sites. As the temperature was decreased, the peak shifts from around 1850 cm^{-1} at 500 K up to 1962 cm^{-1} at 200 K (approximately 1940 cm^{-1} at 300 K) attributed to a gradual change from 3 fold adsorption sites to bridging sites. In addition there was a small peak that appeared at 2070 cm^{-1} below 350 K resulting from atop site adsorption. Below 150 K the 1962 cm^{-1} peak diminished to leave two peaks at 2110 and 1895 cm^{-1} corresponding to atop and 3 fold sites respectively. These data are important for comparison with the experiments discussed in this chapter due to the saturation exposures used and the exposure at different pressures. Importantly the dominating adsorption site at 300 K remained the same across all pressures below 1 torr.

The Adsorption of Carbon Monoxide on CoPd Alloy Surfaces

Matolinova *et al* examined the adsorption of carbon monoxide on cobalt palladium alloy particles grown on sapphire ($\alpha\text{-Al}_2\text{O}_3$) [12]. Using TPD and XPS, the bimetallic system was observed as having lower bonding energies (lower desorption temperature) in comparison to the individual metals. In addition to these conclusions, SSIMS (Static Secondary Ion Mass Spectroscopy) was used to show that the CO partially dissociates on the CoPd alloy.

The adsorption of CO on relatively thick cobalt thin films on Pd{111} was examined with XANES and EXAFS [13]. The cobalt overlayer, confirmed as having an fcc structure, was found to be structurally unchanged after exposure to CO, although there was an electronic influence from the CO. The thickness of the cobalt layer in this case, along with the conclusion that intermixing is minimal at room temperature, would make any segregation effects unlikely – effectively the surface is equivalent to that of a fcc Co{111} crystal.

The Adsorption of Hydrogen on Cobalt and Palladium Surfaces

Hydrogen adsorbs dissociatively on Co{0001} at 300 K [14] as was observed for numerous metal surfaces [15]. Desorption occurred at approximately 400 K with second order kinetics and an

activation energy of $67 \pm 8 \text{ kJ mol}^{-1}$ [14]. The initial sticking probability was relatively low at 0.04 and saturation is reached by 0.1 L.

Winkler has reviewed the interaction of hydrogen with Pd{111} surfaces [16]. The initial sticking probability was given as 0.45 and was largely independent of temperature. The hydrogen adsorbs dissociatively at room temperature and desorbs at approximately 300 K. However atomic hydrogen is also easily absorbed into the bulk at room temperature forming a solid solution with the palladium under large hydrogen exposures. The atomic hydrogen absorbed in the bulk outgases at 500 K resulting in a broad desorption peak extending from 500 to 1000 K.

H₂/CO Co-adsorbed on Cobalt

Following examination of hydrogen adsorption on Co{0001} Bridge *et al* studied the co-adsorption of hydrogen and carbon monoxide [14]. The desorption spectra demonstrate that neither gas affects the binding energy of the other. The intensity of the CO adsorption is unaffected from pre-exposure or post-exposure to hydrogen; the hydrogen however, is easily displaced by CO and less adsorption was also indicated following CO exposure on Co{0001}. This would suggest that the CO is more likely to influence the alloy surface and any segregation effects during co-adsorption would be expected to follow the same trends as those seen for CO adsorption alone.

H₂/CO Co-adsorbed on Palladium

Kiskinova and Bliznakov have examined the adsorption and coadsorption of CO and H₂ on Pd(111) [17]. The changes in the desorption spectra are similar to those seen from the Co{0001} surface [14]. CO easily displaces hydrogen from the surface leading to decreased peak intensity in the H₂ desorption spectra. In the case of palladium hydrogen does have a site specific influence on CO adsorption. Above 300 K, in the absence of hydrogen, CO adsorbs in two sites which can be attributed to 3-fold and bridge sites by comparison to the study using infrared spectroscopy [11]. When substantial amounts of hydrogen are pre-absorbed the peak corresponding to the 3-fold site decreases in intensity. The overall dominance of CO during co-adsorption gives more weight to the hypothesis that alloy behaviour is likely to be influenced by CO more than H₂.

5.2 Experimental

The fcc Pd{111} crystal substrate [Surface Preparation Laboratories] used in all experiments, was cleaned using cycles of Ar⁺ sputtering (1.5 keV, 10-20 μ A crystal current) followed by annealing to 1100 K. The condition of the surface was considered to be clean when a clear 1x1 LEED pattern could be seen, combined with either an AES spectrum presenting no impurities (MEIS apparatus), or an STM image indicating a clean surface with large terraces (STM apparatus).

Influence of Gas Adsorption on CoPd alloys on Pd{111}

For the segregation experiments, the alloy was first prepared in accordance with the experiments in *Chapter 3*. Around 5 ML of cobalt (estimated with MEIS) is deposited for each experiment and then annealed to one of the selected temperatures – 560, 600 and 700 K – chosen to test alloy surface ranging from cobalt rich to palladium rich. For reference, data were collected for the prepared samples before exposure to each gas. In addition these preparation temperatures correspond to earlier TPD/AES work on oxygen adsorption on the binary bulk alloy [18, 19].

Each gas was dosed at 300 K in the preparation chamber at progressively increasing pressures, 10^{-7} , 10^{-6} , 10^{-5} and 10^{-4} mbar, transferring and collecting MEIS data in between. The gas dose was kept constant for each pressure, maintaining 1000 L of carbon monoxide, hydrogen or syngas in each case by altering the dose time – the basis of this is discussed in *section 2.2*. The syngas has a fixed composition of 30% carbon monoxide, 70% hydrogen. The carbon monoxide and syngas were fed into the vacuum chambers *via* a cold trap to remove potential volatile metal carbonyl compounds that could potentially be formed inside the cylinders or gas lines. The cold trap consisted of acetone cooled to its freezing point at -95 °C (178 K) using liquid nitrogen as a coolant.

During all MEIS data collection, the crystal was in an aligned geometry along the [-1-12] azimuth with the beam incident along the [-1-1-4] direction which corresponds to an illumination of the top three layers of an ideal fcc {111} surface. The detector was aligned to two different scattering angle ranges centred at 86° and 106° – the subsequent data make up the blocking channels in 1-layer, 2-layer and 3-layer geometries of the ideal surface.

Reflection absorption infrared spectroscopy (RAIRS) experiments monitoring adsorption at 300 K were carried out after the STM experiments of *Chapter 3* following 50 K annealing

temperature increments from 450 to 850 K. Following imaging, the sample was transferred to the RAIRS chamber where it was aligned and background spectra were taken. An experiment analogous to the one carried out at the MEIS facility is performed, exposing the sample to gas at varying pressures from 10^{-7} to 10^{-4} mbar. In addition to the post exposure data collection, the RAIRS apparatus allows *in situ* scanning which can be done at 10^{-7} and 10^{-6} mbar. This is not possible at the higher pressures because the scanning time exceeds the shorter dosing times. It was deemed more important to retain consistency between the RAIRS and MEIS experiments and maintain the 1000 L dose than to extend the dose to allow the *in situ* RAIRS analysis.

Before the results are presented it is important to note that there is a systematic discrepancy between thermocouples on the STM/RAIRS and MEIS apparatus. The temperature reading is approximately 75 K higher at 900 K on the MEIS apparatus and the discrepancy diminishes linearly to 0 at 300 K, as judged from the visual appearance of the crystal upon annealing beyond 850 K during the cleaning procedure and pyrometer measurements above 600 K. As discussed in *Chapter 3*, slightly higher temperatures are required to create the alloy surfaces prepared in the MEIS apparatus.

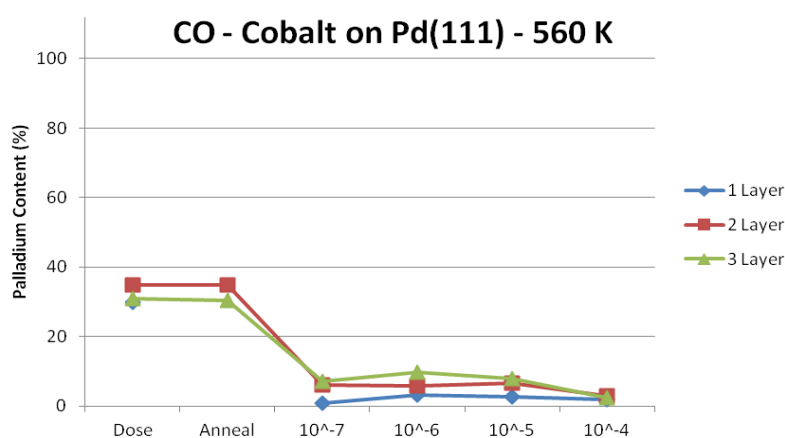
5.3 Results

The MEIS scattered ion intensity versus energy (I vs. E) spectra presented in this chapter are described as being derived from 1-layer, 2-layer and 3-layer geometries referring to outgoing blocking directions of the clean Pd{111} surface at scattering angles of 109.4°, 84.3° and 90°. These spectra are obtained by the integration method discussed in *section 2.7*. In each I vs. E spectra, up to three peaks may be observed – the lowest energy peak is assigned as cobalt, the highest as palladium surface and the central peak as sub-surface palladium. The compositional graphs of Pd % for each experiment are obtained by referencing the peak intensity of the surface palladium peak against the same peak in the data collected for the clean Pd{111} sample.

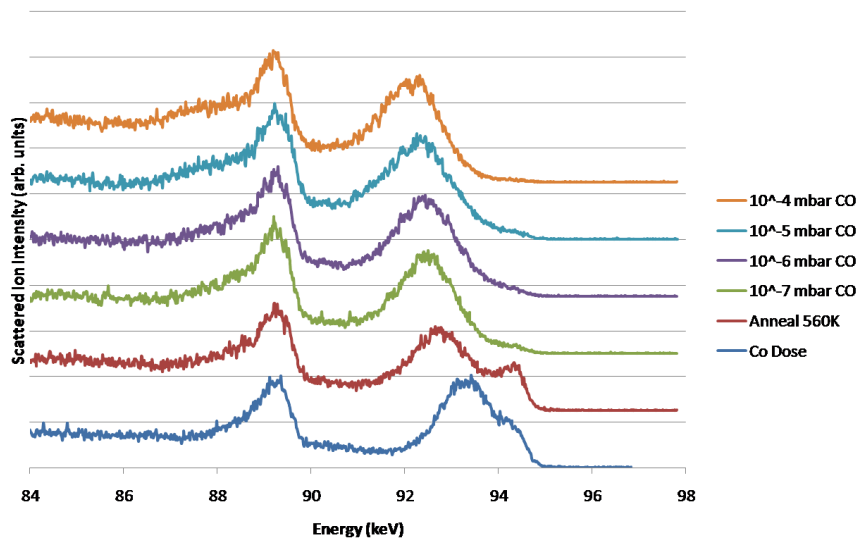
Carbon Monoxide Adsorption on CoPd Alloys on Pd{111} – MEIS

Co Rich Alloy – Pre-Annealing at 560 K – CO Adsorption at 300 K

The MEIS data in *Figure 5.3* describe the surface behaviour following adsorption of CO on a cobalt rich CoPd alloy surface, formed by annealing to 560 K as a function of CO partial pressure. Comparison between the post annealing spectrum to the alloy compositions discussed in *Chapter 3* reveals that the alloy surface has a composition of around 30% Pd in the top three layers. In *figure 5.3b*, it is clear that the surface palladium peak disappears after 1000 L exposure to CO at 10^{-7} mbar. In addition there is a small shift down in energy of the sub-surface peak, and the cobalt peak marginally increases in intensity after exposure. The absence of the 1 layer data series for the exposure to CO at 10^{-7} mbar is due to a problem with data acquisition at the 106° analyser angle for this experiment.



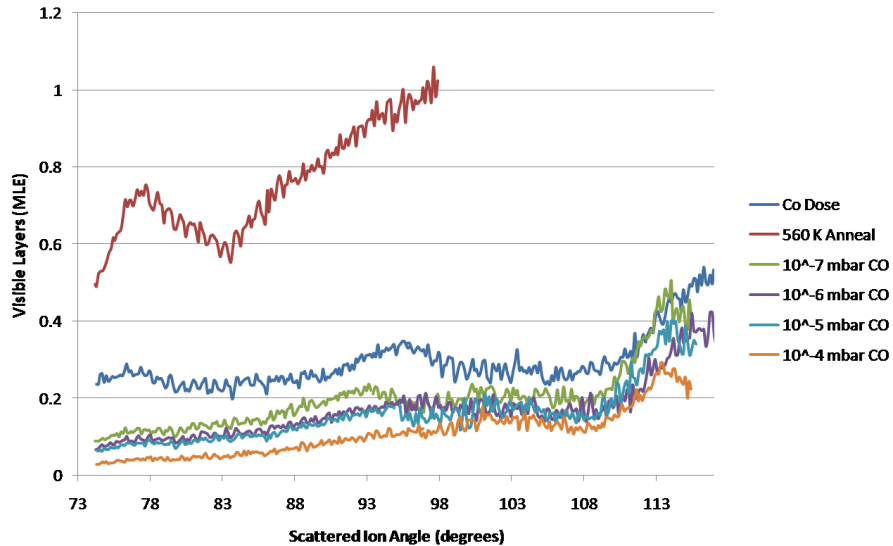
a)



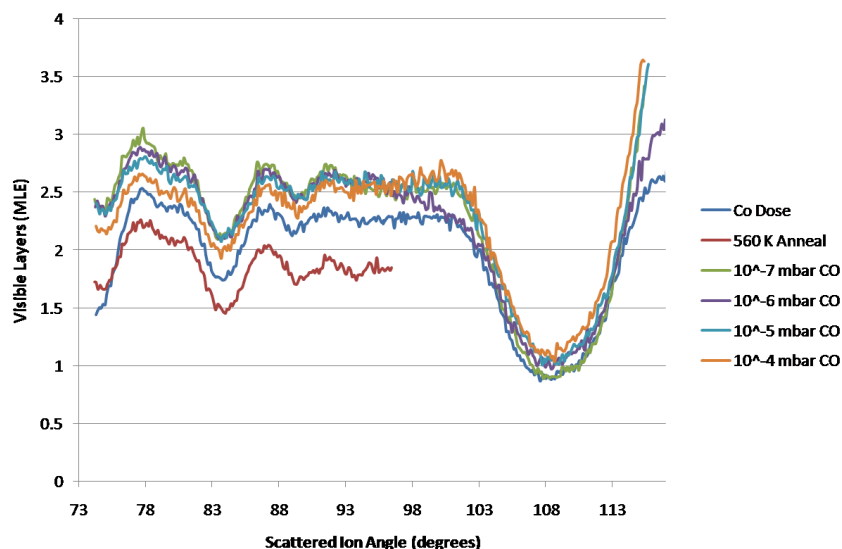
b)

Figure 5.3:- Composition of the surface in Pd % (a) and stacked scattered ion intensity versus energy data (b) of 4 ML cobalt on Pd {111}, annealed to 560 K before being sequentially exposed to CO at increasing pressure increments.

The scattering ion intensity versus scattering angle (I vs. θ) data, presented in figure 5.4, are consistent with the scattered ion intensity versus energy and data and the determined composition (figure 5.3). The absolute yield of the total palladium is observed as remaining constant throughout (i.e. increases in the Pd surface are mirrored by decreases in the Pd sub-surface).



a)

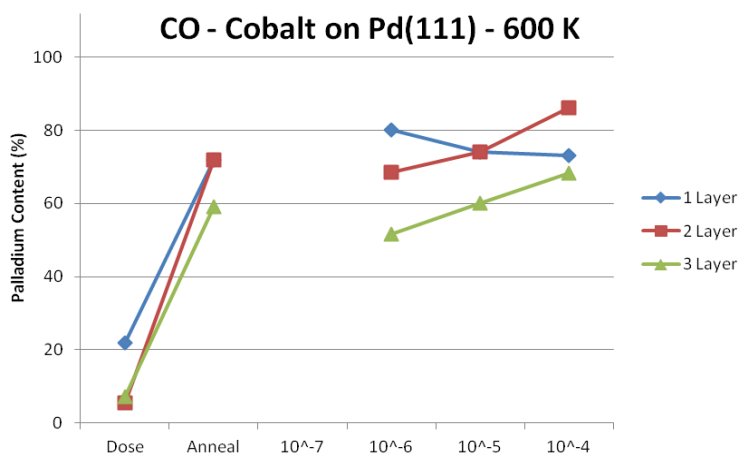


b)

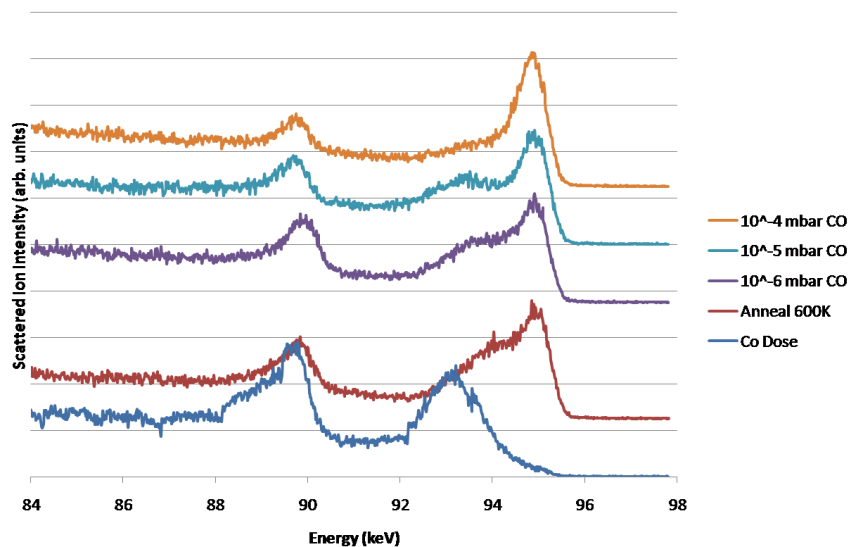
Figure 5.4:- Scattered ion intensity versus scattering angle data of 4 ML cobalt on Pd {111}, annealed to 560 K before being sequentially exposed to CO at increasing pressure increments. Data series correspond to the surface palladium peak (a) and the sub-surface palladium peak (b).

Intermediate Composition Alloy – Pre-Annealing at 600 K – CO Adsorption at 300 K

Figure 5.5b presents the I vs. E plots for a CoPd surface alloy with approximately 65% palladium (As shown in figure 5.5a) exposed to increasing pressures of CO. This composition of the surface corresponds to the upper end of the regime in which the stable ordered CoPd is found (Chapter 3) before the cobalt dissolves into the bulk. After subsequent CO exposure at 10⁻⁶, 10⁻⁵ and 10⁻⁴ mbar, the Pd surface peak in figure 5.5b essentially retains a constant intensity while the Pd sub-surface shoulder drops gradually in intensity.



a)

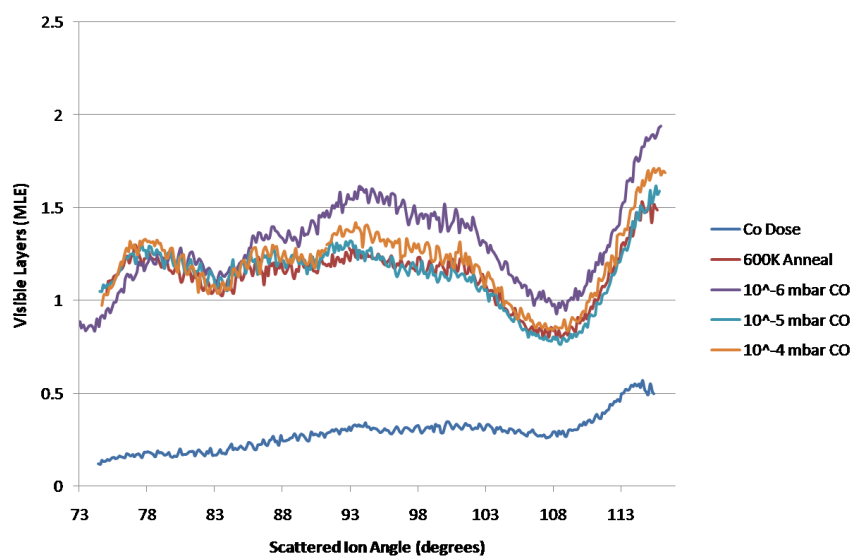


b)

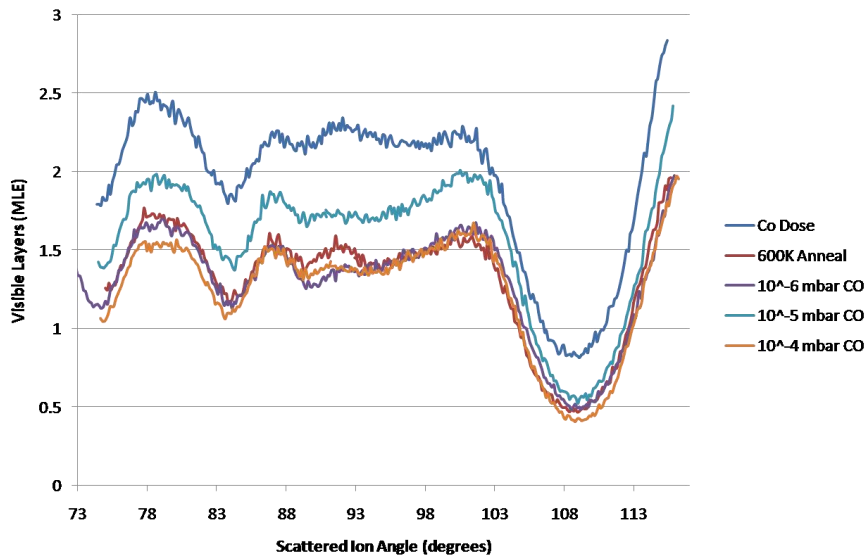
Figure 5.5:- Composition of the surface in Pd % (a) and stacked scattered ion intensity versus energy data (b) of 4 ML cobalt on Pd {111}, annealed to 600 K before being sequentially exposed to CO at increasing pressure increments.

The scattered ion intensity (normalised to number of visible layers) versus scattering angle data are presented in figure 5.6. The changes between the spectra following each incremental CO exposure are relatively small. The spectrum with the lower intensity palladium surface peaks; after cobalt dosing – displays a lower absolute yield in the surface data (figure 5.6a) and a higher yield in the sub-surface data (figure 5.6b). When these two peaks are taken together in the total Pd spectrum the yield is similar to the post-annealing spectrum, as seen in figure 5.6c.

The absolute yield in the sub-surface data (figure 5.6b) does not remain constant. The 10^{-5} mbar CO exposure gives rise to an increase in the sub-surface yield (in comparison with the previous spectra), whilst the surface Pd yield remains constant. The sub-surface increase is not immediately apparent in the I vs. E data (figures 5.5b) due to the change in peak position.



a)

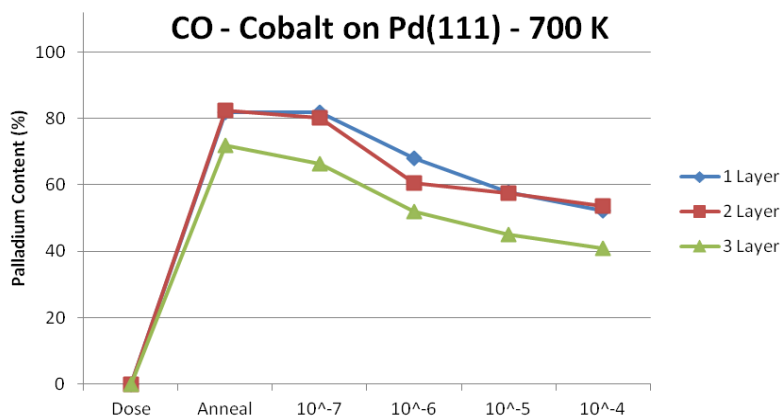


b)

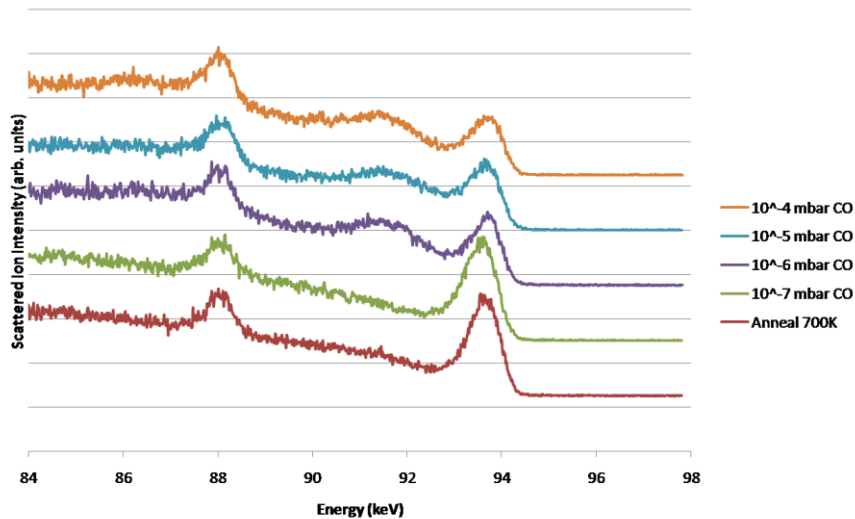
Figure 5.6:- Scattered ion intensity versus scattering angle data of 4 ML cobalt on Pd {111}, annealed to 600 K before being sequentially exposed to CO at increasing pressure increments. Data series correspond to the surface palladium peak (a) and the sub-surface palladium peak (b).

Pd Rich Alloy – Pre-Annealing at 700 K – CO Adsorption at 300 K

The MEIS data and compositional graph for CO exposures at varying pressures on a CoPd alloy with a starting composition of 80% are given in figure 5.7. Adsorption of CO clearly results in a change in the palladium composition of the surface. The drop in surface palladium is associated with the appearance of a noticeable Pd sub-surface peak after exposure to 10^{-6} mbar. The Pd surface composition is indicated as falling from 80% Pd after annealing, to 50% after exposure to 10^{-4} mbar of CO.



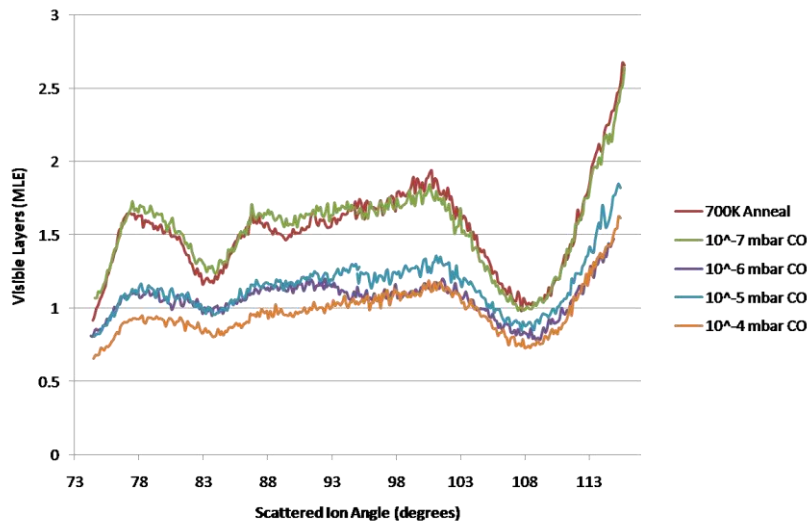
a)



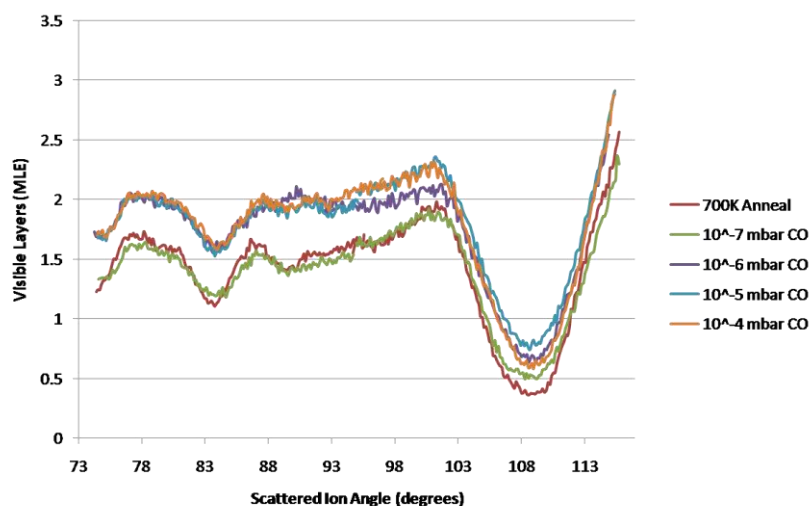
b)

Figure 5.7:- Composition of the surface in Pd % (a) and stacked scattered ion intensity versus energy data (b) of 4 ML cobalt on Pd {111}, annealed to 700 K before being sequentially exposed to CO at increasing pressure increments.

Presented in figure 5.8, the I vs. θ MEIS data clearly correspond to the I vs. E MEIS data (figure 5.7). The Pd surface (figure 5.8a) absolute yield decreases at pressures beyond 10⁻⁶ mbar, while the Pd sub-surface (figure 5.8b) yield increases. The total visible palladium remains constant through all CO exposures, as seen in figure 5.8c.



a)



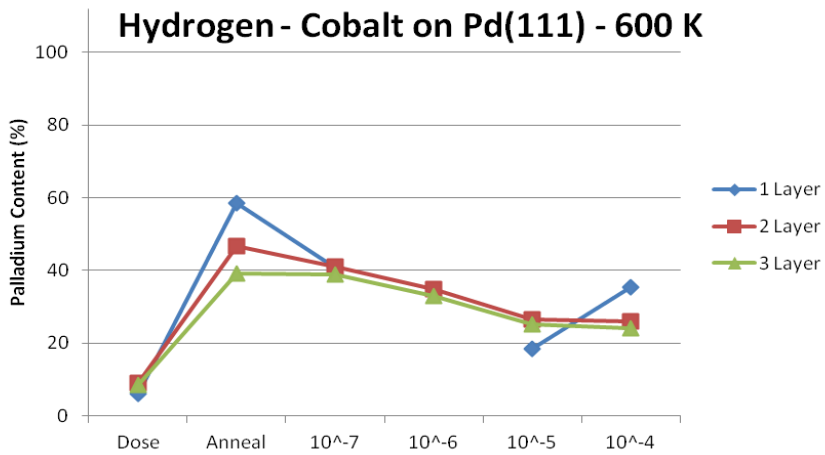
b)

Figure 5.8:- Scattered ion intensity versus scattering angle data of 4 ML cobalt on Pd {111}, annealed to 700 K before being sequentially exposed to CO at increasing pressure increments. Data series correspond to the surface palladium peak (a) and the sub-surface palladium peak (b).

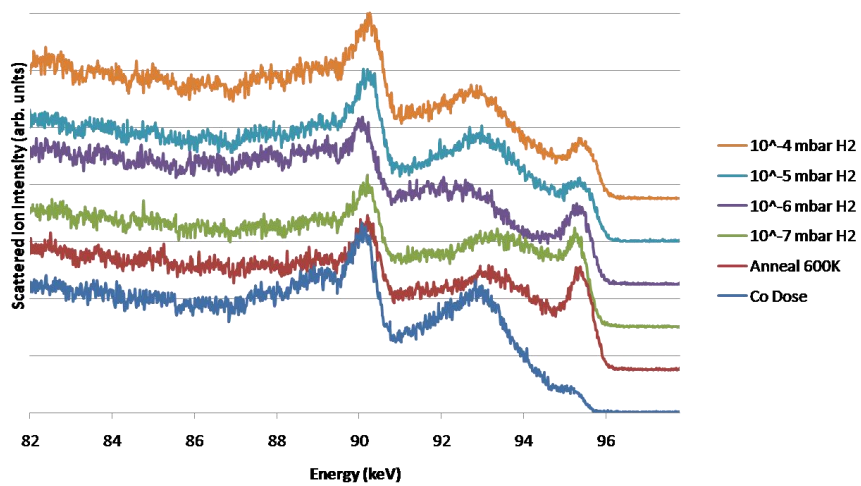
Hydrogen Adsorption on CoPd Alloys on Pd{111} – MEIS

Intermediate Composition Alloy – Pre-Annealing at 600 K – H₂ adsorption at 300 K

Presented in *figure 5.9* are the MEIS data for the adsorption of hydrogen on a CoPd alloy film at a range of partial pressures of H₂. Comparison of the data with the annealing experiment in *Chapter 3* indicates that the surface alloy has approximately 50% Pd composition, corresponding to the ordered alloy regime with p(2x1) LEED pattern. The palladium surface peak is observed to decrease in intensity after the adsorption at 10⁻⁷ mbar. The trend of reduction in palladium content continues higher pressures, particularly in the 2-layer and 3-layer geometries with the final composition at around 25-30% Pd. In the 1-layer geometry, the spectrum appeared dramatically different; however comparing the AES spectrum for this pressure with the other experiments, shown in *figure 5.9c*, leads to the conclusion that there is an experimental problem. Discounting the 1-layer spectrum for the 10⁻⁶ mbar experiment, the cobalt peak exhibits small trend of increasing intensity as the pressure is increased.

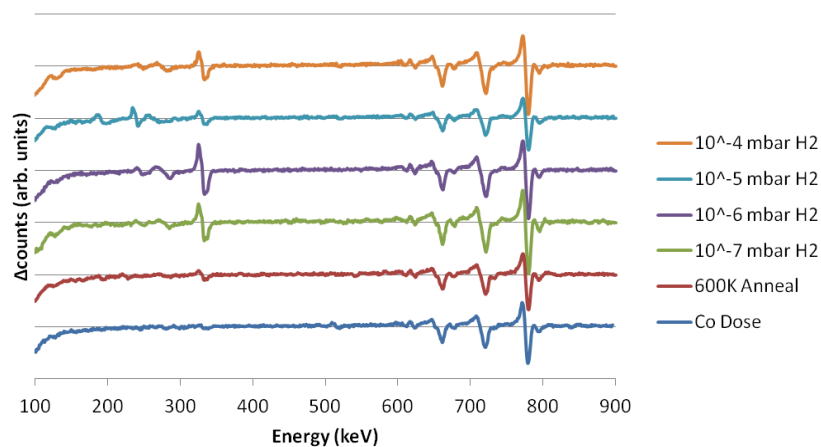


a)



b)

Hydrogen Segregation Auger Spectra - 600 K



c)

Figure 5.9:- Composition of the surface in Pd % (a), stacked scattered ion intensity versus energy data (b) and AES data of 4 ML cobalt on Pd {111}, annealed to 600 K before being sequentially exposed to H₂ at increasing pressure increments.

The scattering ion intensity versus scattering angle data (*figure 5.10*) do not indicate any apparent changes in the position of the blocking features. However, the definition, or depth, of the blocking channels decreases in the surface data. In particular the spectrum following exposure to H₂ at 10⁻⁶ mbar increases in absolute yield but the 87° and 90° channels (2 and 3 layer channels respectively) almost disappear. The absolute yields match the scattered ion intensity versus energy data as expected.

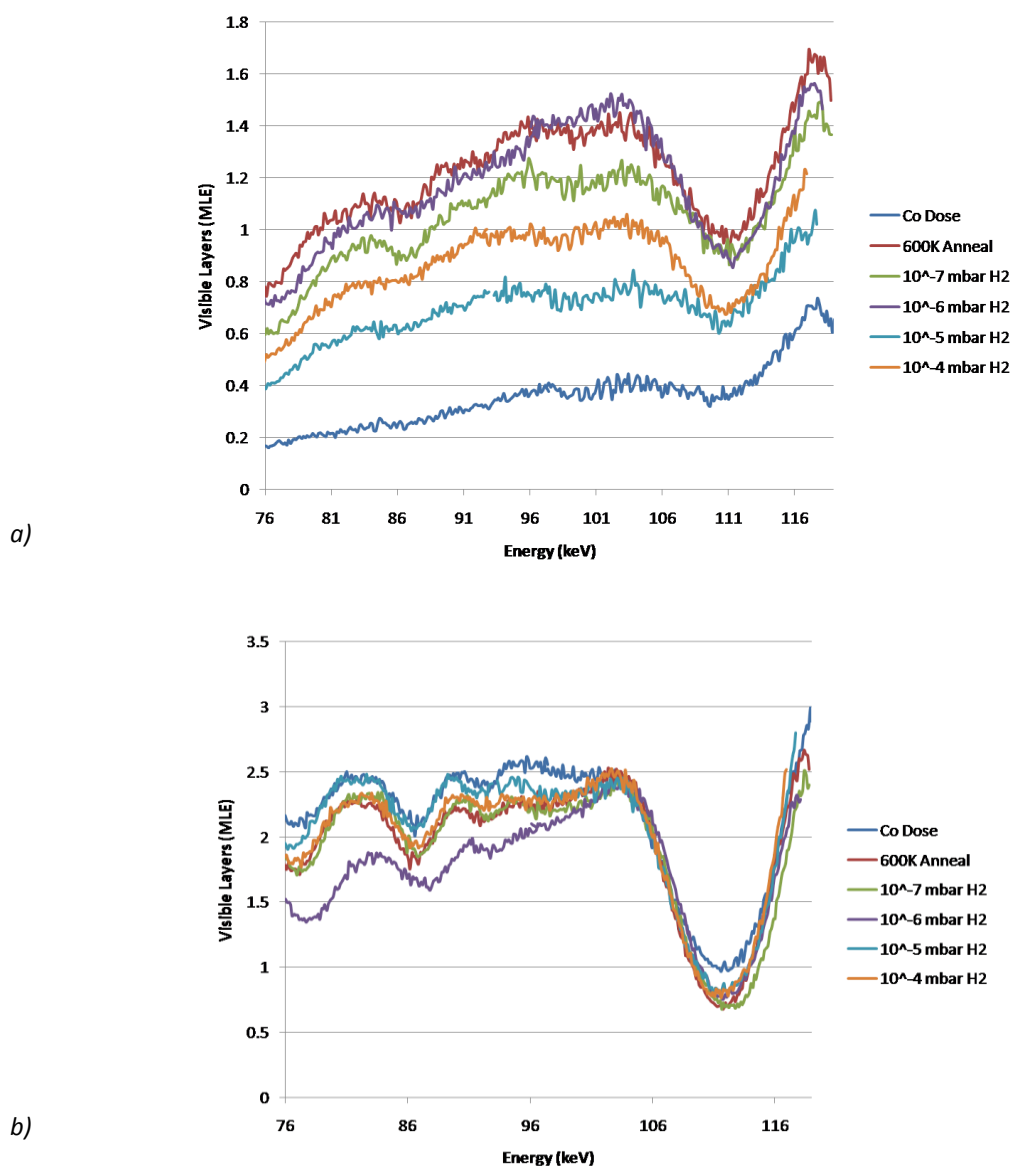


Figure 5.10:- Scattered ion intensity versus scattering angle data of 4 ML cobalt on Pd {111}, annealed to 600 K before being sequentially exposed to H₂ at increasing pressure increments. Data series correspond to the surface palladium peak (a) and the sub-surface palladium peak (b).

Pd Rich Alloy – Pre-Annealing at 700 K – H₂ Adsorption at 300 K

Figure 5.11 includes the 3-layer I vs. E MEIS spectra and the Pd surface compositions at each pressure for the adsorption of hydrogen on a Pd-rich CoPd alloy on Pd{111}. The amount of cobalt deposited prior to annealing was substantially lower than the previous experiments (approximately 1.2 MLE), however comparison with *Chapter 3* indicates that the alloy formed after annealing has approximately 85% palladium in each of the top three layers, so the experiment is comparable with other adsorption experiments.

The palladium surface data (*figure 5.12a*) essentially indicates very little change in the surface composition or structure. In the I vs. E data there are broad sub-surface features that marginally increase in intensity after treatment in H₂ at 10⁻⁶ and 10⁻⁴ mbar and there are also small changes in the Pd surface intensity. These changes are within the limits of the errors of the experiment.

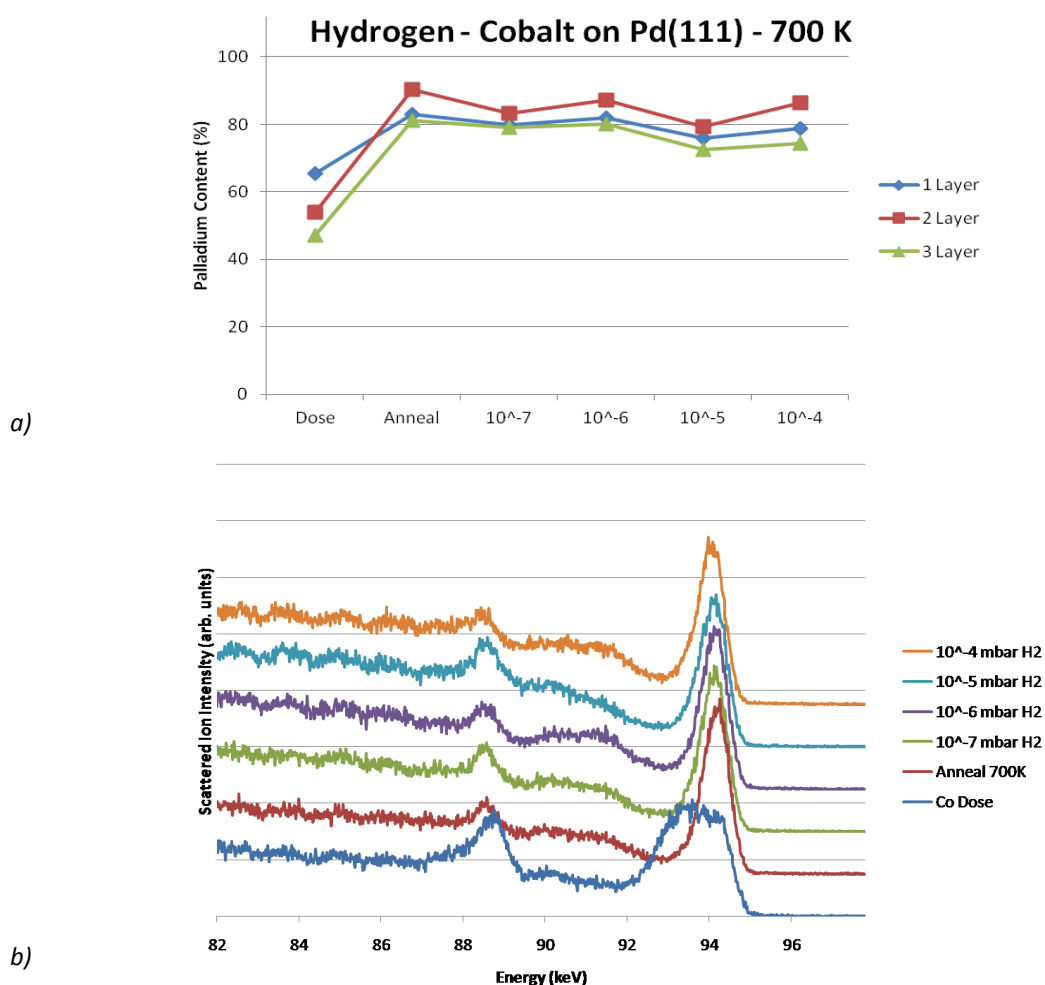
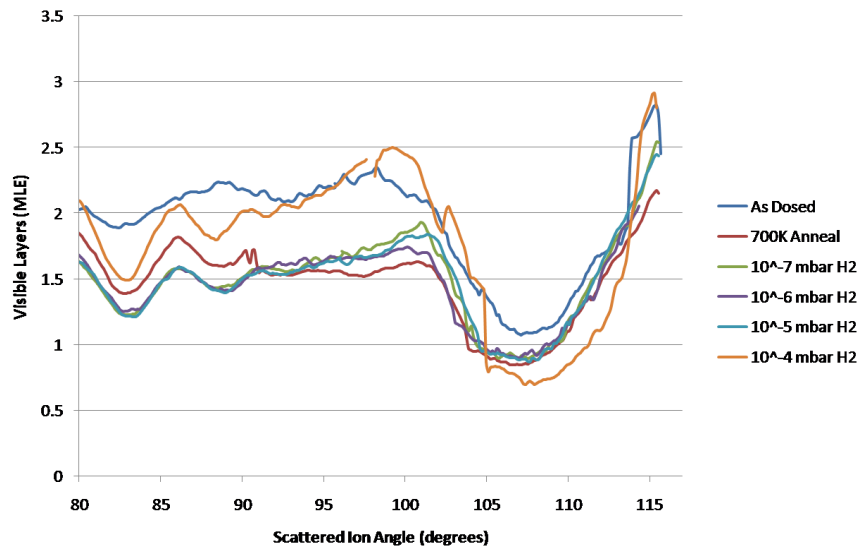
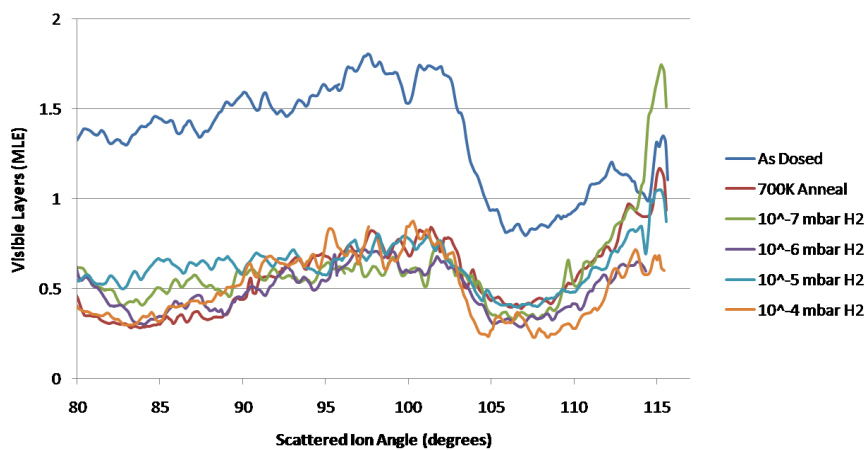


Figure 5.11:- Composition of the surface in Pd % (a) and stacked scattered ion intensity versus energy data (b) of 4 ML cobalt on Pd {111}, annealed to 700 K before being sequentially exposed to H₂ at increasing pressure increments.



a)



b)

Figure 5.12:- Scattered ion intensity versus scattering angle data of 4 ML cobalt on Pd {111}, annealed to 700 K before being sequentially exposed to H₂ at increasing pressure increments. Data series correspond to the surface palladium peak (a) and surface cobalt peak (b).

The I vs. θ data presented in figure 5.12 correspond to the IGOR fitted Pd peak (figure 5.12a) and fitted cobalt extracted from the Pd background signal. The yields of both spectra after annealing provide further evidence to indicate that the alloy formed is comparable to the experiment described in Chapter 3. The I vs. θ after H₂ exposure show relatively little variation with H₂ exposure and are thus consistent with the essentially unchanging I vs. E spectra displayed in figure 5.11.

Syngas Adsorption on CoPd Alloys on Pd{111} – MEIS

Co Rich Alloy – Pre-Annealing at 560 K – Syngas Adsorption at 300 K

The I vs. E MEIS data for Syngas adsorption at varying pressures on a CoPd alloy with a starting composition of around 45%, (corresponding to the low temperature limit of the ordered alloy regime) are given in figure 5.13. There is an indication that the lower pressure exposure to

syngas decreases the Pd content, but as the pressure is increased to 10^{-5} and 10^{-4} mbar, the Pd composition in the top three layers increases to a level higher than after the initial syngas treatment.

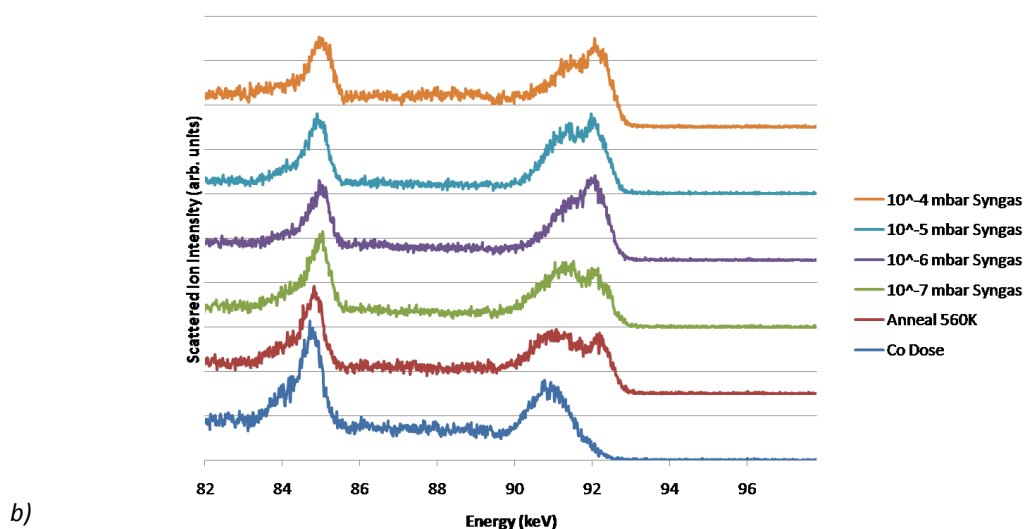
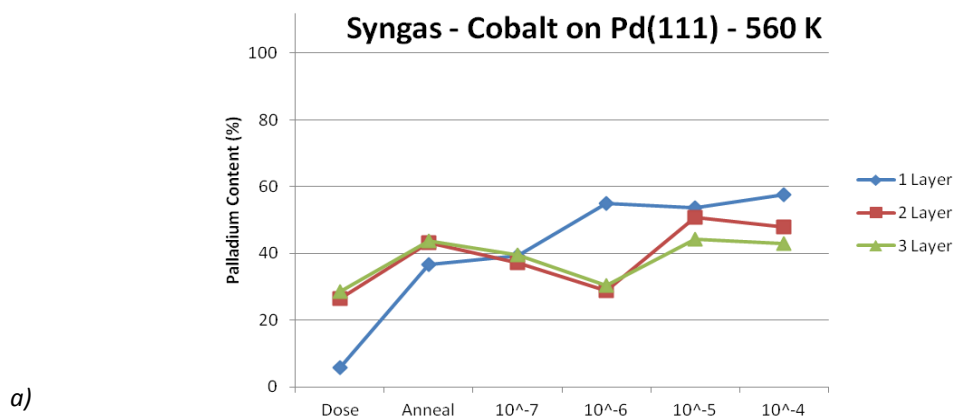
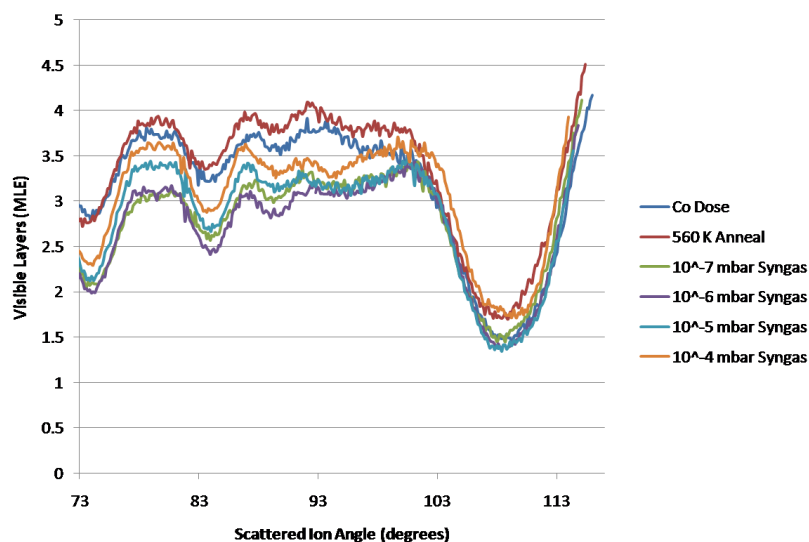
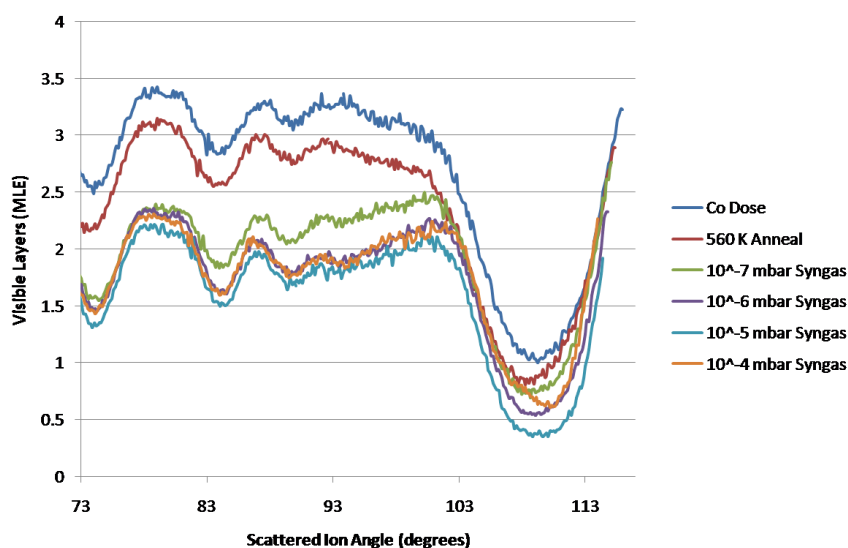


Figure 5.13:- Composition of the surface in Pd % (a) and stacked scattered ion intensity versus energy data (b) of 4 ML cobalt on Pd {111}, annealed to 560 K before being sequentially exposed to syngas at increasing pressure increments.

The changes in the I vs. θ MEIS data given in figure 5.14 augment the changes in the I vs. E MEIS data. In the surface peak data (figure 5.14a) baseline intensity decreases after the first syngas exposure at 10^{-7} mbar, then partially recovers as the pressure is increased. The total palladium spectra (figure 5.14c), indicate that the post-dosing and post annealing spectra are partially misaligned, as signified by a high background yield relative to the other spectra.



a)



b)

Figure 5.14:- Scattered ion intensity versus scattering angle data of 4 ML cobalt on Pd {111}, annealed to 560 K before being sequentially exposed to syngas at increasing pressure increments. Data series correspond to the surface palladium peak (a) and the sub-surface palladium peak (b).

Intermediate Composition Alloy – Pre-Annealing at 600 K – Syngas Adsorption

The I vs. θ MEIS data along with palladium compositions for a CoPd alloy, formed by annealing to 600 K is given in figure 5.15. The composition after annealing is approximately 45%, corresponding to the ordered alloy regime (Chapter 3). The palladium surface peak in the 1 layer data shows a slight increase in intensity from 10^{-7} to 10^{-4} mbar. In association with this the sub-surface peak shows some evidence of a decrease in Pd with increasing syngas partial pressure – but any effects are relatively minor.

The 2 and 3 layer data contain fluctuations in the Pd surface intensity with considerably less palladium indicated in the surface in the 10^{-7} and 10^{-5} mbar spectra – relative to the other spectra.

As before the differences in the Pd sub-surface are small, dropping intensity when the surface feature increases. Differences are also visible in the cobalt peak showing larger intensities when the palladium surface peak is reduced in intensity. It should be noted that the composition stays within a few percent of 50% Pd in all cases with the exception of the 10^{-5} spectra. In order to verify whether this effect was real, it would have been beneficial to repeat this experiment. Due to limited time at the MEIS facility, this was not possible.

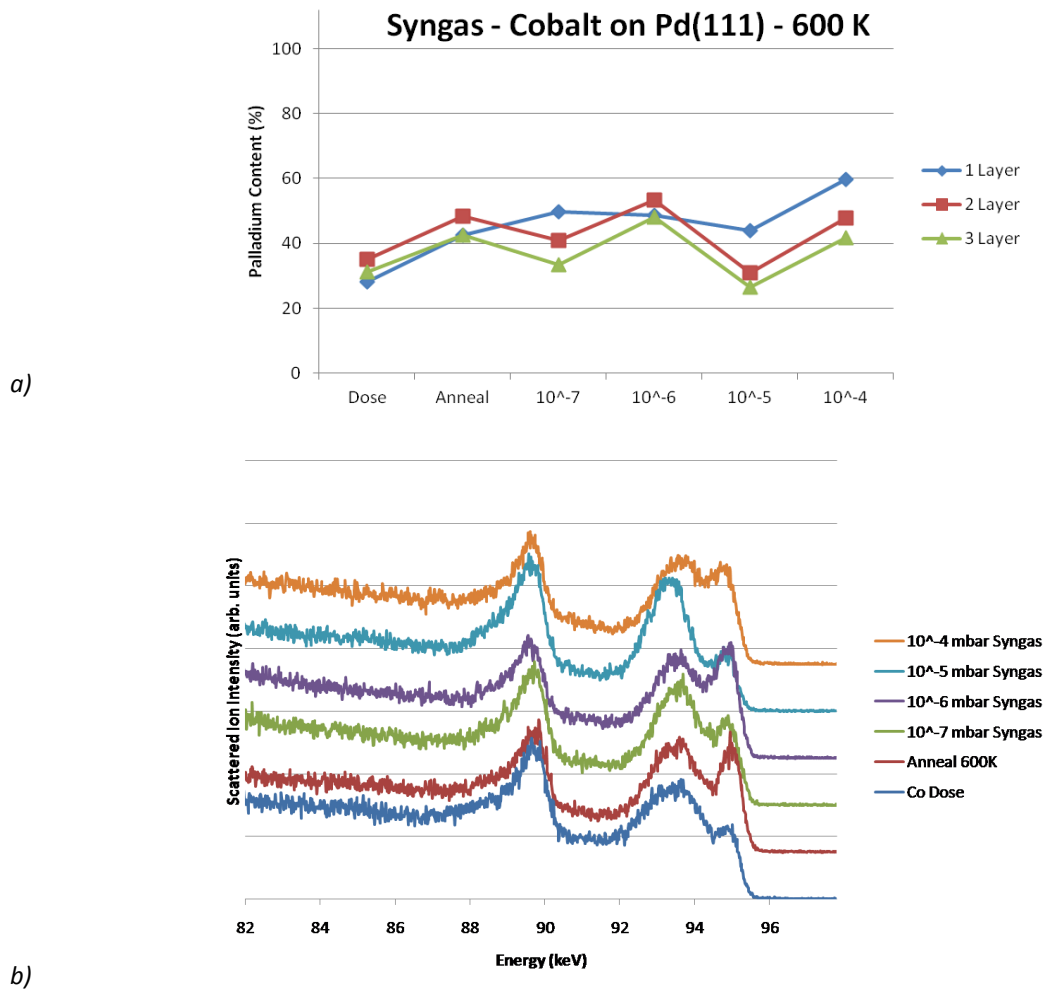


Figure 5.15:- Composition of the surface in Pd % (a) and stacked scattered ion intensity versus energy data (b) of 4 ML cobalt on Pd {111}, annealed to 600 K before being sequentially exposed to syngas at increasing pressure increments.

Figure 5.16 present the MEIS I vs. θ data for the syngas adsorption on a CoPd alloy surface with a Pd composition of 45-50%; corresponding to the ordered alloy regime described in Chapter 3. The scattered ion intensity versus scattering angle data for the 600 K alloy display relatively minor changes in absolute yield across all angles. In both of the surface and sub-surface peaks (as well as the total palladium) the spectra have a constant shape across the range of pressures.

The absolute yield in the total palladium data (figure 5.16c) remains constant and therefore yield increases in the surface spectra correspond to yield decreases in the sub-surface spectra. The 10^{-5} mbar surface spectrum is noticeable reduced relative to the other pressures, to a similar yield seen before the deposited layer is annealed. As described above, it was not possible to verify whether this unusual behaviour was reproducible.

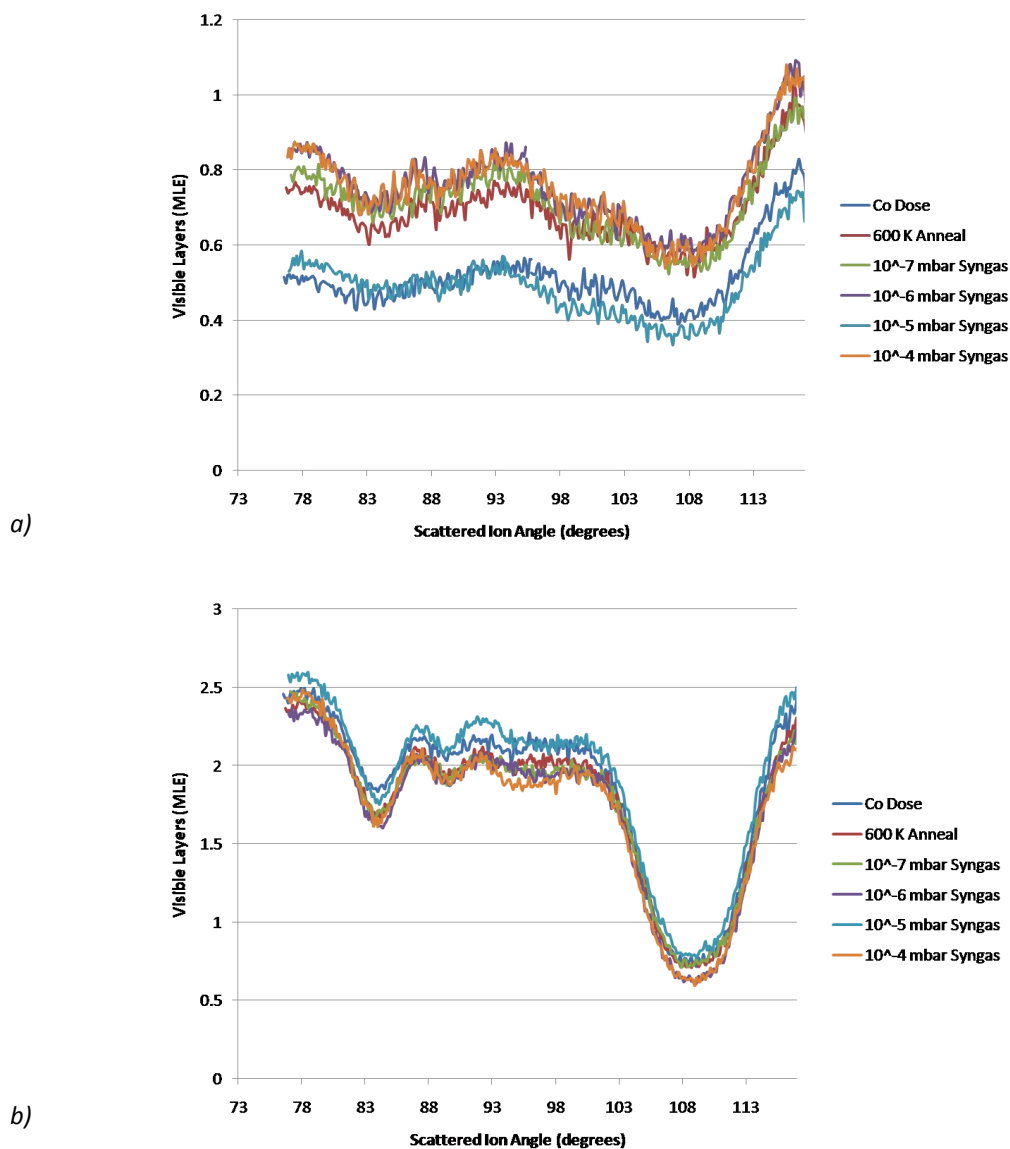


Figure 5.16:- Scattered ion intensity versus scattering angle data of 4 ML cobalt on Pd {111}, annealed to 600 K before being sequentially exposed to syngas at increasing pressure increments. Data series correspond to the surface palladium peak (a) and the sub-surface palladium peak (b).

Pd Rich Alloy – Pre-Annealing at 700 K – Syngas Adsorption

The I vs. E MEIS spectra for syngas adsorption at 300 K on a palladium rich bimetallic alloy on Pd{111} are presented in *figure 5.17* along with the palladium compositions. The alloy, formed by annealing to 700 K, corresponds to the surface composition of approximately 80%, consistent with the analogous annealing treatment reported in *Chapter 3*. There are few noticeable differences in the spectra after the surface is exposed to increasing pressures of syngas.

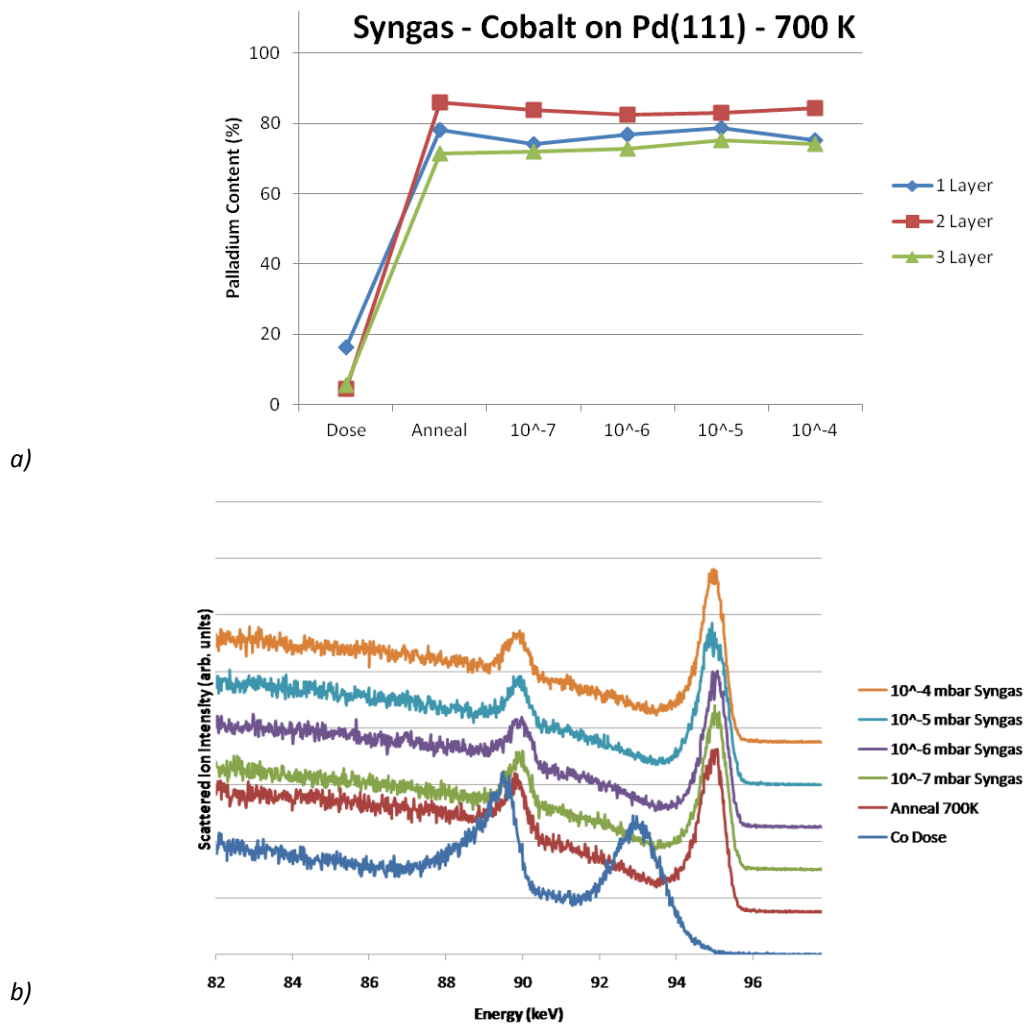
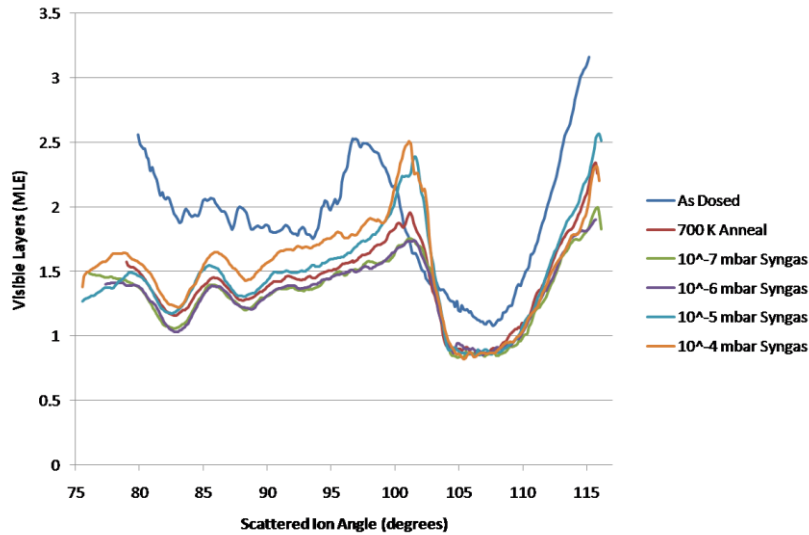
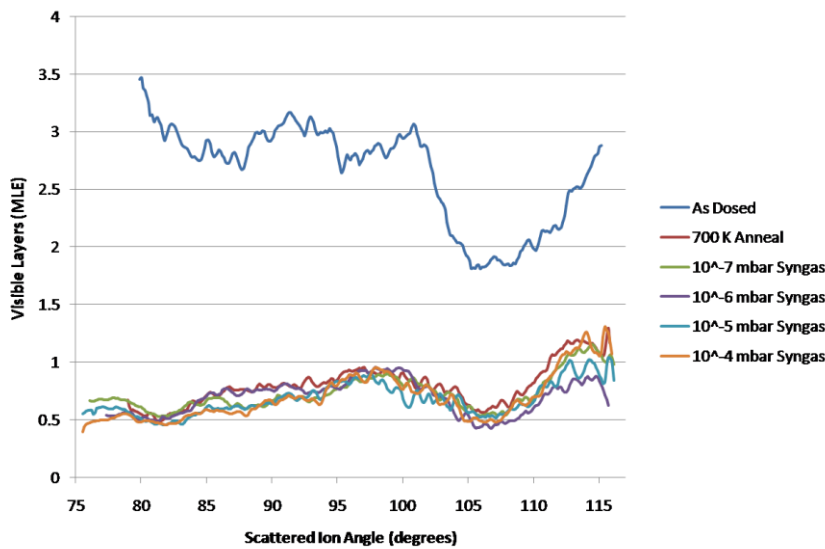


Figure 5.17:- Composition of the surface in Pd % (a) and stacked scattered ion intensity versus energy data (b) of 4 ML cobalt on Pd {111}, annealed to 700 K before being sequentially exposed to syngas at increasing pressure increments.



a)



b)

Figure 5.18:- Scattered ion intensity versus scattering angle data of 4 ML cobalt on Pd {111}, annealed to 700 K before being sequentially exposed to syngas at increasing pressure increments. Data series correspond to the palladium peak (a) and surface cobalt peak (b).

The scattered ion intensity versus scattering angle data for the cobalt rich alloy shows a substantial drop in the amount of cobalt and an increase in the blocking channel definitions. The post-dosing data series for palladium is relatively high in yield and the blocking channels are more diffuse. This data series corresponds to the sub-surface peak and is therefore not unusual. The post annealing and post syngas exposure data series have anomalous spikes on the low angle edge of the blocking channel at 109° due a difficulty encountered in the IGOR programme in identifying a sensible background subtraction in this region of the spectrum.

Carbon Monoxide Absorption on CoPd Alloys on Pd{111} – RAIRS

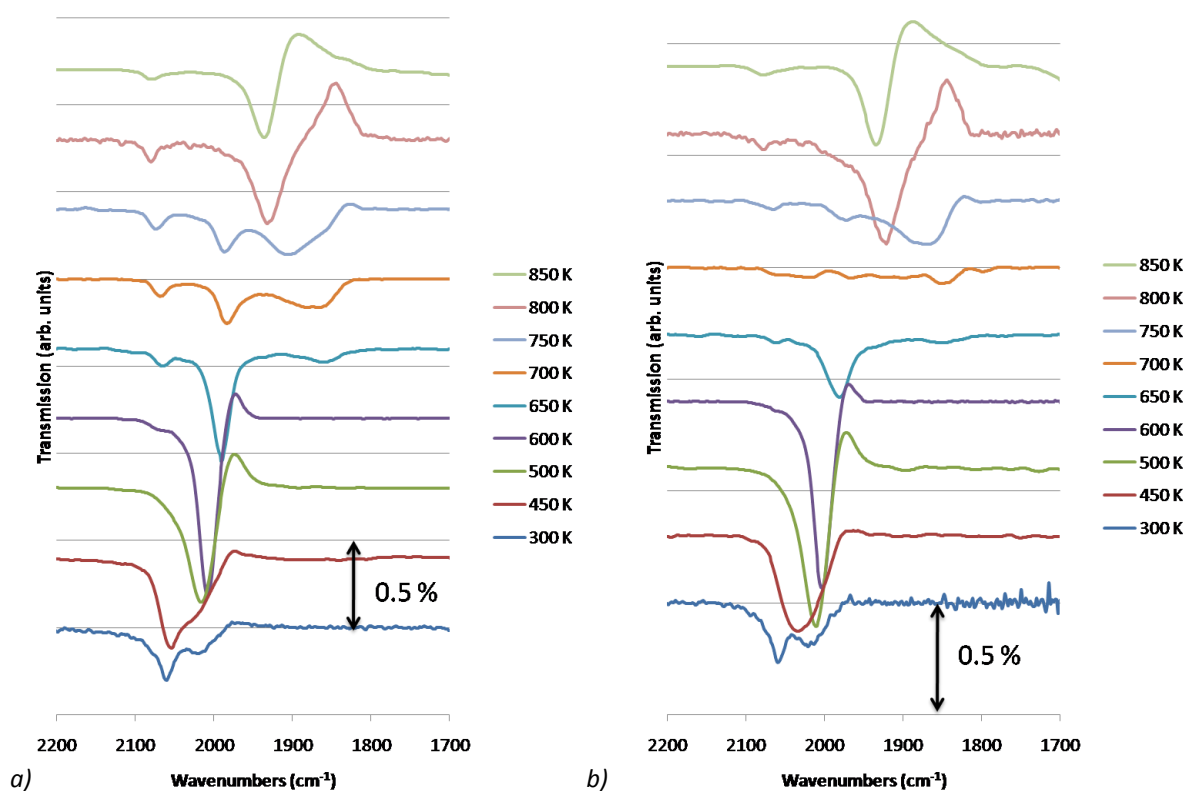


Figure 5.19:- Stacked RAIR spectra taken *in situ* during exposure (a) of CoPd alloys on Pd{111} to 10⁻⁷ mbar CO and post-exposure (b). Spectra correspond to the annealing temperatures used to create the alloy surface.

The RAIR spectra for a film of approximately 4 MLE cobalt on Pd{111} as a function of pre-annealing temperature are given in *figure 5.19*. The RAIR spectra shown are taken *in situ* during exposure to CO (*figure 5.19a*), and after the gas has been evacuated from the chamber (*figure 5.19b*) – the latter procedure of which is analogous to the sample preparation methods used in the MEIS experiments. In each case, spectra are presented relative to a background of the surface before exposure to any CO.

CO adsorption at 300 K on the sample following immediately after deposition of cobalt on Pd{111} gives rise to two peaks at 2015 and 2061 cm⁻¹ in the spectra acquired during the 10⁻⁷ mbar exposure. The 2061 cm⁻¹ peak is the larger of the two peaks with absorption of approximately 0.3%. The peaks remain unchanged at 10⁻⁶ mbar, and after the gas is removed at each of the exposures the intensity of the 2061 cm⁻¹ peak decreases.

Following annealing at 450 K, exposure to 10⁻⁷ mbar CO results in the peaks merging into a single feature at 2055 cm⁻¹ with a substantial shoulder. Evacuation of the gas results in the decrease of the high frequency side of the peak associated with a shift in the peak minimum to 2035 cm⁻¹.

Further annealing to 500 and 600 K gives rise to a single peak which shifts down to 2012 and 2006 cm^{-1} respectively. After the removal of the CO the peak intensity does not change noticeably, but it does shift down by approximately 5 cm^{-1} in each case. A small positive band is also observed at approximately 1970 cm^{-1} , indicative of the loss or displacement of a species present as a contaminant on the otherwise clean alloy surface.

The spectrum after annealing to 650 K presents three peaks consisting of one large peak (ca. 0.7% absorption) at 1985 cm^{-1} with two small features (<0.1% absorption) at either side; these are positioned at 2061 and 1868 cm^{-1} respectively. After removal of the CO the absorption decreases by 50% for all three peaks, along with a small shift of 15 cm^{-1} down in both the 1985 and the 1868 cm^{-1} peaks.

Upon annealing to 700 and 750 K the central peak loses intensity as the low frequency peak between 1850 and 1900 cm^{-1} gains intensity – clearly developing into at least two convoluted peaks. From 700 to 750 K the high frequency side of the double feature appreciably increases in intensity. The post evacuation spectra of these annealing temperatures exhibits the loss of almost all peak intensity except in the lower frequency portion of the double peak in the 750 K spectra where the peak remains relatively constant.

After annealing to 800 K the CO RAIRS spectra consist of one large peak at 1929 cm^{-1} and one large positive peak (indicating the loss of a CO species present in the background spectrum) at 1850 cm^{-1} . There is also a small peak at 2074 cm^{-1} , corresponding to the small high frequency peak in previous spectra. After evacuation of CO the peak intensities remain essentially constant and shift down by < 5 cm^{-1} .

The small high frequency peak partially decreases in intensity from the 800 K annealed surface to the 850 K annealed surface and the large positive peak shifts down and broadens. Post evacuation spectra indicate similar behaviour to the 800 K annealed surface: The peak intensity does not appear to change and there is a very small shift down in frequency of the main peak.

In *figure 5.20*, RAIR spectra are presented at each different pre-annealing temperature as a function of increasing CO pressure. It is apparent that the spectra (taken after evacuation of CO in all cases) remain essentially constant through 10^{-7} , 10^{-6} and 10^{-5} mbar.

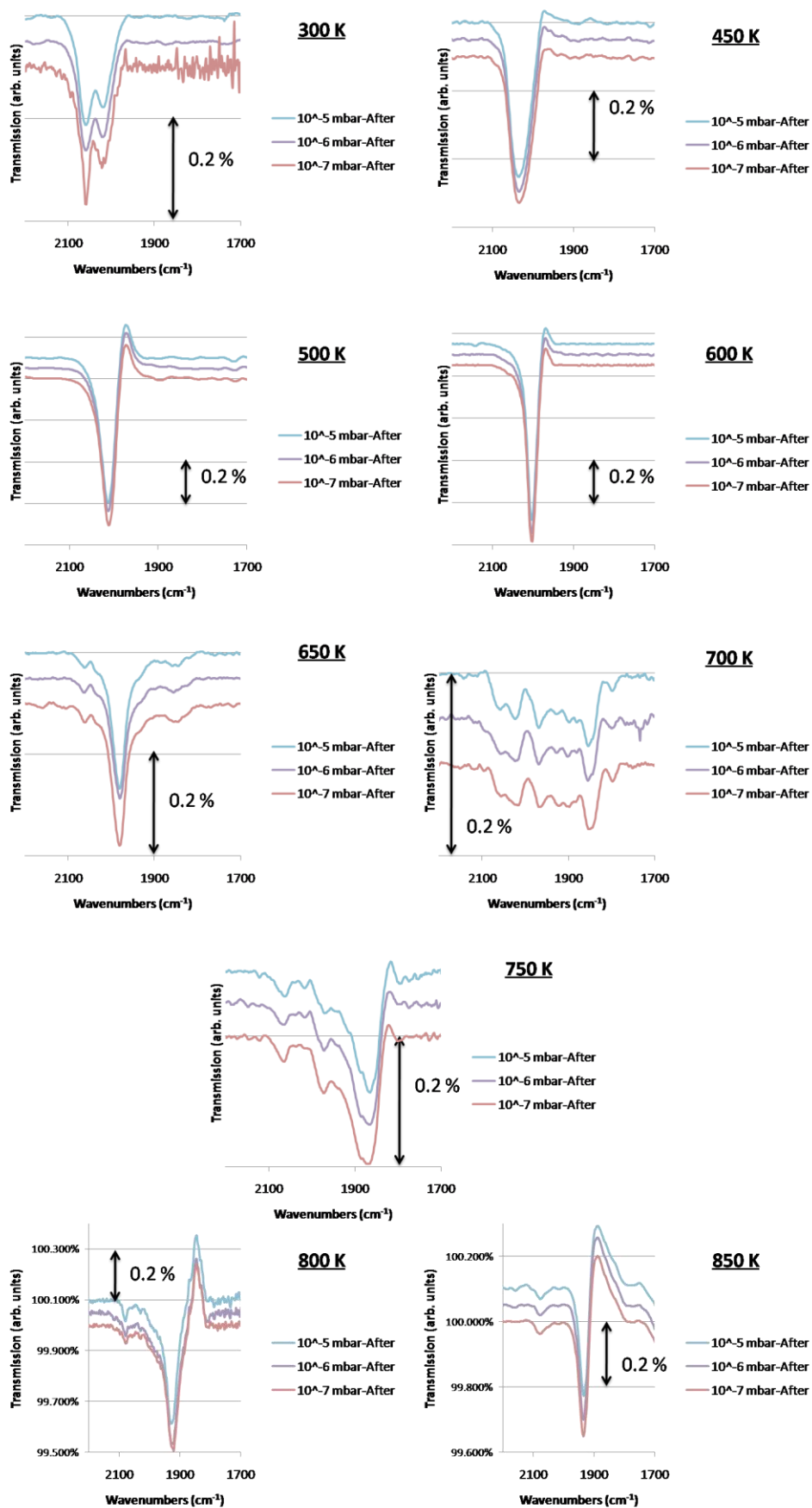


Figure 5.20:- RAIRS spectra taken after adsorption of CO at varying pressures on CoPd alloys pre-annealed to each of the temperatures indicated.

5.4 Discussion

The variability of the starting alloy composition, even though the same annealing conditions are maintained, indicates that the alloy formation is strongly coverage dependent and occurs relatively slowly. A small increase in the amount of deposited cobalt appears to result in a more cobalt rich surface after annealing to a given temperature. In contrast the alloy formed after annealing to 700 K or above appears to be largely independent of the initial coverage (above a certain limit). The rate of diffusion at the interface at elevated temperatures will be increased and therefore the independence of coverage above 700 K is not unexpected.

Carbon Monoxide Adsorption on CoPd Alloys on Pd{111}

The STM images presented in *Chapter 3* indicate a rough surface with island like morphology after cobalt dosing. With a comparison of published RAIRS data CO adsorption on the two different facets of cobalt [7-8], the RAIR spectrum in *figure 5.19* for the unannealed surface can be concluded to be in agreement with the surface appearance. The twin peak feature ($2015\text{-}2060\text{ cm}^{-1}$) is similar to the double peak seen on the high index surface of cobalt [8]. The alloy regime at the 600 and 650 K annealing temperatures (as read from the STM thermocouple) corresponds to the 560 to 600 K in the MEIS data.

As the surface is annealed in the STM/RAIRS apparatus through 450, 500 and 600 K the double peak is replaced by a single feature at 2010 cm^{-1} which is more in line with the close packed surface of Co{0001} [7]. Although the STM images do not show the islands flattening out, the changes do correspond to the associated MEIS data which indicated that the cobalt overlayer became more continuous after annealing to the lower temperatures. In this surface regime, evaluation of CO adsorption on cobalt in the literature [7] signifies the majority of the CO is adsorbed on atop sites.

CO adsorption on the cobalt rich alloy, prepared by annealing to 560 K, leads to strong segregation of Co to the surface at 10^{-7} mbar followed by no further changes in the spectra at higher CO partial pressures. The MEIS data reveal an absence of a Pd surface constituent. The surface therefore, becomes essentially 100% cobalt. The segregation of cobalt appears to occur in at least the top three layers – indicated by the low yield and the lack of blocking features in the surface scattering ion intensity versus scattering angle (*figure 5.4a*). The RAIRS data following adsorption of

CO under these conditions show a single peak at approximately 2000 cm^{-1} indicative of adsorption on Co sites with no evidence of adsorption on Pd-like sites. This suggests that exposure to CO at relatively low pressure is sufficient to redistribute the surface Co in such a way as to bury Pd several layers below the surface.

At intermediate annealing temperatures, the RAIR spectra evolve in a relatively complex way. In the RAIRS experiment, the CO RAIR spectra are relatively similar for the 650, 700 and 750 K annealing experiments; indicative that under these conditions the surface has a relatively stable composition. These spectra correspond to the STM images presented in *Chapter 3* that exhibit alternate rows of palladium and cobalt. On this surface there is in essence, a complete reduction in the number of the usual 3-fold Pd bonding sites [11] available to CO, and therefore adsorption would be expected only at atop or bridge sites. However, the bands between 1880 and 1900 cm^{-1} are more difficult to assign and may be related to CO adsorption in a 3-fold hollow site comprising of two Pd atoms and 1 Co atom for example. It is interesting to note that the RAIR spectra do not indicate any substantial pressure dependent changes on the CO adsorption. The subtle changes that are observed in the MEIS data, however suggest that MEIS is a more sensitive probe of such effects than RAIRS.

The thermodynamic properties of segregation, as discussed in *section 5.1*, suggest that the element with the strongest interaction with the adsorbate is most likely to accumulate at the surface. However, the rate of diffusion to the surface is likely to be strongly temperature dependent. It is not unexpected that CO adsorption gave rise to the most dramatic effects when the surface morphology was roughest. The existence of multiple edge and corner atoms presumably facilitates the redistribution of atoms by the adsorbate, thus explaining the wetting of the Pd substrate by CO on the Co-rich bimetallic surface.

At the highest annealing temperatures tested, the surface is extremely well defined as evidenced by STM (Moiré pattern with a periodicity of up to 15 nm is observed) and only minor changes are observed by MEIS. In the case of CO, the adsorption energy is relatively similar for Co{0001} [14] and Pd{111} [10] so dramatic segregation effects are not expected. However, the work of Chorkendorff and co-workers investigating CO adsorption on CuPt surfaces [20] showed that the surface composition can be dictated by additional factors such as the enthalpy of formation of an ordered alloy phase and the ability of CO to optimise the adsorption thermodynamics by adopting a particular adsorption site. Theoretical investigations examining the adsorption energy of CO on an

ordered p(2x1) surface in order to identify the optimum adsorption geometry of CO would be of great interest. It appears as though the alloy itself is stable under the influence of CO.

The alloy formed from annealing to 700 K in the MEIS apparatus corresponds to the CoPd alloy after annealing to 800 K in the STM/RAIRS apparatus. In this case, the RAIRS data show no pressure dependence, but the MEIS data indicated that above 10^{-6} mbar, the carbon monoxide causes significant cobalt segregation in the 700 K annealed alloy surface with the Pd composition in each of the top few layers dropping from 80% down to approximately 50%. The composition of the surface after 10^{-4} mbar CO is within the ordered alloy regime. This is unlikely to be significant for the case of CO because at the lower palladium composition the segregation favours cobalt. Such a relatively dramatic change in the surface composition would be expected to be mirrored by a change in the RAIR spectra. Further work would be required to explain this apparent inconsistency.

After annealing the surface to 800 and 850 K in the STM/RAIRS apparatus, the CO RAIR spectra become dominated by the single 1930 cm^{-1} peak consistent with bridge site adsorption typically observed on Pd{111} under analogous conditions [11]. This demonstrates that the surface is similar to the clean Pd{111} surface. The additional peak is from atop desorption on the small amount of cobalt remaining in the surface.

The large positive features in the various spectra are a result of substantial amount of CO adsorbed on the surface during the background spectra being displaced during the deliberate exposures to CO *via* a compression of the CO layer, a change in the local adsorption site and hence a shift in the band position for CO.

Hydrogen Adsorption on CoPd Alloys on Pd{111} – MEIS

The alloys formed after annealing in the hydrogen experiments closely match the corresponding annealing temperatures from *Chapter 3*. The 600 K anneal produces the 50-50 alloy and 700 K annealing results in the expected palladium rich surface.

Hydrogen causes segregation in the surface layer of the 600 K alloy generally favouring cobalt as the pressure is increased, although some fluctuations are observed. The fluctuations are based around the I vs. E spectra taken from the 106° data tile for the adsorption of hydrogen at 10^{-6} mbar. The 700 K annealed alloy appears relatively unaffected by the hydrogen exposure. The spectra remain unchanged until 10^{-5} mbar where the cobalt intensity increases then 10^{-4} mbar where

there is an increase in the palladium peak intensity and a noticeable shift down in the energy of the cobalt peak accompanied by peak intensity changes. Small changes in the spectra are not unexpected due to the small amount of cobalt remaining after annealing.

The main effects observed following hydrogen adsorption are changes in the Pd sub-surface peaks. The basis behind this can be hypothesised to be absorption of dissociated hydrogen into the palladium bulk, causing disruption to the crystal lattice. This does correspond to the absorption behaviour of hydrogen with palladium discussed in the literature [16]. Hydrogen that dissociates and is absorbed into the palladium bulk would be likely to 'push' the palladium atoms apart, thereby increasing visibility in the MEIS experiment. This effect would be exaggerated in the surface layers due to the additional freedom of movement associated with surface atoms.

Syngas Adsorption on CoPd Alloys on Pd{111} – MEIS

Annealing to 560 and 600 K closely reproduces the data given in *Chapter 3* that describe the 50-50 alloy regime. The spectra after annealing to each temperature are similar to each other indicating the same surface structure in both cases: A result of different amounts of deposited cobalt, as discussed above. As expected the 700 K annealing gives a palladium rich surface.

Exposure of syngas to the CoPd alloy on Pd{111} from annealing to 560 K initially results in apparent segregation of cobalt after exposure to 10^{-7} mbar. The decrease in palladium is small at this point and can be considered to be within the range of error. As the pressure is increased, the segregation marginally favours palladium as the palladium concentration increases after exposure to CO at 10^{-6} mbar. The segregation of palladium increases significantly after exposure to 10^{-5} and 10^{-4} mbar confirming a trend in the segregation.

It is interesting that there seems to be a marked difference between adsorption of CO (causing strong segregation) and adsorption of CO/H₂ (where the composition remains fairly constant) on similarly cobalt rich surfaces. This is true across the range of tested compositions. In the case of CO it can be hypothesised that the CoPd 50-50 surface alloy may be favoured by the adsorption of CO. It would be valuable to carry out an analogous RAIRS/STM experiment on syngas adsorption to compare to adsorption of CO in order to determine how hydrogen influences the CO spectra and the nature of the surface structures produced on the bimetallic surface.

5.5 Conclusions

The RAIRS investigation of CO adsorption correlates well to the literature and previous STM/MEIS analysis (*Chapter 3*). The as deposited cobalt surface is defined as defective and stepped in nature corresponding to an island type morphology. As the sample is heated the surface becomes more ordered and defects are quickly removed. Above 600 K the cobalt begins to alloy with the underlying palladium associated with the appearance of palladium type RAIRS peaks and a shifting down of the main cobalt band probably due to electronic interactions between Pd and Co. At the highest annealing temperatures examined, RAIRS suggests that the surface behaves similarly to Pd{111} [11].

MEIS investigations show that the adsorption of CO on the cobalt rich CoPd surface on a Pd{111} substrate results in strong initial segregation of cobalt to the surface. It is believed that it is likely that CO redistributes cobalt from island edges to more effectively wet the Pd surface. The dramatic change in surface composition occurs following exposure to CO at 10^{-7} mbar.

CO adsorption on more Pd-rich alloy surfaces appears to lead to segregation, favouring the formation of the ordered 50-50 CoPd alloy observed in *Chapter 3*. It may be that the enthalpy of formation of this alloy coupled with an optimisation of CO coverage and adsorption energy provide the thermodynamic driving force for the segregation. For the same reason it is determined that the alloy with a starting composition of around 50% is stable under exposure to CO.

For the case of hydrogen and syngas adsorption on cobalt palladium alloys, the segregation effects are relatively subtle. In the case of hydrogen, the effects seem to be more pronounced on the surface structure which is probably related to diffusion of hydrogen into the sub-surface. In the case of syngas, segregation effects are found to be relatively insignificant suggesting that the presence of hydrogen alters the behaviour observed following the adsorption of pure CO. On the basis of MEIS alone, it is difficult to explain why this is the case. Future RAIRS and STM studies of syngas adsorption on bimetallic CoPd surfaces would help to resolve this behaviour.

5.6 Bibliography

- [1] Baddeley C. J., *The Chemical Physics of Solid Surfaces, Volume 10: Surface Alloys and Alloy Surfaces*, Elsevier (2002), Chapter 14, 495-526, ISBN: 0 444 51152 0
- [2] Lahtinen J. *et al*, *Adsorption and structure dependent desorption of CO on Co(1000)*, Surf. Sci. 418 (1998), 502-510
- [3] Lahtinen J. *et al*, *LEED investigations on Co(0001): The ($\sqrt{3}\times\sqrt{3}$)R30°-CO overlayer*, Surf. Sci. 448 (2000), 269-278
- [4] Cabeza G. F. *et al*, *Adsorption of CO on Co(0001) and Pt-Co(0001) surfaces: an experimental and theoretical study*, Surf. Sci. 465 (2000) 286-300
- [5] Ramsvik T. *et al*, *Molecular vibrations in core-ionised CO adsorbed on Co(0001) and Rh(100)*, Surf. Sci. 492 (2001) 152-160
- [6] Ciobîcă I. M. *et al*, *Adsorbate induced reconstruction of cobalt surfaces*, Surf. Sci. 602 (2008) 17-27
- [7] Beitel G. A. *et al*, *Polarization modulation infrared reflection absorption spectroscopy of CO adsorption on Co(0001) under a high-pressure regime*, J. Phys. Chem. 100 (1996), 12494-12502
- [8] Toomes R. L. *et al*, *The adsorption of CO on Co{10-10}*, Surf. Sci. 349 (1996), 1-18
- [9] Surnev S. *et al*, *CO adsorption on Pd(111): a high-resolution core level photoemission and electron energy loss spectroscopy study*, Surf. Sci. 470 (2000) 171-185
- [10] Bradshaw A. M. *et al*, *The chemisorption of carbon monoxide on palladium single crystal surfaces: IR spectroscopic evidence for localised site adsorption*, Surf. Sci. 72 (1978) 513-535
- [11] Kuhn W. K. *et al*, *CO adsorption on Pd(111): The effects of temperature and pressure*, Surf. Sci. 274 (1992), L611-618
- [12] Matolinova I. *et al*, *Influence of Pd-Co bimetallic interaction on CO adsorption properties of Pd_xCo_{1-x} alloys: XPS, TPD and static SIMS studies*, Vacuum 71 (2003), 41-45
- [13] Miyawaki J. *et al*, *Structural study of Co/Pd(111) and CO/Co/Pd(111) by surface X-ray absorption fine structure spectroscopy*, Surf. Sci. 601 (2007), 95-103
- [14] Bridge M. E. *et al*, *Hydrogen chemisorption and the carbon monoxide-hydrogen interaction on cobalt (0001)*, J. Catal. 58 (1979), 28-33
- [15] Kolasinski K. W., *Surface Science: Foundations of Catalysis and Nanoscience*, Wiley (2002), ISBN 0-471-49245-0
- [16] Winkler A., *Adsorption, reaction and desorption of hydrogen on modified Pd(111) surfaces*, Appl. Surf. Sci. 256 (2009), 1114-1119
- [17] Kiskinova M. P. *et al*, *Adsorption and coadsorption of carbon monoxide and hydrogen on Pd(111)*, Surf. Sci. 123 (1982), 61-76
- [18] Krawczyk M., *Oxygen adsorption on binary Co₅₀Pd₅₀ alloy surfaces*, Vacuum 63 (2001), 23-27
- [19] Krawczyk M. *et al*, *Surface characterisation of cobalt-palladium alloys*, Appl. Surf. Sci. 235 (2004), 49-52
- [20] Andersson K. J., *et al*, *Adsorption-driven surface segregation of the less reactive alloy component*, J. Am. Chem. Soc. 131-6 (2009), 2404-2407

*Characterisation of Mixed Alumina-
Titania Model Supports*



6.1 Introduction

From the discussion in *Chapter 1* on the relevant literature it is known that the primary role of the oxide in catalysis, including Fischer-Tropsch, is to increase the active surface area of the catalyst in order to reduce the costs [1]. To achieve this, the oxide must be highly porous with a high surface area and the surface chemistry should ideally result in the metal particles having a high dispersion. A strong metal support interaction (SMSI) gives rise to highly dispersed particles [2], however if the interaction is too strong the metal can react chemically with the oxide [3], resulting in an inactive surface. This chapter will discuss work on model oxide films and the influence on the metal particles supported by these films.

Oxides used as catalyst supports are generally thermally stable, relatively inert and inexpensive. As discussed in *Chapters 1 and 2*, many oxides are also strong electrical insulators limiting extensive surface science analysis on the surface of oxides. The surface chemistry can be closely reproduced by creating a thin film of oxide on a conducting substrate [4-6]. Important features of this chemistry include the surface structure as well as the nature of the surface termination. These surface characteristics then directly influence the wetting properties and therefore the particle sizes and structure. An extension of this is the defect density and porosity of the surface which also subsequently affect the supported particles.

Aluminium oxide, or sapphire, is an insulating material and prohibits the use of many surface analysis techniques. A comprehensive review of surface examinations using model alumina supports is given by Baumer *et al* [4]. Several preparations on different metal substrates are discussed, along with the surface characterisation techniques commonly employed in the analysis of the alumina thin films. The most desirable alumina thin film exhibits a highly regular ultra thin oxide layer of thickness 5.35 Å [5] on the (110) surface of a nickel aluminium alloy.

The deposition of several metals is also discussed by Baumer *et al* [4], including cobalt and palladium. The nucleation and growth of the two metals on the oxide is relatively dissimilar – cobalt nucleation is highly heterogeneous occurring at point defects and the resulting dispersion is high, while palladium wets the surface easily and growth follows the vectors of the oxide substrate. Deposition of cobalt at an elevated temperature (573 K) results in the rapid aggregation of the deposited material. The difference between each of these metals is an important consideration, and

the rapid coalescence of the cobalt indicates a low SMSI and has consequences for the surface area of catalysts of this type.

The conclusion made by Khassin *et al* [2] contradicts the low SMSI discussed above. The authors examine co-precipitated cobalt-alumina catalysts and the XPS results indicate that the cobalt does not fully reduce at relatively high calcining temperatures. The results do not differentiate whether the remaining cobalt exists as cobalt oxide or cobalt aluminate. The explanation for the varying interpretations is likely to be the differing methods of preparation.

Another important consideration of alumina type supports is that although oxidation with deposited metals occurs at room temperature, the oxidation is shown to only occur at the interface [3]. This conclusion applies to single crystal alumina and ultra thin films of alumina. It is important to note that cobalt deposition in this study compared to catalytic studies is *via* metal vapour deposition as opposed to reduction from an oxide. Metal particle encapsulation by the oxide on NiAl(110) does not appear to occur below 900 K and on Al(111) supported oxides [3].

Titania single crystals are conducting (as discussed in *Chapter 1*) and they are therefore used directly as the support. The surface chemistry of titania has been reviewed [6]. This includes discussion on the surface structure and defect chemistry, along with reconstructions of various facets of rutile titania (the most common form of titania). Additionally the depositions of several different metals have been discussed – cobalt and palladium are among the metals covered.

The deposition of cobalt on titania has been shown to result in the formation of cobalt titanates [7]. Titania supported cobalt has also been analysed by Suriye and co-workers [8] focusing on the oxidation state of the titania and the effects on the cobalt catalyst. FT-IR, TPD and reaction tests were used to characterise the catalyst. Importantly the formation of cobalt titanates is more prevalent on titanium with many oxygen vacancies (associated with Ti^{4+} being replaced by Ti^{3+}). An improved understanding of this system would be obtained by structural characterisation using ion scattering and correlating this to the oxidation states, examined using photoemission techniques. Another consideration is that the use of promoters may inhibit the formation of cobalt titanates and thus prevent deactivation.

A comparative study of cobalt supported on alumina, silica and titania has been performed using transmission electron microscopy with elemental analysis and XPS [9]. The pore sizes of each

of the oxides are shown to have a large contribution to the morphology and particle size of the deposited cobalt as opposed to the chemistry of the oxides. The small pores in the silica and γ -alumina supports give rise to a high dispersion of smaller particles, whereas the large pores in the titania and α -alumina result in large agglomerates of Co_3O_4 .

The growth of epitaxial titanium dioxide films has been carried out on a sapphire substrate [10]. The titania grown exhibits the rutile structure with a relatively high defect density. AFM analysis shows the surface to have a polycrystalline appearance, but LEED analysis indicates highly ordered crystallites. Although the growth rate of titania is shown to be independent of the oxygen partial pressure, the morphology changes from highly angular crystallites at 5×10^{-7} torr to rounded crystallites at 1×10^{-5} torr.

Cobalt supported by alumina doped with silica was compared to cobalt supported by alumina [11]. In accordance with the previous comparison of the cobalt morphology on the different oxides [9], the authors conclude that the dispersion and morphology are highly dependent on the pore sizes. The relatively low amount of silica doping (*ca.* 5%) was shown to improve the reaction rates for Fischer-Tropsch Synthesis, and this was attributed to improved reducibility due to a reduction in the SMSI. The authors suggest that formation of cobalt aluminate was reduced in the silica-doped sample, however cobalt aluminate would be difficult to resolve separately from cobalt oxide in the XPS data. Energy dispersive x-ray spectroscopy could point towards cobalt aluminate, but the results from this technique were not been included in this case.

Mixed silica-titania supported cobalt was examined through CO hydrogenation by Jongsomjit *et al* [12]. The samples were also characterised using XRD, Raman spectroscopy, scanning electron microscopy/energy dispersive x-ray spectroscopy (SEM/EDX) transmission electron microscopy (TEM) temperature programmed reduction (TPR) and H_2 chemisorption. The overall conclusions include a large reduction in activity of the mixed oxide supported cobalt than silica supported cobalt; however the selectivity towards higher hydrocarbons was indicated for increased titania content in the support. The cause of the lowered activities can be hypothesised to be the result of formation of cobalt titanate, while the improved selectivities could be an indicator that the titania has role in chain growth – either through reservoir effects or metal-oxide boundary adsorption site contribution.

The aims of this chapter are to study the structure and composition of model mixed oxide surfaces grown on NiAl{110} using MEIS, and to examine the growth and thermal stability of cobalt nanoparticles on these surfaces using TPD.

6.2 Experimental

A widely employed method (for example, refs [4-5]) used to create an ultra thin oxide layer of alumina is to use a nickel aluminium alloy single crystal, typically NiAl{110}. Sputtering with argon ion energies of *ca.* 1.5 keV for 20 minutes followed by annealing to 750 °C is optimum for stripping layers of atoms without excessively damaging the planar structure. The crystal, heated to 300 °C, is subsequently exposed to oxygen at 10^{-6} mbar for 20 minutes. The resulting oxide layer is 2 layers thick or ≈ 5.35 Å [5].

The NiAl{110} crystal [Surface Preparation Laboratories] used for the alumina surface, as detailed above, is used as the support for the mixed oxide compositions to maintain continuity. The titania surface and $\text{Al}_x\text{Ti}_y\text{O}_z$ surfaces are created by dosing pure metal titanium from a filament in varying quantities and oxidised according to the preparation of the alumina surface.

During all MEIS data collection, the crystal was in an aligned geometry along the [1-12] azimuth with the beam incident along the [-1-2-1] direction which corresponds to an illumination of the top three layers of an ideal fcc {111} surface. The detector was set at two different scattering angles of 70° and 90°.

In the TPD apparatus, cleaning is followed by cobalt dosing using the miniature furnace in different quantities ranging from 0.5 MLE (monolayer equivalents) to 4 MLE. The sample is then annealed to one of the temperatures for five minutes and allowed to cool to room temperature. The surface is exposed to approximately 60 L of carbon monoxide (300 s, 1.3×10^{-7} mbar), measured indirectly from the ion gauge, and confirmed directly from the quadrupole mass spectrometer (MKS Spectra; 0-300 a.m.u.).

Immediately after the CO partial pressure reading has returned to background after dosing the TPD is started. The 'Spectra' programme controlling the mass spectrometer records pressure data every second for each mass/charge value chosen while the computer separately records the temperature values from the thermocouple. Subsequently the two data sets are synchronised by starting the temperature recording after the pressure measurements have been taken for five seconds and waiting a further five seconds until the heating is started.

The sample, mounted on tungsten wire, is heated resistively using a fixed current. This initially gives a linear heating rate which drops off at higher temperatures. The current is therefore chosen to give a linear heating rate across a temperature range that includes all expected notable desorption features.

As well as measuring the mass/charge value of 28, corresponding to CO, values of 2 (pH_2), 18 (H_2O) and 44 (CO_2) were also routinely recorded when using CO as the molecular probe. Care was taken as to not confuse CO with other mass fragments with a mass/charge value of 28, most notably diatomic nitrogen. This was achieved by monitoring the peak during cleaning, valve operation and other equipment use to ensure that the background remains constant.

6.3 Results

Titanium Oxide – NiAl{110} – Medium Energy Ion Scattering

The amount of titanium deposited onto the NiAl{110} substrate is estimated from the attenuation of the Ni-848 eV Auger peak giving a film thickness of 16 Å. If the titanium growth was pseudomorphic this would correspond to approximately 5.5 ML of metallic titanium.

Medium energy ion scattering characterisation of the model titanium oxide support on the NiAl{110} substrate is shown in *figure 6.1*. These spectra correspond to the 1 layer blocking channel at a scattering angle of 90°. The MEIS scattering ion intensity versus energy spectra of the clean NiAl{110} crystal contains a small peak at 76 keV identified as aluminium, and a larger peak at 89 keV corresponding to nickel. After dosing 8 ML titanium a double feature is observed between 84-88 keV whilst the peaks corresponding to the clean NiAl{110} lose intensity and become difficult to distinguish from the background noise. In addition a sharp peak at 90 keV separate from the peak ending at 88 keV is visible.

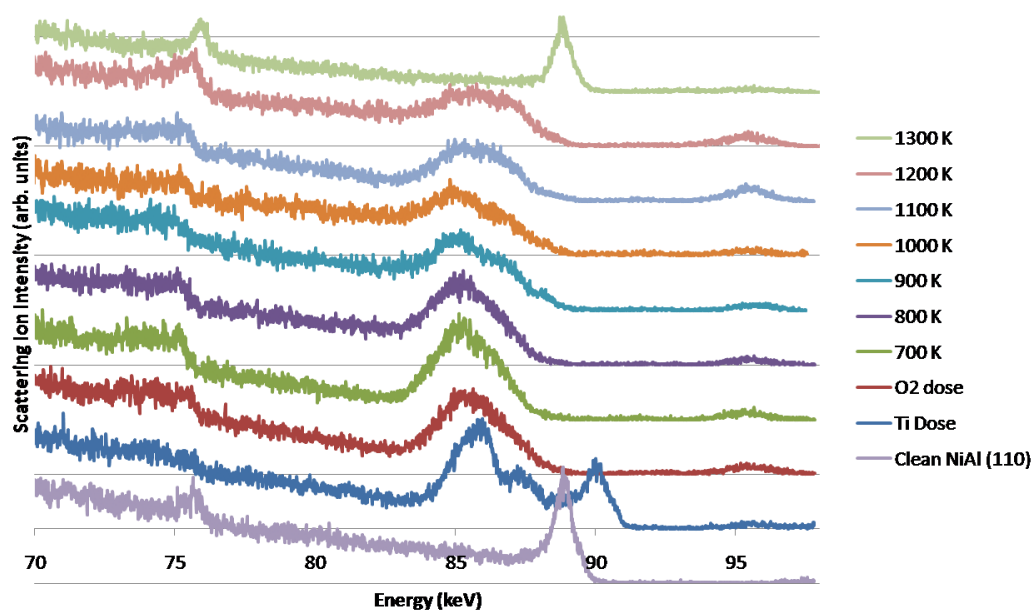


Figure 6.1:- Stacked scattered ion intensity versus energy MEIS data of 8 ML titanium on NiAl{110}, oxidised and sequentially annealed to increasing temperatures.

Following oxidation the peak between 84-88 keV changes to a single asymmetric feature and the peak at 90 keV disappears. At the same time a peak returns at 76 keV with the inclusion of a broad shoulder feature on the low energy side of the peak. As the substrate is annealed through 700 and 800 K the lower energy peak (76 keV) increases slightly in intensity and becomes sharper. The higher energy edge and the maximum of the peak complex between 84-88 keV shifts down in energy, however the low energy edge does not move from 84 keV.

As the sample is annealed past 900 K the spectra do not change drastically. The 86 keV peak exhibits the only notable changes as the peak appears to broaden. After 1200 K the peak is broader than at any of the lower temperatures. Annealing to 1300 K results in a transformation in the spectrum with it ending up similar to the clean NiAl{110} surface.

Cobalt Nanoparticles on Alumina on NiAl{110} – CO TPD

The CO desorption spectra (*figure 6.2*) from cobalt supported on alumina consists of a single peak around 380 K. There are no significant changes in the position of this peak; however the height of the peak does increase for the surface that was annealed to 400 K, followed by a decrease for the 560 K annealed surface. The remainder of the spectrum, up to 700 K, indicates no further desorption from the surface.

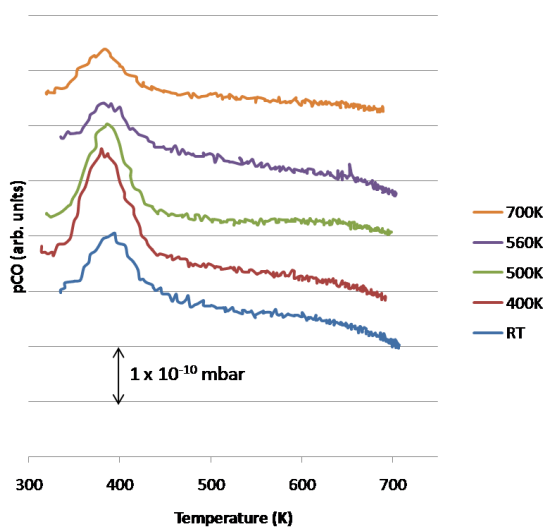


Figure 6.2:- Stacked CO-TPD spectra of 1 MLE cobalt on an alumina film on NiAl{110}. Each spectrum corresponds to a range of post cobalt dose annealing temperatures.

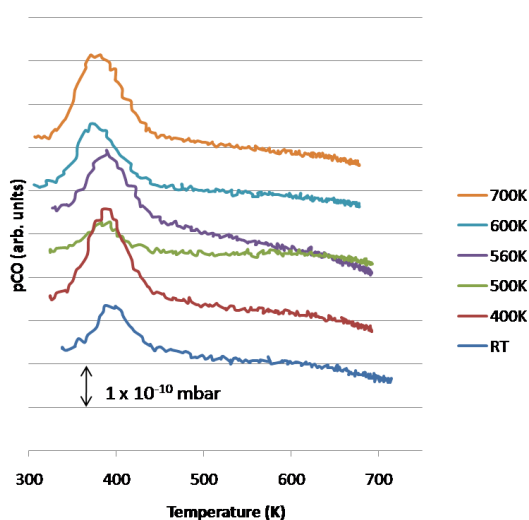


Figure 6.3:- Stacked CO-TPD spectra of 2 MLE cobalt on an alumina film on NiAl{110}. Each spectrum corresponds to a range of post cobalt dose annealing temperatures.

The CO desorption from the 2 MLE cobalt/alumina surface also exhibits a peak around 380 K. The peak intensity drops through the spectra for the 500 K annealed surface, but the higher temperature spectra of 600 and 700 K show a similar desorption feature to the 400 K spectra. The higher temperature portions of the spectra remain unchanged from the 1 MLE cobalt spectra, displaying no further desorption above 450 K.

4 MLE of cobalt (*figure 6.4*) on alumina demonstrates consistent CO desorption across the range of annealing temperatures. The peak at 380 K does not appear to change in intensity at higher annealing temperatures, and the small shift down in the CO desorption peak in the 400 K anneal spectrum is within the error range and therefore appears insignificant.

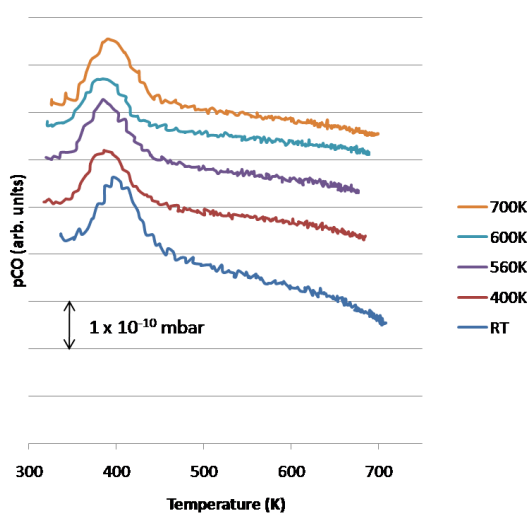


Figure 6.4:- Stacked CO-TPD spectra of 4 MLE cobalt on an alumina film on NiAl{110}. Each spectrum corresponds to a range of post cobalt dose annealing temperatures.

Comparison of the three coverages of cobalt indicates only small differences in the spectra. The spectra corresponding to desorption from the surface before any annealing show comparable relative desorption at all three coverages indicating a similar number of active bonding sites.

Mixed Oxide (Low Titanium Content) – NiAl{110} – TPD

Low titanium content refers to the surface preparation discussed in *section 6.2* following deposition of 0.5 ML of titanium metal. The composition of this mixed oxide is to be determined quantitatively by combining the TPD experiments with the use of another technique such as XPS.

The CO desorption data (*figure 6.5*) for the 0.5 MLE cobalt on the low titanium mixed oxide surface consist of two peaks, one sharp peak around 380 K and a very broad high temperature feature. The high temperature feature in the unannealed spectra begins just above 510 K, peaks

around 680 K and drops away towards the end of the spectrum at 900 K. After annealing to 400 K the high temperature peak appears absent although the baseline pressure does diminish towards the end of the spectrum. The high temperature peak is apparent in the spectra when the sample is annealed to 500, 560 and 600 K – The peak is centred at 640 K for the surface that was annealed to 500 K and shifts up to 670 and 710 K for the 560 and 600 K annealing temperatures respectively.

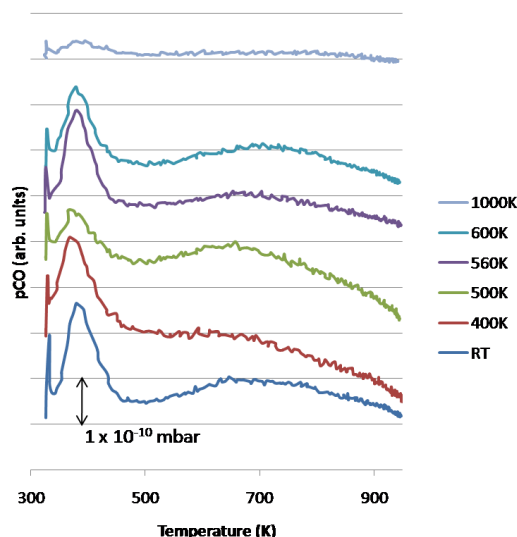


Figure 6.5:- Stacked CO-TPD spectra of 0.5 MLE cobalt on a mixed oxide film (0.5 ML titanium deposited followed by oxidation) on NiAl{110}. Each spectrum corresponds to a range of post cobalt dose annealing temperatures.

1 MLE cobalt (figure 6.6) on the mixed oxide (low titanium content) gives rise to similar peaks at each of the annealing temperature spectra. There is one peak at 380 K and a higher temperature peak that shifts down in the spectrum for the surface pre-annealed to 500 K, then back up in the 600 K pre-anneal spectrum. The peak intensities overall are increased in comparison with the 0.5 MLE cobalt on mixed oxide (low titanium content) experiments.

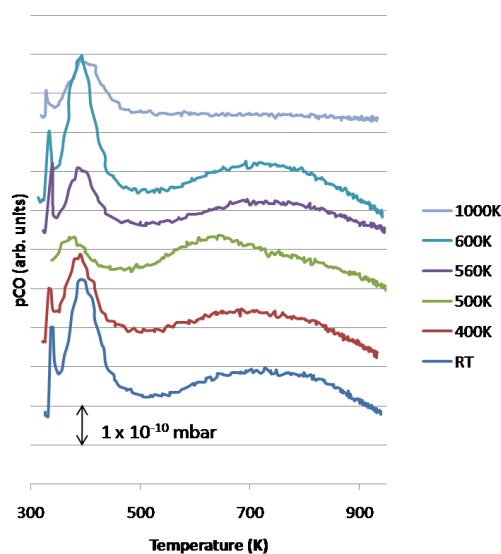


Figure 6.6:- Stacked CO-TPD spectra of 1 MLE cobalt on a mixed oxide film (0.5 ML titanium deposited followed by oxidation) on NiAl{110}. Each spectrum corresponds to a range of post cobalt dose annealing temperatures.

The peak intensities in *figure 6.7* for the 380 K peak increase further still for 3 MLE of cobalt on the same oxide composition. At the same time the high temperature feature appears to have a drop in intensity relative to the main peak. The absolute intensity of this peak does drop, however due to the broad nature of this feature it is difficult to judge the magnitude of the peak accurately for each cobalt coverage.

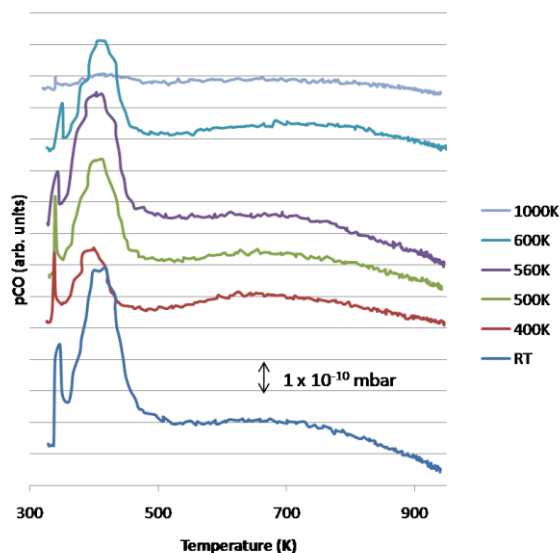


Figure 6.7:- Stacked CO-TPD spectra of 3 MLE cobalt on a mixed oxide film (0.5 ML titanium deposited followed by oxidation) on NiAl{110}. Each spectrum corresponds to a range of post cobalt dose annealing temperatures.

Mixed Oxide (Increased Titanium Content) – NiAl{110} – TPD

Increased titanium content refers to the surface preparation discussed in *section 6.2* following deposition of 1.3 MLE of titanium metal. The composition of this mixed oxide is to be determined quantitatively by combining the TPD experiments with the use of another technique such as XPS.

After deposition of 1 MLE cobalt (*figure 6.8*) onto the mixed oxide surface with increased titanium content the spectra remains similar to the 1 MLE cobalt on the low titanium content mixed oxide. The 380 K peak drops slightly in intensity and the high temperature peak appears to increase slightly upon annealing to 400 K, but the peak positions remain constant. The 380 K peak remains in the 560 K anneal spectra with a very low intensity high temperature peak.

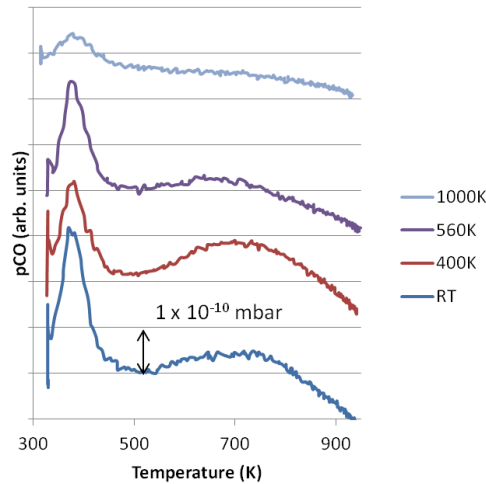


Figure 6.8:- Stacked CO-TPD spectra of 1 MLE cobalt on a mixed oxide film (1.3 ML titanium deposited followed by oxidation) on NiAl{110}. Each spectrum corresponds to a range of post cobalt dose annealing temperatures.

The higher cobalt coverage gives rise to consistent spectra across the range of pre-annealing temperatures as indicated in figure 6.9. The 380 K peak drops initially in the 400 K anneal spectrum, increases again in the 600 K spectrum and following the previous trend of dropping significantly after annealing to 1000 K. Compared to the previous oxide compositions/cobalt coverages, the high temperature feature is down around 615 K (it has generally been above 700 K in prior experiments). The intensity of this peak is has also comparatively increased from the other coverages/compositions.

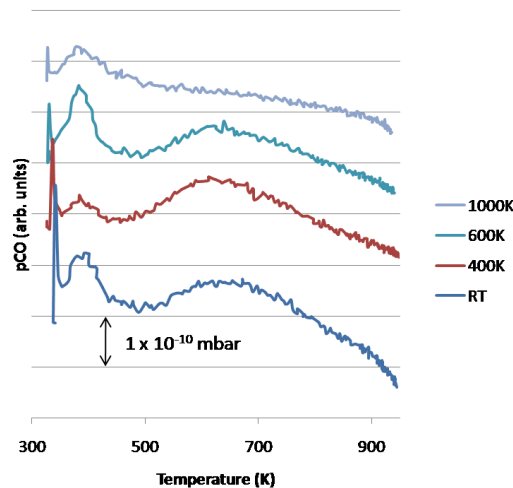


Figure 6.9:- Stacked CO-TPD spectra of 3 MLE cobalt on a mixed oxide film (1.3 ML titanium deposited followed by oxidation) on NiAl{110}. Each spectrum corresponds to a range of post cobalt dose annealing temperatures.

Titanium Oxide (Thick Titanium Layer) – NiAl{110} – TPD

The thick titanium layer refers to the surface preparation discussed in section 6.2 following deposition of 8 ML of titanium metal with the intent of producing an unmixed titania thin film. The

composition of this thin film is to be determined quantitatively by combining the TPD experiments with the use of another technique such as XPS.

Cobalt (1 MLE) supported by titania grown on NiAl{110} exhibits two desorption features as indicated in *figure 6.10*, a sharp peak at 380 K and a broad asymmetric peak with a base starting just above 500 K and continuing to the end of the spectra at 950 K. The intensity of the peak at 380 K drops substantially after annealing (although after annealing the sample to 700 K the intensity is high). As the sample is annealed the shape of the high temperature peak changes, associated with shifts in the maximum desorption temperature of this peak. Initially this peak is symmetrical and low in intensity. After annealing to 400 and 500 K the peak increases in intensity without substantially shifting. As the sample is annealed between 560 and 700 K the high temperature peak shifts down to 611 K then up to 815 K while the base of the peak remains fairly constant.

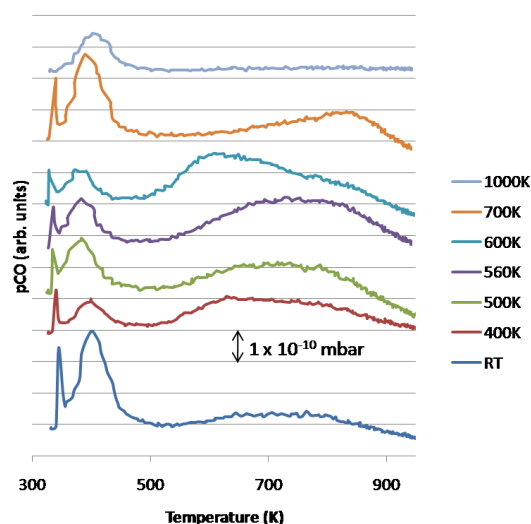


Figure 6.10:- Stacked CO-TPD spectra of 1 MLE cobalt on a titania film (8 ML titanium deposited followed by oxidation) on NiAl{110}. Each spectra corresponds to a range of post cobalt dose annealing temperatures.

The titania surface supporting 3 MLE cobalt gives rise to two peaks similar to the previous experiments (*figure 6.11*); one at 380 K and a broad asymmetric peak at higher temperature. The peak maximum of the high temperature peak is lower than previous observed: The peak is positioned at 628 K in the 400 K annealing spectrum, which remains essentially in the same place after annealing 500 and 560 K, then shifts down to 496 K after annealing to 600 K. The intensity of the 380 K peak is greater in the spectrum for the sample which was annealed to 560 K and otherwise the peak has similar intensities.

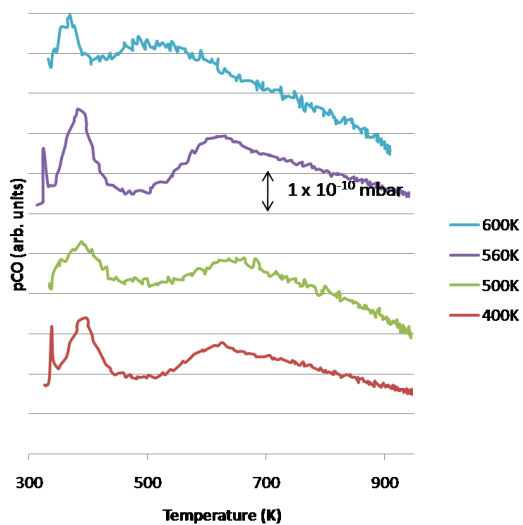


Figure 6.11:- Stacked CO-TPD spectra of 3 MLE cobalt on a titania film (8 ML titanium deposited followed by oxidation) on NiAl{110}. Each spectrum corresponds to a range of post cobalt dose annealing temperatures.

6.4 Discussion

Titanium Oxide – NiAl{110} – Medium Energy Ion Scattering

Due to the similar atomic mass of nickel and titanium determination of the precise nature of the surface structure from MEIS is problematic. This is most apparent in the post-titanium dosing spectrum where there are three distinct peaks between 85 and 90 keV. With the reasonable assumption that the titanium would not give a sub-surface peak, the nickel is considered as contributing to a surface and sub-surface feature at 88 and 90 keV respectively. The spectrum is consistent with the Volmer-Weber growth of large islands of titanium on NiAl{110}. The additional consequence of island growth is that the coverage can be assumed to be underestimated from the AES spectra.

After the sample is oxidised there is a dramatic change in the 85-90 keV region consistent with Ni becoming completely buried below an oxidised alumina/titania film. At this point the titanium peak shape is likely to be complicated by the scattering on ions from sub-surface nickel. Oxidation also results in aluminium becoming visible after being partially buried by the titanium. The shape of the aluminium peak indicates the aluminium is visible across a range of depths which suggests that the oxide film is a solid solution of alumina and titania. Due to the low sensitivity of alumina and the difficulty in determining the intensity of the Ti signal due to the sub-surface Ni contribution, it is not possible to accurately quantify the composition of the oxide surface.

Annealing the sample does not appear to greatly affect the oxide until decomposition at 1300 K. There is a broadening of the high energy feature that can be explained by a 'thinning' of the oxide layer. The increased aluminium peak intensity at 1200 K correspond to the desorption of oxygen and aluminium being increasingly exposed at the surface.

Alumina/ $\text{Al}_x\text{Ti}_y\text{O}_z$ /Titania – NiAl{110} – TPD

The low temperature peak seen in all the alumina supported cobalt spectra is calculated using the Redhead approximation as corresponding to a bonding energy of $100.3 \pm 2.7 \text{ kJ mol}^{-1}$ (The error corresponds to the range of different values for each sample). This calculation is based on a vibration frequency of 440 cm^{-1} for the C-Co stretch, corresponding to the atop site on cobalt [13]. It was not possible to detect any trends within these values – the spread of results are consistent with errors in defining the temperature axis for each spectra.

In the mixed oxide with low titanium content the low temperature peak has a calculated average of $97.8 \pm 2 \text{ kJ mol}^{-1}$ for 0.5 MLE cobalt, $101 \pm 2.1 \text{ kJ mol}^{-1}$ for 1 MLE cobalt and $106.4 \pm 2.6 \text{ kJ mol}^{-1}$ for 3 MLE cobalt. This appears to be a significant trend, especially since the difference between each value exceeds the spread in each group of values. However, this trend cannot be confirmed to be a significant result to the approximate nature of the Redhead equation. One possible hypothesis is that the larger particles have a large metal-carbon monoxide binding energy may be considered, but this would be unexpected when considering smaller particles are usually more reactive [14].

The mixed oxide with medium titanium content has average values of $98.1 \pm 1.5 \text{ kJ mol}^{-1}$ for 1 MLE cobalt and $98.6 \pm 2.5 \text{ kJ mol}^{-1}$ for 3 MLE cobalt. The values for the cobalt supported on the thick titania layer are similar: $98.4 \pm 2.5 \text{ kJ mol}^{-1}$ for 1MLE cobalt and $99.5 \pm 3.1 \text{ kJ mol}^{-1}$ for 3 MLE cobalt. Again, the similarity of these values coupled with to the approximate nature of the Redhead equation suggests the desorption of CO in the 380 K peak is rather independent of Co particle size and the nature of any support.

Considering the possible errors in the temperature scale due to the method used to record the data, small shifts can generally be regarded as artefacts. Qualitatively examining the 380 K peak with such an assumption leads to the conclusion that this peak remains constant. The shifts in the high temperature peak are much larger than any scale errors and can be considered significant when taken in reference to the consistent low temperature peak.

The high temperature peak, only present in the titanium containing oxide spectra, is consistent with a more complicated desorption process. This desorption is likely to be derived from carbon-oxygen recombination and hence to display second order kinetics. This process supports the hypothesis that the titania, which is reducible, supplies oxygen to carbon adsorbed on the surface of the cobalt particles derived from the dissociation of CO presumably at surface defect sites.

An appropriate extension to these experiments would include an examination of the coverage dependence on the peak positions in order to examine the order of desorption. In particular, it would be sensible to test the hypothesis that the higher temperature desorption from the oxides containing titanium is due to the reducible titania supplying oxygen for a carbon-oxygen recombination using an appropriate method such as repeating the experiment following the

creation of the oxide film using $^{17}\text{O}_2$ as opposed to natural oxygen gas – the resulting signal for CO would appear as 29 instead of 28 a.m.u.

In addition to further TPD study on these surfaces, XPS would provide valuable chemical information on both the titanium oxidation state and any electronic effects on the cobalt on each of the oxides. RAIRS would also back up these TPD experiments. These techniques would allow solid conclusions on the possible changes in the low temperature peak in each oxide composition.

Further Work

The mass separation problem in the MEIS data would advocate further study to characterise mixed titania-alumina films. Although hydrogen could be used as the beam ion to increase mass separation in the MEIS data, a more suitable approach would be to use an alternative substrate. Sapphire would be an appropriate choice for ion scattering, but the insulating properties of such a substrate could cause issues related to sample charging by the ion beam. Doped silicon wafers would be a good low atomic mass substrate alternative. In addition the examination with techniques such as XPS and Surface X-Ray Diffraction (SXRD) would prove to be invaluable.

The TPD experiments were scheduled to include silicon for the study of alumina-silica and titania-silica supported cobalt nanoparticles. The characterisation of these surfaces as well as the alumina-titania supported nanoparticles using STM or AFM would be useful in determining the morphology, and in turn, provide data comparable with 'real' catalytic systems.

6.5 Conclusions

Titania grown on NiAl{110} *via* the deposition of metallic titanium and subsequent oxidation at high temperature has been examined with medium energy ion scattering. In addition the temperature dependent behaviour of the oxide film was examined. The metal is considered to grow with island based morphology and form a continuous oxide layer upon annealing. The oxide is not considered to be pure titania, but a mixed titanium-aluminium oxide of undetermined stoichiometry. Decomposition of the oxide occurs between 1200 and 1300 K.

CO-TPD analysis of cobalt nanoparticles supported by a range of mixed oxides from alumina to titania has been carried out. In all cases the spectra consist of a sharp low temperature desorption feature present across all oxide compositions and particle size (or cobalt coverages). This peak is consistent with desorption of chemisorbed CO from atop sites.

CO desorption spectra from mixed oxide (alumina-titania) supported cobalt and titania supported cobalt also include extremely broad peaks at relatively high temperatures that extend from around 500 to 900 K. This peak is hypothesised to be a result from second order desorption from carbon oxygen recombination.

6.6 Bibliography

- [1] Khodakov A. Y. *et al*, Advances in the Development of Novel Cobalt Fischer-Tropsch Catalysts for Synthesis of Long-Chain Hydrocarbons and Clean Fuels, *Chem. Rev.* 107 (2007), 1692-1744
- [2] Khassin A. *et al*, *Metal-support interactions in cobalt-aluminium co-precipitated catalyst: XPS and CO adsorption studies*, *J. Mol. Catal. A* 175 (2001), 189-204
- [3] Fu Q., Wagner T., *Interaction of nanostructured metal overlayers with oxide surfaces*, *Surf. Sci. Reports* 62 (2007), 431-498s
- [4] Baumer M. *et al*, *Metal deposits on well-ordered oxide film*, *Prog. Surf. Sci.* 61 (1999), 127-198
- [5] Kresse G. *et al*, *Structure of the ultrathin aluminium oxide film on NiAl(110)*, *Science* 308 (2005), 1440-1442
- [6] Diebold U., *Surface Science of Titanium Dioxide*, *Surf. Sci. Rep.* 48 (2003), 53-229
- [7] Sui-Wen H. *et al*, *The structure and activity of titania supported cobalt catalysts*, *J. Catal.* 135 (1992), 173-185
- [8] Suriye K. *et al*, *Effect of surface sites of TiO₂ support on the formation of cobalt-support compound in Co/TiO₂ catalysts*, *Catal. Commun.* 8 (2007), 1772-1780
- [9] Storsæter S. *et al*, *Characterisation of alumina-, silica, and titania-supported cobalt Fischer-Tropsch catalyst*, *J. Catal.* 236 (2005), 139-152
- [10] Engel-Herbert R. *et al*, *Microstructure of epitaxial rutile TiO₂ films grown by molecular beam epitaxy on r-plane Al₂O₃*, *J. Cryst. Growth* 312 (2009), 149-153
- [11] Jean-Marie A. *et al*, *Cobalt supported on alumina and silica-doped alumina: Catalyst structure and catalytic performance in Fischer-Tropsch synthesis*, *C. R. Chimie* 12 (2009), 660-667
- [12] Jongsomjit B. *et al*, *Catalytic behaviours of mixed TiO₂-SiO₂ supported cobalt Fischer-Tropsch catalysts for carbon monoxide hydrogenation*, *Mater. Chem. and Phys.* 97 (2006), 343-350
- [13] Beitel G. A. *et al*, *Polarization modulation infrared reflection absorption spectroscopy of CO adsorption on Co(0001) under a high-pressure regime*, *J. Phys. Chem.* 100 (1996), 12494-12502
- [14] Bower M., *The Basis and Applications of Heterogeneous Catalysis*, Oxford (1998), ISBN: 0-19-855958-5

Conclusions

7.1 Conclusion Summary

The structure, composition and adsorption properties of cobalt-palladium model catalyst surfaces grown on a Pd{111} single crystal have been examined using MEIS, STM and TPD (supported by LEED and AES). Ultrathin cobalt films were heated in order to induce the formation of surface alloys whose adsorption properties could then be investigated. In particular, MEIS was used to detect adsorbate induced changes in surface composition following exposure to gases relevant to Fischer-Tropsch catalysis. In addition metal oxide surfaces were synthesised and characterised to provide model oxide supports for the subsequent deposition of cobalt metal particles. These model catalysts were examined by TPD experiments following CO adsorption.

MEIS and STM revealed that the growth of cobalt on the Pd{111} surface was non-pseudomorphic exhibiting island-type morphology – in agreement with previous work [1]. After annealing 4 ML Co on Pd{111} from room temperature to 500 K, the surface morphology remains essentially unchanged and very little intermixing with palladium occurring. At annealing temperatures between 550 and 700 K a stable alloy was formed which STM and LEED revealed was consistent with three domains of a p(2x1) structure. MEIS measurements indicated that the surface composition was approximately 50% Pd. The alloy structure is likely to be based on the bulk ordered PdCo alloy. The {111} plane of this previously unreported surface alloy consists of alternating rows of Co and Pd atoms aligned along the [-110] direction consistent with the striped features observed in STM. As the sample was annealed to temperatures above 700 K, diffusion of cobalt into the bulk resulted in the near-surface region becoming a palladium rich solid solution giving a Moiré pattern that increased in periodicity from 3.4 to 14 nm with increasing temperature and hence with increasing palladium concentration. At each annealing temperature, the periodicity of the Moiré structure could be explained by the lattice mismatch between a Pd_xCo_{1-x} alloy and the underlying Pd{111} surface. Full modelling of the surface layers using the VEGAS program was not achieved due to inadequacies involved in modelling Moiré type structures [2].

The interaction of the bimetallic surface with O₂ at 300 K, as examined by MEIS, resulted in the segregation of the cobalt and in the formation of cobalt oxide films with an unknown stoichiometry. Complete segregation to a pure cobalt oxide film occurred across the full range of starting alloy compositions that were tested. Segregation was complete after the first oxygen dose at 10⁻⁷ mbar. STM revealed that deposition of a cobalt oxide resulted in a thin film exhibiting uniform thickness with a surface that had a rough appearance. The oxide was resistant to change at

annealing temperatures below 700 K – at this point the surface took on a smoother appearance possessing pore like features of 1 layer depth.

Exposure of both cobalt-rich and palladium-rich alloys to CO at 300 K led to strong segregation of cobalt to the surface. The starting composition in the cobalt rich alloy of 30% was reduced to almost zero in the top three layers by the adsorption of CO. The composition in the palladium rich alloy was reduced from around 80 to 50%. No significant changes were observed when the ordered PdCo alloy was exposed to CO indicating that this alloy structure is relatively chemically stable. RAIRS analysis of these alloys was consistent with the MEIS and STM data. At low annealing temperatures the adsorption sites were dominated by the rough islands of cobalt with bonding to atop and defect sites. Throughout the alloy temperature range the RAIR spectra include peaks that indicate 3-fold “hybrid” bonding sites where Co was bound to bimetallic CoPd ensembles. As the cobalt concentration dropped at high annealing temperatures, the RAIRS peaks observed could be attributed to 3-fold palladium adsorption sites as expected.

The adsorption of H₂ and syngas caused less dramatic effects on the composition of the alloy surfaces than either CO or oxygen. MEIS data from the Pd sub-surface revealed that structural disruption of the palladium-rich alloys occurred after exposure to hydrogen which was likely to be related to hydrogen diffusing into the palladium sub-surface. A similar effect was not observed in the syngas experiments which indicated that CO and H₂ alter the adsorption behaviour of each other on the surface.

The formation of titania-alumina mixed oxides model supports for particle depositions results in a thermally stable surface – the stoichiometry of which can be difficult to control through altering the quantity of deposited material alone. Depositing the two components of the mixed oxide onto a substrate that does not react with either component should prove to be a better strategy.

7.2 Further Work

Further modelling of the CoPd surface alloy to obtain a closer fit would not greatly increase the confidence of the structural characterisation due to the inadequacies of the simulations when examining Moiré patterns. The ideal strategy to follow the work presented throughout this thesis would be to analyse adsorbate induced behaviour at the surface of bulk alloys of cobalt and palladium. This could be accomplished using a small number of crystals with different compositions from cobalt rich to palladium.

In addition the work could be augmented using XPS in order to examine the adsorbate-metal chemistry, with particular focus on examining the dissociation of CO and nature of the adsorption of carbon and oxygen. The work of *Chapter 4* would benefit from this approach, allowing a clear-cut determination of the cobalt oxidation state in the metal oxide and the degree of oxidation after oxygen exposure of the metal surface.

Altering the temperature of adsorption in addition to the pressure is also of great interest. This would allow the experiments to closer emulate the conditions in a FTS reactor. For these experiments to be fully effective it would be valuable to conduct the sample analysis *in situ* during gas adsorption where experimental setup allows. The pressures that could be accessible would be restricted by the experimental setup – without the use of purpose built equipment, the pressure could not exceed a few mbar.

As discussed, the TPD work presented in *Chapter 6* indicated the need for supporting techniques such as STM and XPS to provide a detailed characterisation of mixed oxide surfaces. This would give information on the morphology and composition of the supporting oxide, leading to fuller conclusions on the adsorbate/particle behaviour. The priority for strengthening the quality of the MEIS experiments would be to deposit the oxide on a more suitable low-Z substrate, such as graphite, to remove the difficulty in extracting the ion scattering data specific to the surface oxide. However STM/XPS analysis could provide data that removes the requirement for further MEIS experiments.

7.3 Bibliography

- [1] Wasniowska M. *et al*, *Growth and morphology of cobalt thin films on Pd(111)*, Surf. Sci. 601 (2007), 3073-3081
- [2] Howe C.J. *et al*, *Ultra-thin films and surface alloying of Pd on Cu(111) investigated by medium energy ion scattering*, Surf. Sci. 604 (2010), 201-209